

¹

Heavy-ion collisions at the LHC

²

G. Roland¹, K. Šafařík², P. Steinberg³

¹MIT, USA

²CERN, European Organization for Nuclear Research, Geneva, Switzerland

³Brookhaven National Laboratory, Upton, NY 11973, USA

³

December 15, 2013

⁴

Abstract

5 A new era in the study of high-energy nuclear collisions began when the CERN Large Hadron
6 Collider (LHC) provided the first collisions of lead nuclei in late 2010. In the first three years
7 of operation the ALICE, ATLAS and CMS experiments each collected Pb+Pb data samples of
8 more than $150 \mu\text{b}^{-1}$ at $\sqrt{s_{\text{NN}}} = 2.76 \text{ TeV}$, exceeding the previously studied collision energies by
9 more than an order of magnitude. These data have provided new insights into the properties of
10 QCD matter under extreme conditions, with extensive measurements of soft particle production
11 and newly accessible hard probes of the hot and dense medium. In this review, we provide a
12 comprehensive overview of the results obtained in heavy-ion collisions at the LHC so far, with
13 particular emphasis on the complementary nature of the observations by the three experiments. In
14 particular, the combination of ALICE's strengths at hadron identification, the strengths of ATLAS
15 and CMS to make precise measurements of high p_T probes, and the resourceful measurements of
16 collective flow by all of the experiments have provided a rich and diverse dataset in only a few
17 years. While the basic paradigm established at RHIC — that of a hot, dense medium that flows
18 with a viscosity to shear-entropy ratio near the predicted lower bound, and which degrades the
19 energy of probes, such as jets, heavy-flavours and J/ψ — is confirmed at the LHC, the new data
20 suggest many new avenues for extracting its properties in detail.

21 Contents

22	1 Introduction	3
23	1.1 Physics motivation	3
24	1.2 LHC heavy-ion running	5
25	1.3 Detectors at the LHC	6
26	1.3.1 ALICE	6
27	1.3.2 ATLAS	8
28	1.3.3 CMS	10
29	2 Event characterization	11
30	2.1 Centrality determination	11
31	2.2 Charged-particle density	14
32	2.3 Energy density	16
33	3 Particle spectra and yields	17
34	3.1 Charged-particle transverse momentum spectra	17
35	3.2 Identified-hadron spectra	18
36	3.3 Strange-particle production	21
37	3.4 Resonance and light-nuclei production	22
38	3.5 Particle yields	23
39	4 Non-flow correlations	24
40	4.1 Femtoscopic correlations	24
41	4.2 Fluctuations	26
42	4.3 Angular correlations	28
43	4.4 Chiral magnetic effect	30
44	5 Flow correlations	31
45	5.1 Introduction	31
46	5.2 Methods	32
47	5.3 Elliptic flow	33
48	5.4 Higher order harmonics	37
49	5.5 Flow fluctuations	39
50	6 Electroweak probes	41
51	6.1 Measurements of W and Z bosons in Pb+Pb collisions	42
52	6.2 Measurement of isolated photons in Pb+Pb collisions	44
53	7 Jet quenching	47
54	7.1 Dijet correlations	47
55	7.2 Suppression of jet yields	49
56	7.3 Modification of jet structure	51
57	7.4 Energy flow in dijet events	54
58	7.5 Photon-jet correlations	54
59	8 Heavy-flavour production	57
60	8.1 Heavy-flavour particle spectra	57
61	8.2 Heavy-flavour elliptic flow	60

62	9 Quarkonium production	61
63	9.1 Charmonium suppression in PbPb collisions	61
64	9.2 Charmonium elliptic flow	62
65	9.3 Upsilon suppression in PbPb	63
66	10 Summary and outlook	64

67 **1 Introduction**

68 The first ideas about heavy-ion experiments at the Large Hadron Collider (LHC) [1] at CERN were
 69 formed in the late eighties and the early nineties [2]. Since the beginning of the LHC project, approved
 70 by CERN Council in 1994, the investigation of heavy-ion collisions has been an integral part of the LHC
 71 physics programme. Built from 1998 to 2008 in the 27 km long circular underground tunnel, earlier
 72 exploited by the Large Electron–Positron (LEP) collider, the LHC machine represents the highest-
 73 energy particle accelerator ever made. This very versatile collider is designed to reach centre-of-mass
 74 energies up to $\sqrt{s} = 14$ TeV for proton–proton (pp) collisions, and up to 1 150 TeV using lead-ion beams,
 75 corresponding to $\sqrt{s_{NN}} = 5.5$ TeV per colliding nucleon pair. These will entail the energy increase by a
 76 factor of seven for hadron collisions, and more than 27 for heavy-ion collisions compared to previous
 77 colliders.

78 **1.1 Physics motivation**

79 At very high temperatures and densities, hadronic matter is expected to undergo a phase transition into
 80 a qualitatively different state, where quark and gluon degrees of freedom are liberated. Such conditions
 81 were prevailing in the early Universe, a few microseconds after its formation. In heavy-ion collisions at
 82 ultra-relativistic energies, nuclear matter is heated and compressed reaching conditions well beyond the
 83 phase-transition point, and the same type of medium filling the very early Universe is thus momentarily
 84 re-created. At the highest available energies, at the LHC, far better conditions, than those at the other
 85 existing facilities, are achieved to study this state of matter, called the Quark–Gluon Plasma (QGP).
 86 The nearly-vanishing baryon density, the highest available initial temperature and energy density, and
 87 the abundance of perturbatively-calculable hard Quantum Chromo-Dynamics (QCD) processes make
 88 heavy-ion collisions at the LHC particularly well-suited for precision studies of the QGP properties.

89 QCD, the well-established theory of strong interactions, predicts (cross-over) phase transitions in
 90 strongly interacting matter at high temperatures. A phase transition reflects breaking of a fundamental
 91 symmetry in the theory. Above the critical temperature, ordinary hadronic matter, where protons
 92 and neutrons are composed of quarks and gluons confined in a colour-neutral state, melts during the
 93 deconfinement phase transition. In the deconfined medium, quarks and gluons are not bound into
 94 hadrons anymore, however, the effective degrees of freedom of the QGP, formed at temperatures achieved
 95 with heavy-ion collisions, are rather complex. A second phase transition is connected with the generation
 96 of hadron masses as a consequence of the presence of a quark–antiquark condensate in the vacuum at
 97 low temperature. According to QCD, at high temperatures, the vacuum condensate is reduced, and
 98 the masses of quarks drop to their bare values during a chiral phase transition. Quantitative lattice
 99 QCD calculations [3] confirm that QCD matter undergoes a transition from a hadronic gas to a QGP
 100 at a temperature about 160 MeV, corresponding to an energy density of about 0.5 GeV/fm³. At LHC
 101 conditions (low baryon density), the transition is a smooth cross-over spanning a temperature range of
 102 20–30 MeV, which means that the precise value of the critical temperature depends on the observable
 103 used to locate it.

104 In a heavy-ion collision the energy deposited at mid-rapidity is determined by the density of low-*x*
 105 (*Bjorken x*, corresponds approximately to the fraction of nucleon longitudinal momentum carried by a

106 parton) gluons confined in the colliding nuclei. The relevant values of x at LHC energies are one order of
107 magnitude smaller than those at RHIC, i.e. on the 10^{-3} level and below. In such small- x range, at low
108 virtualities the perturbative gluon distribution reaches saturation and gluons have to fuse, in order not to
109 violate unitarity. This marks the transition to the non-linear parton-evolution region, and the virtuality
110 scale at which this transition happens is known as the saturation scale Q_s . It increases (logarithmically)
111 with the incident energy, and the mass of colliding nuclei (as the nucleon radius), and reaches values
112 $Q_s \approx 3\text{--}4 \text{ GeV}^2$ for Pb–Pb collisions at the LHC. During the collision of the two nuclei, these dense
113 gluon fields are deconfined and create a primordial strongly-interacting medium, which rapidly expands
114 and thermalizes. The thermalized QGP continues to cool down, mainly by longitudinal expansion, until
115 its temperature decreases below the critical temperature of the QCD phase transitions, and then it is
116 converted into a gas of hadron resonances. At this moment the produced-particle composition is frozen.
117 The corresponding temperature is called the chemical freeze-out temperature (T_{ch}), and is presumably
118 rather close to the critical temperature of the QCD phase transitions. Hadrons after chemical freeze-out
119 continue to interact. However, since their relative energy is below the threshold for inelastic production,
120 only their momentum spectra are modified. At kinetic freeze-out, with corresponding kinetic freeze-out
121 temperature (T_{kin}), the medium is so diluted that the final hadrons cease interacting altogether and
122 decouple.

123 Prior to the start-up of the LHC heavy-ion programme, the nature of the QGP as an almost-
124 perfect, inviscid liquid emerged from the experimental investigations at RHIC [4]. The pressure created
125 in the thermalized QGP phase is reflected in the large azimuthal asymmetry observed in the final-
126 state particle production. The resistance of the medium to the shape change implies a very low shear
127 viscosity, or in dimensionless variable, a very low ratio of shear-viscosity to entropy-density in the QGP.
128 This indicates extremely short mean-free path inside the medium at this stage of the evolution (and
129 the corresponding cross section approaching the unitarity limit) induced by complex excitation modes
130 in the strongly-coupled QCD medium. This also implies the development of a collective transverse
131 velocity field already at this stage contributing to the plasma cooling. The smallness of the mean-free
132 path with respect to the system size allows for the successful utilization of relativistic hydrodynamics
133 in the description of the evolution of the thermalized QGP until hadronization.

134 Such an interpretation is further supported by the observation of the strong energy loss of partons
135 traversing this strongly-coupled QCD medium, demonstrated at RHIC with large suppression of particle
136 production at transverse momenta (p_T) up to 20 GeV. Deduced from these measurements, the large
137 amount of the energy lost by hard partons due to gluon bremsstrahlung and by elastic collisions is
138 consistent with the low shear viscosity established from the collective-flow pattern of low-momentum
139 hadrons. With the first LHC data, this basic picture has been confirmed with the observation of
140 deconfined matter at unprecedented values of temperatures, densities and volumes [5]. The origin and
141 properties of this almost-perfect-fluid QGP behaviour is the subject of further experimental study at
142 the LHC. Among the important questions to answer are: does the predicted initial gluon saturation
143 also reduce the low- p_T particle yields?; is the low shear viscosity affected by the expected increase of the
144 QGP temperature at an early stage? However, the most important impact of the more than one order
145 of magnitude increase of the collision energy is the large increase of the rates for hard probes, such as
146 the jets, electro-weak particles, heavy flavours, and quarkonia. The high rates allow for precision studies
147 of the QGP using the in-medium interactions of these probes, better controlled theoretically than the
148 propagation of light partons. In addition, some observables, e.g. very high-energy jets, electro-weak
149 bosons, and different Υ states, are accessible in heavy-ion collisions for the first time. A comprehensive
150 compilation of theoretical predictions for the LHC heavy-ion programme was published in [6].

151 The experimental results obtained using heavy-ion collisions during the first period of the LHC
152 running are summarized in this article. It is divided into sections according to the various observables:
153 Sec. 2 describes the principles of centrality selection and measurements of particle and energy densities;
154 particle yields and spectra are discussed in Sec. 3; correlation studies are illustrated in Sec. 4 for non-

155 flow effects, and in Sec. 5 for flow phenomena; Sec. 6 deals with the production of electro-weak bosons;
 156 Sec. 7 is dedicated to jets and their quenching; two sections are devoted to heavy flavours, Sec. 8 to
 157 open heavy flavours, and Sec. 9 to quarkonia. Summary and outlook are given in Sec. 10.

158 **1.2 LHC heavy-ion running**

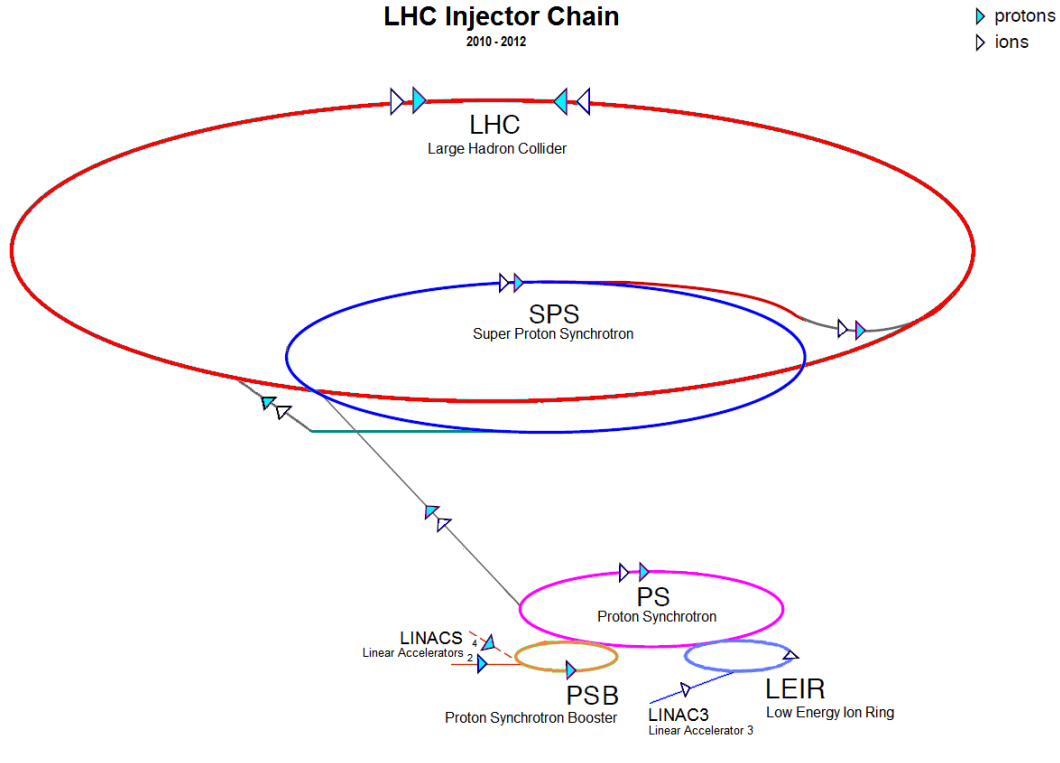


Figure 1: Schematic view of LHC injector chain, showing the path of both protons and ions.

159 Heavy ion running at the Large Hadron Collider had been planned long before the machine was
 160 built. This was based on the interest in the physics at the CERN SPS, which was colliding light ions
 161 since 1986 and heavy ions since 1994, and as a natural extension to the already-planned program at the
 162 Relativistic Heavy Ion Collider (RHIC). The accelerator complex is shown in Figure 1. Ions start their
 163 path to collisions at the ECR (electron cyclotron resonance) ion source, which provides lead isotope
 164 ^{208}Pb ions stripped to values around Pb^{29+} , which are passed through a spectrometer to select Pb^{29+}
 165 and accelerated in a linear accelerator to 4.2 MeV/n. They are then stripped to around Pb^{54+} by a 0.3
 166 μm carbon foil and the Pb^{54+} are selected by a spectrometer to be fed into the CERN Low Energy Ion
 167 Ring (LEIR). LEIR is used to transform a set of low intensity ion pulses from the LINAC into shorter
 168 bunches with higher intensity. This is done by filling the available phase space in three dimensions.
 169 After this, electron cooling is applied to shrink the beam to increase the bunch density, and decelerate
 170 it into “a stack sitting slightly inside the central orbit”. At this point, seven pulses are captured, split
 171 into two bunches, and then accelerated to 72 MeV/n. The bunches from LEIR are then sent to the
 172 CERN PS (Proton Synchrotron), accelerated to 5.9 GeV/n and stripped fully to Pb^{82+} using a 0.8 mm
 173 aluminium foil. These ions are then sent to the SPS where they are accelerated to 177 GeV/n and
 174 injected into the LHC.

175 To date, there have been three heavy ion runs at the LHC. The first run was in November–December
 176 2010, which provided 120 colliding bunches of lead ions in each ring, with a center of mass energy per

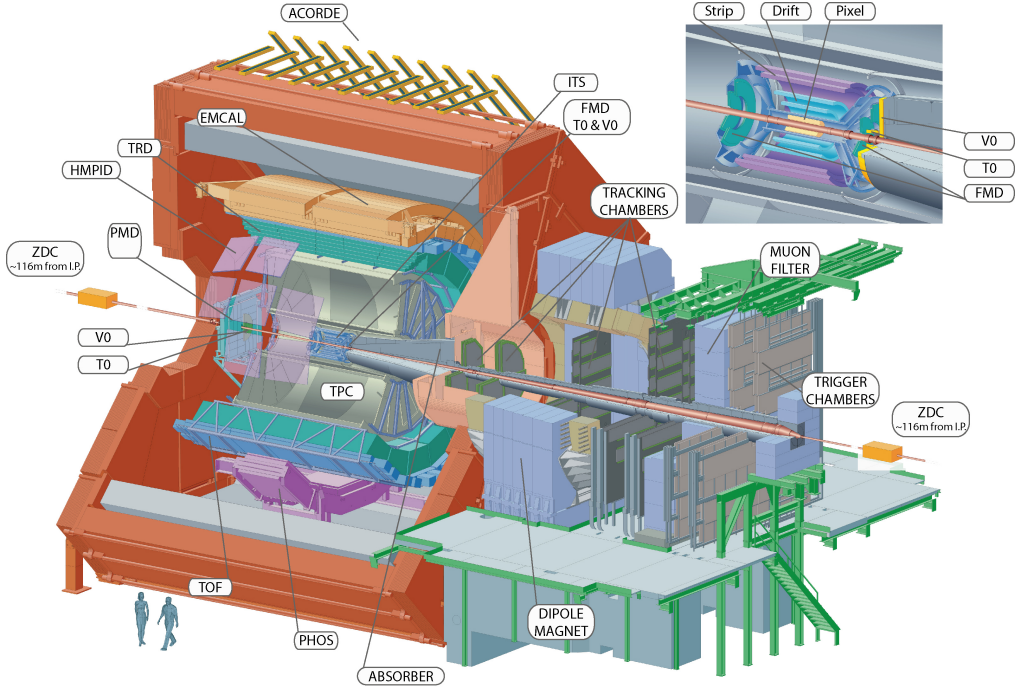


Figure 2: Schematic layout of the ALICE detector, indicating the main subsystems. The inset in the top-right corner shows the innermost part in detail.

177 nucleon pair of $\sqrt{s_{\text{NN}}} = 2.76$ TeV, a peak luminosity of $3 \times 10^{25} \text{ cm}^{-2} \text{ s}^{-1}$ and an integrated luminosity
178 of $7 \mu\text{b}^{-1}$, corresponding to about 50 million minimum bias events. The second run was in November–
179 December 2011, which provided about 360 colliding bunches of lead ions per ring, also at $\sqrt{s_{\text{NN}}} =$
180 2.76 TeV, a peak luminosity of about $5 \times 10^{26} \text{ cm}^{-2} \text{ s}^{-1}$ and an integrated luminosity of about $150 \mu\text{b}^{-1}$,
181 a factor of 20 increase over 2010. The third run, in January–February 2013, provided proton-lead
182 collisions at $\sqrt{s_{\text{NN}}} = 5.02$ TeV but these results are not discussed in detail in this review.

183 1.3 Detectors at the LHC

184 Three, out of the four principal LHC detectors, participate in the LHC heavy-ion programme. These
185 are: ALICE (A Large Ion Collider Experiment), a dedicated heavy-ion detector designed to operate in
186 the high particle density environment; and two general-purpose particle detectors, ATLAS (A Toroidal
187 LHC ApparatuS) and the CMS (Compact Muon Spectrometer), optimized to high interaction rates and
188 capable of precision measurements at very high transverse momenta. The fourth detector, the LHCb,
189 was not taking data in Pb–Pb runs due to the occupancy limitation, however, it participated in the
190 p–Pb run, and reported interesting results.

191 1.3.1 ALICE

192 The ALICE detector [7] is shown in Fig. 2, it has the following main parts: central barrel, muon
193 arm, and forward detectors. The central barrel is housed in a large solenoid magnet providing the
194 field of 0.5 T, with 12 m aperture and 12 m length, which was inherited from the L3 experiment
195 running at the LEP collider. This part provides measurements of particles produced within about
196 $\pm 45^\circ$ with respect to a plane perpendicular to the beam axis, corresponding to the pseudorapidity
197 coverage $|\eta| < 0.9$ ($\eta = -\ln \tan(\Theta/2)$, where Θ is the angle from the beam axis). The six-layer
198 silicon Inner Tracking System (ITS), surrounding the beryllium vacuum beam pipe of 6 cm diameter,

begins with pixel detectors at radii 4 and 8 cm, continues with silicon-drift detectors at 14 and 22 cm, and ends with double-sided strip detectors at 39 and 43 cm. The ITS measures the particle tracks with position precision of a few tens of microns. In addition, the four outer layers participate in the Particle Identification (PID) by determining the specific ionization energy loss (dE/dx). The excellent spatial resolution of the innermost silicon pixel layers results in outstanding capabilities of primary and secondary vertex reconstruction. The resolution in measuring the distance of closest approach to the primary vertex for tracks coming from secondary decays with transverse momentum p_T of 1 GeV is in the range 60–70 μm , allowing to detect weak decays of charm and beauty particles. The main particle tracking device is the TPC (Time Projection Chamber), the largest such detector built to date. It has a cylindrical shape and a size of more than 5 m along the beam axis, and 5 m in outer diameter. The TPC continues the tracking from the ITS starting from a radius of 88 cm and carries on till its outer radius of 2.5 m. The TPC volume, filled with neon-based gas mixture, is divided into two halves by a thin central high-voltage electrode providing an electrostatic field of about 0.4 kV/cm. Electrons created by ionization in the gas drift towards one of the end-plates equipped with multi-wire proportional chambers with cathode-pad readout. Altogether the TPC is read out with more than 600 thousands pads, which gives, taking into account the sampling along the drift direction, an effective granularity in the TPC volume of more than half a billion three-dimensional pixels. This results in very efficient track-finding down to low transverse momenta, about 100 MeV, even at the highest particle densities in central lead–lead collisions at LHC energies. In addition, the ALICE TPC has an excellent resolution for the measurement of dE/dx ; between 5 and 6 %, depending on particle density. The momentum dependencies of dE/dx for different particles come close together when approaching their minima for ionization energy losses. This makes particle identification using the above method impossible in that momentum region. To distinguish particle species in this region, ALICE installed a Time-Of-Flight detector (TOF) at a radius of about 3.7 m from the beam axis. This detector determines the arrival time of charged particles with a precision better than 100 ps, exploiting multi-gap resistive plate chambers, an innovative technology developed specifically for ALICE. The TOF measurement is able to separate pions and kaons up to 2.2 GeV, K mesons and protons up to 3.5 GeV, and can be used for electron identification at lower momenta. To further increase the momentum reach for charged hadron identification, a smaller detector, the High-Momentum PID (HMPID), covering about 10 % of the area covered by the other central barrel detectors and using the Čerenkov ring-imaging technique, is placed at a distance of 1 m larger than that of TOF. To improve the electron identification ALICE uses a Transition Radiation Detector (TRD) situated between the TPC and TOF detectors. Particles traverse six radial drift chambers, each consisting of a transition radiator followed by a volume containing a xenon-based gas mixture, allowing the detection of X-ray photons in addition to charged tracks. The TRD drift chambers are read out with cathode-pad wire chambers. Electrons are separated from pions by discriminating on the signal amplitude of last samples, where the electron transition radiation contributes. This detector is also used in the tracking; an increase of the track length in the magnetic field improves the momentum resolution at high transverse momenta (to about 5 % around 100 GeV). At low momenta, 0.1–1 GeV, the momentum resolution of the ALICE tracking system is better than 1 %. The central barrel part of ALICE is completed with electromagnetic calorimeters. The larger one, EMCal, covers 120° in azimuthal angle, and in the longitudinal direction, a little less than the barrel detectors in front of it. It is used to trigger on jets and to improve the jet energy determination measured with tracking detectors. The much smaller Photon Spectrometer (PHOS) has significantly better energy resolution and granularity, and is dedicated to the isolation of a direct photon signal in heavy-ion collisions.

The ALICE detector can detect and trigger on muons in the forward region on one side of the central barrel using its muon arm, between 2° and 9° from the beam axis. A conical absorber begins at only 90 cm from the nominal interaction point, in order to suppress the background from decaying pions and kaons. Behind the absorber, five tracking stations detect the filtered-out muons. The first two stations

248 are located inside the main solenoid magnet; the third one is in the middle of a dipole magnet with
 249 3 Tm of field integral used for muon momentum analysis; the remaining two measure deflected muon
 250 tracks behind the dipole. Each tracking station consists of two planes of multi-wire chambers with
 251 cathode-pad readout, giving a coordinate precision of about $100 \mu\text{m}$ in the bending plane, thus giving
 252 a mass resolution of 1% at the Υ mass, needed for the separation of the different Υ states. Behind
 253 the last muon tracking station a second absorber shields the muon trigger detectors from the surviving
 254 background. Two trigger planes of Resistive Plane Chambers (RPC) detect the position and direction
 255 of penetrating muons. Using this information the muon trigger electronics select events having muons
 256 with transverse momentum above a predetermined threshold. The full length of the muon arm, from
 257 the interaction point to the end of the trigger system, is about 20 m.

258 On the side opposite to the muon arm the Photon Multiplicity Detector (PMD) measures the yield
 259 of π^0 mesons by counting the number of photons. The Forward Multiplicity Detector (FMD), with
 260 silicon strip planes on both sides of the interaction region, determines the density of charged particles
 261 emitted at pseudorapidities $-3.4 < \eta - 1.7$ and $1.7 < \eta < 5$. Scintillator tile arrays (VZERO), covering
 262 an acceptance similar to that of the FMD, are used to trigger on LHC collisions, selecting different
 263 centrality classes with corresponding thresholds. Small quartz counters on both sides (TZERO detector)
 264 are employed in time-of-flight measurements. Zero Degree Calorimeters (ZDC) are placed more than
 265 100 m from the interaction region in both directions; on each side there is one for the detection of
 266 proton spectators and one for neutron spectators.

267 1.3.2 ATLAS

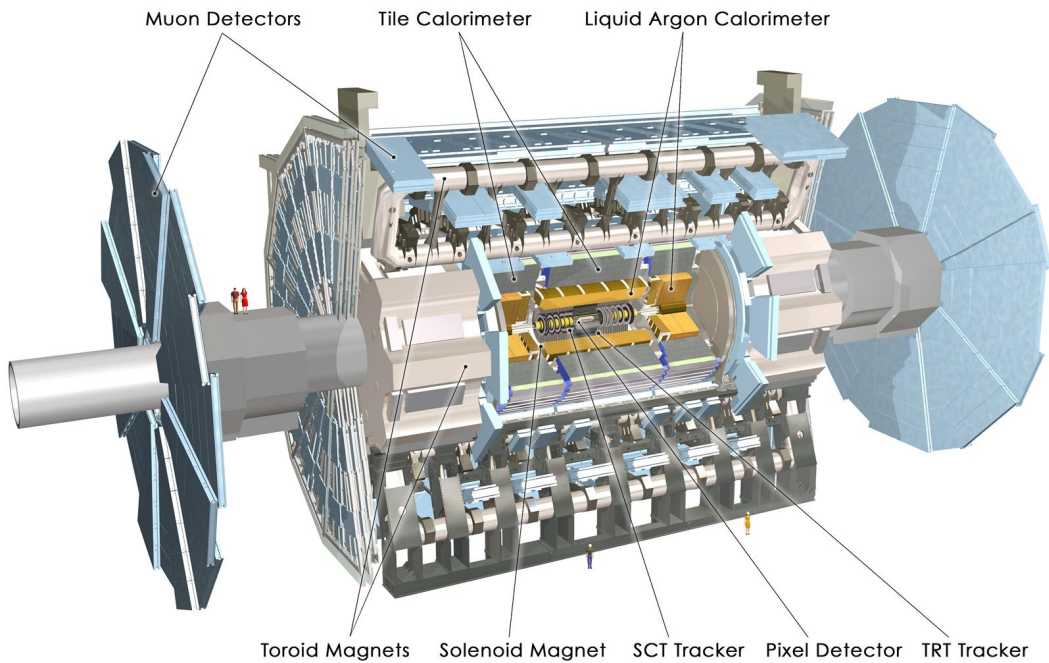


Figure 3: Schematic view of ATLAS detector at the LHC, highlighting the major subsystems.

268 The ATLAS detector [8], shown in Figure 3 is one of the general-purpose particle physics detectors
 269 at the LHC. It has three main detector systems: the inner detector (ID), the calorimeter, and the
 270 muon spectrometer (MS). The inner detector tracks charged particles using three separate detector
 271 technologies, and the spectrometer is immersed in a 2 T axial field from a superconducting solenoid
 272 magnet 1.2 m from the nominal beam axis. The pixel detector typically provides three high-resolution

space points with three layers of pixel detector surrounding the beam pipe within $|z| < 400$ mm (covering approximately $|\eta| < 2$ and 4 disks at forward angles covering out to $|\eta| < 2.5$). The detector has approximately 80.4 million readout channels. While the minimum pixel size is $50 \times 400 \mu\text{m}^2$, the intrinsic position resolution is $10 \mu\text{m}$ in $R - \phi$ and $115 \mu\text{m}$ in z in the barrel region, and $10 \mu\text{m}$ in $R - \phi$ and $115 \mu\text{m}$ in R in the disks. The semiconductor tracker detector (SCT) consists of silicon strips covering out to $|\eta| < X$ in the barrel region and $|\eta| < 2.5$ in the forward regions. The detector has approximately 6.3 readout channels. The sensors have $80 \mu\text{m}$ pitch and are double-sided with a 40 mrad angle between the strip directions to measure hit positions in two dimensions. The intrinsic accuracies per module are $17 \mu\text{m}$ in $R - \phi$ and $580 \mu\text{m}$ in z in the barrel region, and $17 \mu\text{m}$ in $R - \phi$ and $580 \mu\text{m}$ in R in the disks. The transition-radiation tracker (TRT) covers $|\eta| < 2$ with 351,000 4 mm straw tubes in both the barrel and forward regions. It only provides $R - \phi$ coverage out to $|\eta| = 2.0$, with tubes parallel to the beam axis in the barrel region and arranged radially in the endcaps. A track typically has three hits in the pixel detector, 7 hits in the SCT, and 36 in the TRT.

The ATLAS calorimeter has large coverage in pseudorapidity ($|\eta| < 4.9$) and longitudinal segmentation in both electromagnetic and hadronic sections. In the barrel region, the electromagnetic calorimeter uses lead as an absorber and liquid argon (LAr) as the sampling material. The kapton electrodes and lead absorber are accordion shaped over the full coverage, providing full coverage in ϕ without cracks. The EM calorimeter has three longitudinal sections and a presampler layer. The first layer has very high resolution in the η direction, allowing discrimination of photons from neutral hadron decays. The second layer is coarser but deeper, providing the primary energy measurement for electromagnetically interacting particles (photons and electrons), while the third layer is there to catch the tails of the deposited electromagnetic showers. It has a barrel section covering $|\eta| < 1.475$ and two endcap sections each housed in their own cryostat. The outer endcap covers $1.375 < |\eta| < 2.5$ and the inner wheel covers $2.5 < |\eta| < 3.2$. The ATLAS hadronic calorimeter uses steel absorber and measures the hadronic shower energy using scintillating tiles. It has a barrel region covering $|\eta| < 1.0$ and an extended barrel covering $0.8 < |\eta| < 1.7$. Radially, the calorimeter extends from 2.28 m to 4.25 m. It has three longitudinal sections, which are 1.5, 4.1 and 1.8 interaction lengths thick for the barrel region and 1.5, 2.6 and 3.3 interaction lengths thick for the extended barrel. The hadronic end-cap covers $1.5 < |\eta| < 3.2$ and uses LAr technology similar to the EM calorimeter but with copper absorber. The ATLAS forward calorimeter (FCal) covers $|\eta| = 3.2 - 4.9$, using a matrix of copper and liquid argon in the electromagnetic section, and tungsten and liquid argon for the hadronic section. The FCal has a depth of about 10 interaction lengths.

The ATLAS muon spectrometer covers $|\eta| < 2.7$ and is divided into barrel and endcap regions, which are covered by different configurations of magnets and detector technologies. The bending of muons is provided by three sets of air-core toroids, a barrel toroid covering $|\eta| < 1.4$ and providing 1.5-5.5 Tm of bending power, and two end-caps regions covering $1.6 < |\eta| < 2.7$ with 1-7.5 Tm of bending power. The region $1.4 < |\eta| < 1.6$ is covered by a combination of both sets of magnetic fields. The barrel region has tracking detectors arranged in three cylindrical layers around the beam axis, while in the forward region, chambers are arranged in three layers perpendicular to the beam. Out to $|\eta| = 2$, track positions are measured using Monitored Drift Tubes (MDTs). Beyond $|\eta| = 2$, multiwire Cathode Strip Chambers (CGC) with higher granularity are used. The muon system provides a momentum resolution ranging from approximately 2% at low p_{T} up to about 10% at $p_{\text{T}} = 1$ TeV.

Two sets of forward detectors are used for minimum-bias triggering in both p+p and Pb+Pb running. The Minimum Bias Trigger Scintillators (MBTS) are 2 cm thick polystyrene slats mounted at $z = 3.6$ m, divided into 8 sections in ϕ and two sections in η , covering $2.09 < |\eta| < 2.82$ and $2.82 < |\eta| < 3.84$. They are read out by wavelength-shifting fibers embedded in the scintillator. The Zero Degree Calorimeters (ZDCs) use 1 cm thick tungsten plates as an absorber and strips of quartz fibers to read out the light from shower products of incident neutral particles (primarily neutrons and photons). The quartz strips provide the primary energy and time signal. The ZDC is also divided into longitudinal sections, with the

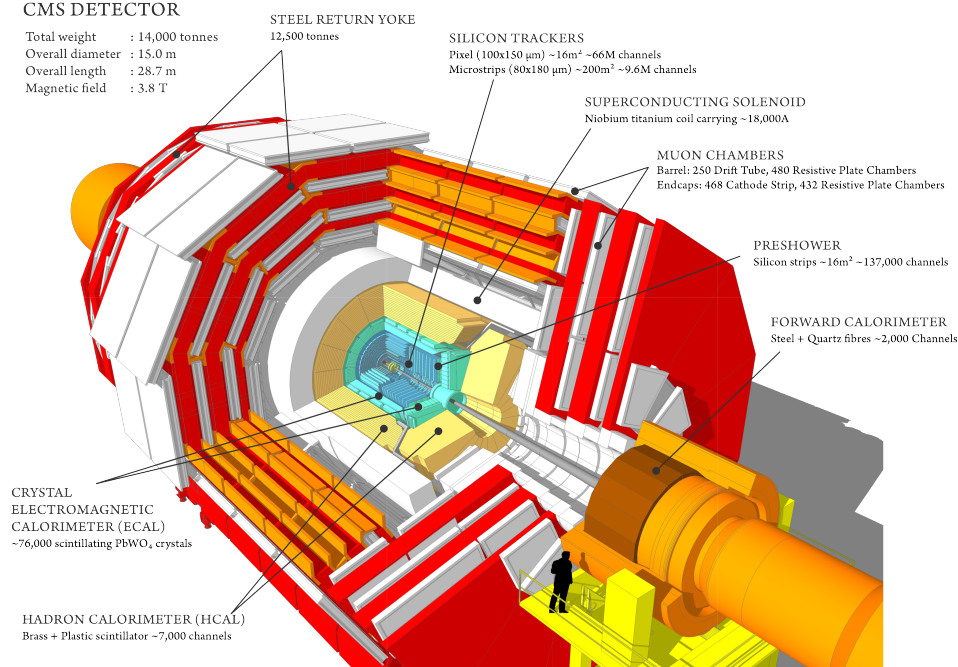


Figure 4: Schematic layout of the CMS detector showing its main subsystems.

322 innermost “EM” section on the negative η side having fine position readout, and the second “hadronic”
 323 section on both sides having coarse position readout. The position readout is performed by a matrix of
 324 quartz fibers oriented in the beam direction.

325 ATLAS provides a sophisticated multi-level trigger system for selection of physics objects (jets, taus,
 326 photons, electrons, muons, and missing transverse energy) and minimum-bias triggers. Jet triggering
 327 is done both seeding on energy deposited into localized regions of the calorimeter, as well as a full
 328 reconstruction of the jets using a similar algorithm as used in the offline analysis. Electron and photon
 329 triggering uses smaller regions in the calorimeter than for jets, and also applies selections based on the
 330 measured shower shape and leakage in the hadronic sections. Muon triggering is provided by thin-gap
 331 chambers and resistive plate chambers, covering about 90% of the solid angle out to $|\eta| = 2.4$. In
 332 general, triggering on tau leptons and missing transverse energy (e.g. from W bosons) is not utilized
 333 for any heavy ion analysis, as both are highly contaminated by the large fluctuations in the underlying
 334 event. Minimum bias triggers are formed primarily from coincidences of the forward and backward
 335 MBTS detectors as well as coincidences of the forward and backward ZDCs.

336 1.3.3 CMS

337 The Compact Muon Solenoid (CMS) is a general purpose collider detector at the LHC. A detailed
 338 description of the CMS experiment can be found in [9]. As shown in Fig. 4, the apparatus has an
 339 overall length of 22 m, a diameter of 15 m, and weighs 14 000 tonnes. The central feature of the
 340 experiment is a superconducting solenoid of 6 m diameter. The large magnetic field of 3.8 T provided
 341 by the solenoid is essential for achieving the very high momentum resolution that is one of the strength’s
 342 of the experiment. Within the volume of the magnet are a silicon pixel and strip tracker, a lead tungstate
 343 crystal electromagnetic calorimeter (ECAL), and a brass/scintillator hadron calorimeter (HCAL). The
 344 silicon tracker measures charged particles in $|\eta| < 2.5$. For 100 GeV/c particles, an impact parameter
 345 resolution of $\approx 15 \mu\text{m}$ and a p_T resolution of about 1.5% are achieved. The ECAL consists of 75 848 lead
 346 tungstate crystals covering $|\eta| < 1.479$ in the barrel region (EB) and $1.479 < |\eta| < 3.0$ in two endcap

347 regions (EE). A two-plane lead/silicon preshower detector is located in front of the EE. The photon
348 energy resolution of the ECAL at $E_T \approx 60$ GeV ranges from 1.1% and 2.6% in the EB region and from
349 and from 2.2% to 5% in the endcaps. Using the particle flow algorithm, which combines information
350 from the inner tracker and calorimeters, the jet energy resolution achieved in p+p collisions typically is
351 15% at 10 GeV, 8% at 100 GeV, and 4% at 1 TeV, which compares to about 40%, 12%, and 5% obtained
352 when the calorimeters alone are used for jet finding. Forward calorimeters extend the rapidity coverage
353 provided by barrel and endcap detectors.

354 In the steel return yoke outside the magnet, detectors are embedded for muon identification. The
355 muon detectors cover $|\eta| < 2.4$ using three detector technologies: drift tubes, cathode strip chambers,
356 and resistive plate chambers. Matching muons to tracks in the silicon tracker allows a p_T resolution
357 between 1 and 5%, for p_T values up to 1 TeV.

358 The detector operates in identical configuration for p+p and Pb+Pb data taking. The main op-
359 erational difference is the configuration of the two-stage trigger system. The first level (L1) of the
360 trigger system employs custom hardware processors and uses information from the calorimeters and
361 muon detectors to select the most interesting events in a fixed time interval of less than $4\mu\text{s}$. The High
362 Level Trigger (HLT) processor farm, based on commodity hardware, decreases the event rate to several
363 100 Hz for final data storage. For heavy-ion data taking, custom reconstruction algorithms executed
364 in the HLT permit the selection of events based on photon, muon, jet and single-track signatures, in
365 connection with global event properties such as charged track multiplicity or energy deposited in the
366 calorimeters.

367 2 Event characterization

368 The first analyses of LHC heavy-ion data dealt with the charged particle density and the energy density
369 achieved in Pb–Pb interactions at an unprecedent collision energy of $\sqrt{s_{\text{NN}}} = 2.76$ TeV per nucleon
370 pair in centre-of-mass system. The estimated values, as well as the results of practically all other
371 measurements, strongly depend on the geometry of the collision (also called centrality), more precisely
372 on the distance b of the centres of colliding nuclei in the plane transverse to the beam axis, called impact
373 parameter of the collision. The impact parameter determines the volume of the interaction region, i.e.
374 how violent the collision was. In this section we first describe how the centrality of Pb–Pb collisions is
375 determined, and then we turn to the basic measurements which characterize these interactions at the
376 LHC.

377 2.1 Centrality determination

378 The lead nuclei are relatively extended objects, their size is about 14 fm across. To classify events ac-
379 cording what part of the two nuclei participated in the interaction, the concept of collision centrality is
380 commonly introduced in the field of heavy-ion physics. The centrality of the collision can be expressed
381 in terms of geometrical parameters, such as the impact parameter b , or the number of participating
382 nucleons. These parameters are inferred by comparison of experimental data with simulations of inter-
383 actions. In this context the geometrical Glauber model is typically used [10], based on a description of
384 pA and A–A scattering, originally proposed by R.J. Glauber [11, 12]. For the event simulation a Monte
385 Carlo implementation of Glauber model is exploited [13, 14], which is realized by the following steps:

- 386 • randomly sample the position of each nucleon inside the nucleus according to a Woods–Saxon
387 distribution (two-parameter Fermi distribution), using the parameters extracted from the analysis
388 of low-energy elastic e–A scattering [15];
- 389 • randomly sample the collision impact parameter b with probability distribution $P(b) \propto b db$ (up
390 to $b_{\text{max}} = 20$ fm, i.e. well above the lead nucleus diameter);

- assuming nucleons are moving along straight lines parallel to the beam direction, a pair of nucleons is considered as colliding if their centres are closer than $\sqrt{\sigma_{\text{NN}}/\pi}$ in the transverse plane, where $\sigma_{\text{NN}} = (64 \pm 5)$ mb is the inelastic nucleon–nucleon cross section, estimated from LHC pp measurements;

and for each event the number of nucleons participating in at least one collision (N_{part}) and the number of these binary collisions (N_{coll}) are counted. Then the total nuclear Pb–Pb cross section (σ_{PbPb}) is calculated as the fraction of πb_{max}^2 given by the ratio of the number of events with $N_{\text{coll}} \geq 1$ to the number of all generated events. The cross section for collisions with impact parameter in the interval $(0, b)$ is obtained the same way, counting the events with $N_{\text{coll}} \geq 1$ having the impact parameter within that interval. The centrality for this impact-parameter selection is its cross section expressed as the percentage of σ_{PbPb} . A centrality class is defined by its lower and upper percentages, corresponding to the events within impact-parameter interval (b_l, b_u) , where the lower percentage is the part of σ_{PbPb} up to the impact parameter b_l and the upper percentage is that part up to b_u . Other characterizations of centrality classes, such as the mean number of participants $\langle N_{\text{part}} \rangle$ and the mean number of binary collisions $\langle N_{\text{coll}} \rangle$ (obtained as the average values for events within that class) are also employed. For completeness, the geometrical overlap function (integral of the convolution of the two transverse nuclear densities in the overlapping region) in the Monte Carlo formulation of Glauber model is defined as $T_{\text{AA}} = N_{\text{coll}}/\sigma_{\text{NN}}$.

However, none of the geometrical quantities mentioned above (b , N_{part} , N_{coll}) is directly measurable in an experiment. Therefore, an experimental observable, which strongly correlates with the collision impact parameter, has to be used to classify the events according to their centrality. For example, the charged-particle multiplicity N_{ch} (or the energy deposition in a calorimeter) within a given pseudorapidity region is often used. In what follows the centrality determination as implemented by the ALICE collaboration is described [16], and later the differences for other experiments are mentioned. The centrality selection of events within a certain impact-parameter interval is then replaced by a selection using a N_{ch} interval. In an ideal case, if one were able to measure the event distribution in such new selection variable for all Pb–Pb nuclear collisions, it would be possible to define centrality selection and centrality percentiles without any model, using only this distribution and its integral. However, for very peripheral collisions (large b , low N_{ch}) the experimental event sample is contaminated by electromagnetic interactions, at LHC energies these processes have a huge cross section (more than two orders of magnitude larger than the nuclear cross section) and contribute to low multiplicity events [17, 18]. It is necessary to suppress them, at least partly, already during the data taking (triggering on a minimum multiplicity value, or requiring some signal in ZDC’s, see Sec. 1.3), which inevitably makes the event trigger less efficient for very peripheral collisions. For these reasons, the event distribution in a variable such as N_{ch} is usable for centrality selection only above some value, typically excluding peripheral collisions corresponding to the centrality class 90–100 %, where the contamination and the trigger inefficiency cannot be neglected. In order to determine the value, from which the distribution can be used, and to relate this so-called anchor point to the centrality, two approaches are utilized. The simulation of the Pb–Pb electromagnetic processes together with the experiment’s trigger response gives the possibility to correct the event distribution of the selection variable, and to estimate a reasonable position of the anchor point with its centrality. Alternatively, the Glauber Monte Carlo can be supplemented with a model of particle production, describing the experimental selection-variable distribution and finding the point where the two deviate. Such an approach also allows to calculate for a given centrality selection the corresponding $\langle N_{\text{part}} \rangle$ and $\langle N_{\text{coll}} \rangle$, taking into account the finite resolution of the selection variable N_{ch} with respect to the collision impact parameter b .

A simple model for multiplicity production, exploited together with a Glauber Monte Carlo, consists in the simulation of the multiplicity distribution from one particle source and a prescription for the number of particle sources depending on the collision geometry, called the number of ancestors (N_{anc}).

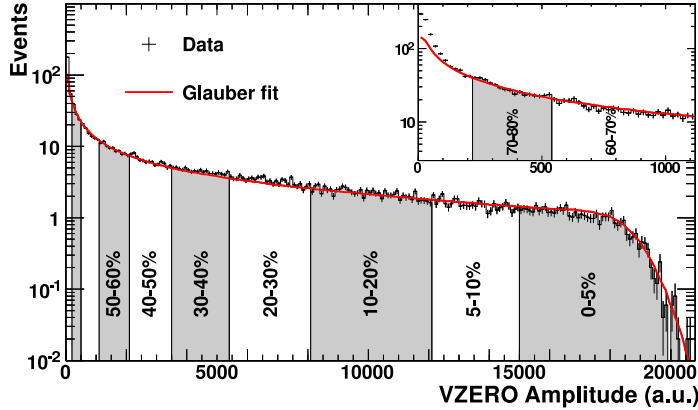


Figure 5: Distribution of the sum of amplitudes from the VZERO scintillators in the ALICE experiment (histogram) fitted to Glauber Monte Carlo coupled to NBD multiplicity production model (line). The inset shows peripheral-collision region enlarged. Reproduced from [16].

For the multiplicity distribution the Negative Binomial Distribution (NBD) is typically used, it has two parameters (controlling the mean and width), and describes reasonably well the charged-particle multiplicity in different pseudorapidity windows for high-energy pp interactions. The number of particle sources is parameterized as a function of N_{part} and N_{coll} , the common choice being $N_{\text{anc}} = fN_{\text{part}} + (1 - f)N_{\text{coll}}$, motivated by a two-component model, where the number of sources is composed of soft (proportional to N_{part}) and hard (proportional to N_{coll}) interactions. Thus, such a model has three parameters, two for the NBD and f for N_{anc} , which are fitted to the experimental distribution of the selection variable between the anchor point and the maximal value (most central collisions).

Figure 5 illustrates the result of such a fit to the event distribution of the sum of amplitudes from the VZERO counters (see Sec. 1.3 for detector description) in the ALICE detector. This variable is proportional to the multiplicity in the pseudorapidity region covered by the VZERO detector. The centrality classes and their percentiles are determined by integrating the experimental distribution from its maximal value down to the anchor point. Simulated events are then used to calculate $\langle N_{\text{part}} \rangle$ and $\langle N_{\text{coll}} \rangle$ for the centrality classes. The ATLAS experiment for the centrality selection is using transverse energy measured in Forward Calorimeters (FCal) and, instead of the model for multiplicity production, the pile-up of calorimeter response from N_{anc} pp collisions is exploited [19]. The CMS experiment bases its Pb–Pb centrality selection on Hadron Forward (HF) calorimeter, and the distribution of the transverse-energy sum is corrected with the simulation of the trigger response [20]. Another detector commonly used for centrality measurements is the ZDC. Its disadvantage is that, unlike for the multiplicity-type detectors, the ZDC response is not a monotonic function of centrality: it gives small signals both for very central and for very peripheral collisions. ZDC's are therefore normally used in correlation with some other detector, especially for central and very central events.

The centrality determination and its uncertainties affect practically all the results from the analyses of heavy-ion data. A careful systematic study of the centrality selection dependence on different assumptions is always required. This usually includes: variation of the parameters describing the nucleus density; including or not a minimal separation between nucleons inside each nucleus; modifying the definition of colliding nucleons (from a black-disc assumption to a Gaussian profile description, or introducing an intra-nuclear rescattering); and changing the functional dependence of N_{anc} , if used, to a power function of N_{part} or N_{coll} . All these uncertainties must then be properly propagated to the measurements of other quantities.

469 2.2 Charged-particle density

470 Traditionally, the very first measurements of heavy-ion collisions at a new energy regime comprise
471 the charged-particle density, and its centrality dependence. These measurements were performed by
472 all three experiments participating in the LHC heavy-ion programme [21, 22, 19, 20], and the first
473 results were published already during the first heavy-ion run [21]. The methods exploited to measure
474 the charged-particle density ($dN_{ch}/d\eta$) in the mid-rapidity region ($|\eta| < 0.5$) were very similar. All
475 experiments used their silicon pixel trackers, detectors closest to the interaction point, to count so
476 called tracklets, pairs of reconstructed hits (pixel clusters) in two layers of the pixel detectors aligned
477 with the primary vertex. Other methods, such as measuring the cluster multiplicity, partial tracking
478 with innermost detectors, and TPC tracking (in the case of ALICE), were also utilized. The collision-
479 energy dependence of $dN_{ch}/d\eta$ for the most central heavy-ion collisions, normalized per participant pair
480 (i.e. $\langle N_{part} \rangle / 2$), is presented in Fig. 6, top part. The results from the three experiments are in excellent
481 agreement, and they show an increase by more than factor of two, compared to the highest value observed
482 at RHIC. The energy dependence of the charged-particle density can be satisfactorily parameterized by
483 a power function: $\propto s_{NN}^{0.15}$. Note that the energy dependence for heavy ions is significantly steeper than
484 that for pp interactions ($\propto s^{0.11}$), this is also reflected by the more than a factor two higher value of
485 the normalized charged-particle density ($dN_{ch}/d\eta)/(0.5\langle N_{part} \rangle)$ in heavy-ion collisions compared to pp
486 interactions. It is interesting to note that most of the theoretical and model predictions for the LHC
487 charged-particle density underestimated the experimental observation [21], contrary to a clear tendency
488 for an overestimation when the first results from RHIC experiments were published.

489 In the bottom part of Fig. 6 the centrality dependence of the same quantity ($dN_{ch}/d\eta)/(0.5\langle N_{part} \rangle)$,
490 expressed as a function of $\langle N_{part} \rangle$, is presented. Again, very good agreement among the three LHC
491 experiments is observed. The data from RHIC (average value over the four experiments [23]) are also
492 shown, multiplied by a factor 2.15 to match the points for the most central collisions. The normalized
493 charged-particle density is rising with centrality, which means that the particle multiplicity at mid-
494 rapidity increases faster than the number of participants, presumably due to the contribution of hard
495 processes to the multiplicity production. However, this increase is very similar to that observed at
496 the top RHIC energy. Apart from a simple interpretation of these data in terms of (a mixture of)
497 soft and hard interactions, model calculations implementing a saturation picture, where the number of
498 soft gluons available for the multiplicity production is progressively reduced by parton recombination,
499 attempt to determine the energy and centrality dependence of the saturation scale [24, 25, 26].

500 The experiments were also looking for the $dN_{ch}/d\eta$ evolution in the longitudinal direction, i.e. as
501 a function of pseudorapidity. The ATLAS collaboration published the charged-particle densities for
502 different centrality classes in $|\eta| < 2$ [19], and the CMS detector measured $dN_{ch}/d\eta$ in the interval $|\eta| <$
503 2.5 [20]. The ALICE experiment extended the pseudorapidity coverage of such measurement to $-5 <$
504 $\eta < 5.5$ [27], exploiting the FMD (see Sec. 1.3) and so called satellite bunches. The latter are created in
505 the accelerator RF cavities, when a small fraction of particles slips from the main bunch into another
506 wave period, 75 cm apart (corresponding to RF frequency 400 MHz). This way, very low-intensity
507 satellite collisions, distanced by every 37.5 cm from the main bunch crossing, are produced, shifting
508 the pseudorapidity acceptance. Figure 7 shows the results of the ALICE pseudorapidity distribution
509 measurement, compared to the data previously obtained by CMS and ATLAS. The wide-rapidity data
510 are used together with the RHIC results (from the BRAHMS [28] and PHOBOS [29] experiments)
511 to confirm limiting fragmentation — the shape of the distributions are in the fragmentation region
512 independent of the collision energy. By extrapolation, the total charged-particle multiplicity in Pb–Pb
513 collisions at $\sqrt{s_{NN}} = 2.76$ TeV for different centralities can be estimated, for example, in 5% of the
514 most central events $(17.2 \pm 0.8) \times 10^3$ charged particles are created.

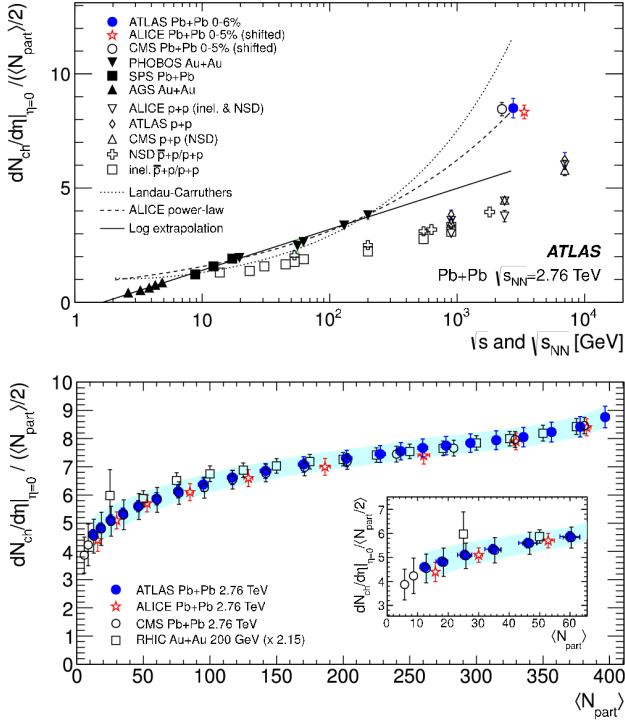


Figure 6: Top: Energy dependence of the charged-particle density at mid-rapidity ($|\eta| < 0.5$) normalized per participant nucleon pair, from various pp (and $\bar{p}p$) measurements, and most central heavy-ion collisions. The curves represent various extrapolations from lower-energy data to LHC, the one describing heavy-ion experimental points (dashed line) is a power function $(dN_{ch}/d\eta)/(0.5\langle N_{part} \rangle) \propto s_{NN}^{0.15}$ proposed in [21]. Bottom: $\langle N_{part} \rangle$ dependence of the charged-particle density normalized per participant nucleon pair from the three LHC experiments, compared to average value from RHIC experiments, multiplied by a factor 2.15. The inset shows in detail the peripheral-collision region with $\langle N_{part} \rangle < 60$. Reproduced from [19].

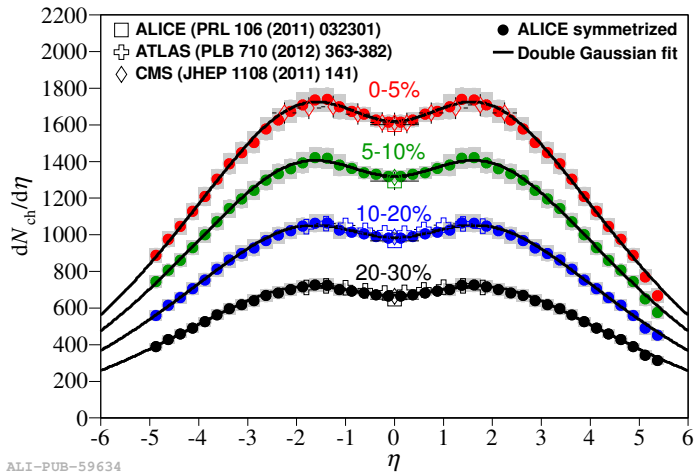


Figure 7: Charged-particle pseudorapidity density distribution for various centrality classes, comparison among the LHC experiments. Reproduced from [27].

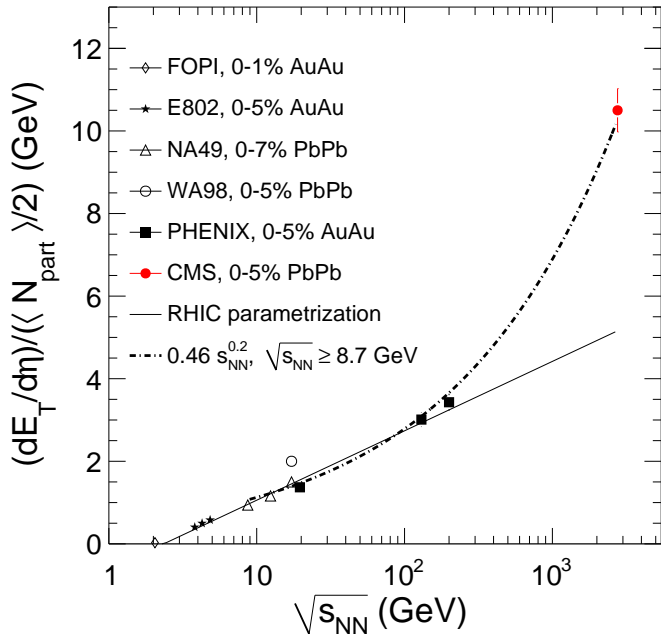


Figure 8: Collision energy dependence of the transverse-energy pseudorapidity density at mid-rapidity, normalized to the number of participant pairs, for central heavy-ion collisions. The curves represent various extrapolations from lower-energy data to LHC, the one describing the LHC measurement (dashed-dotted line) is a power function $(dE_T/d\eta)/(0.5\langle N_{\text{part}} \rangle) \propto s_{\text{NN}}^{0.2}$ proposed in [30], from where this figure is reproduced.

515 2.3 Energy density

516 In order to estimate the energy density achieved in Pb–Pb collisions at the LHC, the measurements of
 517 the transverse energy pseudorapidity density, $dE_T/d\eta$ were performed. The CMS experiment measured
 518 directly the energy flow in calorimeters for different pseudorapidities and centralities [30]. The collision
 519 energy dependence of $dE_T/d\eta$ at mid-rapidity for the most central heavy-ion collisions, normalized to the
 520 the number of participant pairs, is shown in Fig. 8. An increase by more than a factor three is observed
 521 from the top RHIC energy to the LHC. This collision-energy dependence can be satisfactorily described
 522 by a power function $\propto s_{\text{NN}}^{0.2}$, which means that the transverse-energy density rises with collision energy
 523 faster than the particle density, indicating a significant increase of the average transverse momentum
 524 of particles produced in the LHC heavy-ion interactions. The ALICE experiment confirmed the CMS
 525 results estimating $dE_T/d\eta$ from $dN_{\text{ch}}/d\eta$ and the measured transverse-momentum spectra for different
 526 hadron species.

527 Even in forward region, up to $|\eta| = 5$, the transverse-energy density observed at the LHC is larger
 528 than that at mid-rapidity at the top RHIC energy. The energy density achieved in heavy-ion interac-
 529 tions (ϵ) is commonly related to the transverse-energy density by the Bjorken formula [31], based on
 530 geometrical considerations. It can be expressed as $\epsilon\tau_0 = (dE_T/dy)/S$, where τ_0 denotes the time when
 531 the initial thermalization was established (supposed to be $\tau_0 \leq 1$ fm), and S is the transverse overlap
 532 area, approximated for central Pb–Pb collisions with $\pi(7\text{ fm})^2$. For the top 5 % centrality CMS obtained
 533 $\epsilon\tau_0 = 14 \text{ GeV}/\text{fm}^2$ (using a model estimation for Jacobian $d\eta/dy \approx 1.1$). This represents a factor 2.6
 534 increase with respect to the highest RHIC collision energy, and an even larger increase for the energy
 535 density ϵ , since the time τ_0 is expected to be shorter at the LHC.

536 3 Particle spectra and yields

537 3.1 Charged-particle transverse momentum spectra

538 Transverse momentum spectra of charged particles were measured by all three experiments exploiting
 539 the first collected data sample. They are presented as the dependence of the (inclusive) invariant cross
 540 section on the transverse momentum (p_T), and finally in the form normalized to pp measurement at the
 541 same nucleon–nucleon energy. For the latter representation, the nuclear modification factor is defined
 542 as

$$R_{AA}(p_T) = \frac{dN_{ch}^{AA}(p_T)/dp_T}{\langle N_{coll} \rangle dN_{ch}^{pp}(p_T)/dp_T}, \quad (1)$$

543 where on the right hand side the superscripts AA and pp refer to the values obtained in heavy-ion and
 544 pp measurements, respectively. If a collision of two nuclei behaved as a simple superposition of N_{coll}
 545 nucleon–nucleon collisions, the nuclear modification factor would be $R_{AA} = 1$. Such a scaling with the
 546 number of binary collision N_{coll} is a natural expectation for hard processes, in case that nucleons act
 547 independently and their interactions are not influenced by the rest of the nuclei. This is observed for
 548 electro-weak bosons, since they practically do not interact with the surrounding medium, see Sec. 6.
 549 A deviation of R_{AA} from unity for hard processes signals a nuclear effect. However, for soft processes,
 550 such as particle production at p_T below a few GeV, the scaling from pp to AA is governed by N_{part}
 551 rather than by N_{coll} leading to a higher R_{AA} in that p_T region, especially for central events.

552 The p_T spectrum for charged particles in LHC heavy-ion collisions was expected to be suppressed
 553 at high p_T with respect to pp interactions. The fact that R_{AA} is significantly below unity at p_T above
 554 a few GeV was well established for central collisions at RHIC, and attributed to the jet quenching —
 555 an energy loss of hard partons in their interactions with the surrounding high-density nuclear matter.
 556 As the high- p_T particles are supposed to be produced in the fragmentation of such hard partons, their
 557 quenching lowers the particle production, reflecting the amount of energy loss, and thus the density of
 558 nuclear matter created in the collision. However, the value of R_{AA} is also dependent on the steepness of
 559 the parton p_T spectrum (a harder parton spectrum at the LHC should result in less particle suppression),
 560 and on the nuclear modification of the structure functions (distribution of partons inside a nucleon).
 561 Therefore, for theoretical predictions and interpretations of the R_{AA} behaviour, model calculations
 562 taking into account the interplay of many effects are necessary.

563 The first LHC measurement of charged-particle R_{AA} , was published by ALICE [32], presenting the
 564 p_T spectrum up to 20 GeV, for the 5% most central Pb–Pb events. It showed a slightly stronger
 565 suppression compared to RHIC: the largest suppression, in the p_T range 6–7 GeV, was a factor about 7
 566 at the LHC, while at RHIC a factor of 5 was observed. A new observation was that with increasing p_T
 567 the suppression gets smaller, i.e. R_{AA} increases. This was soon confirmed by the CMS measurement [33],
 568 extending the p_T reach up to 100 GeV (see Fig. 9). The nuclear modification factor R_{AA} exhibits a
 569 clear increase up to p_T about 40 GeV, and then seems to saturate with the R_{AA} value about 0.5–0.6
 570 for the most central collisions. Figure 9 also shows the p_T dependence of R_{AA} at lower energies, and a
 571 variety of model calculations [34, 35, 36, 37, 38, 39]. Different models can be tuned to fairly reproduce
 572 the R_{AA} data, however, it remains to demonstrate that they describe with the same parameters the
 573 ensemble of other observables, especially the azimuthal anisotropy (Sec. 5).

574 The CMS and ALICE experiments also measured the R_{AA} p_T dependence for different collision
 575 centralities [33, 40]. The charged-particle production is, as expected, less and less suppressed as one
 576 moves from central to peripheral Pb–Pb collisions. The ATLAS collaboration reported similar results,
 577 presented as R_{CP} as a function of p_T , where R_{CP} stands for a quantity analogue to that defined in Eq. 1
 578 using the normalized ratio of heavy-ion results at different centralities (the subscript CP indicates the
 579 central-to-peripheral ratio), commonly using the most peripheral class available for normalization.

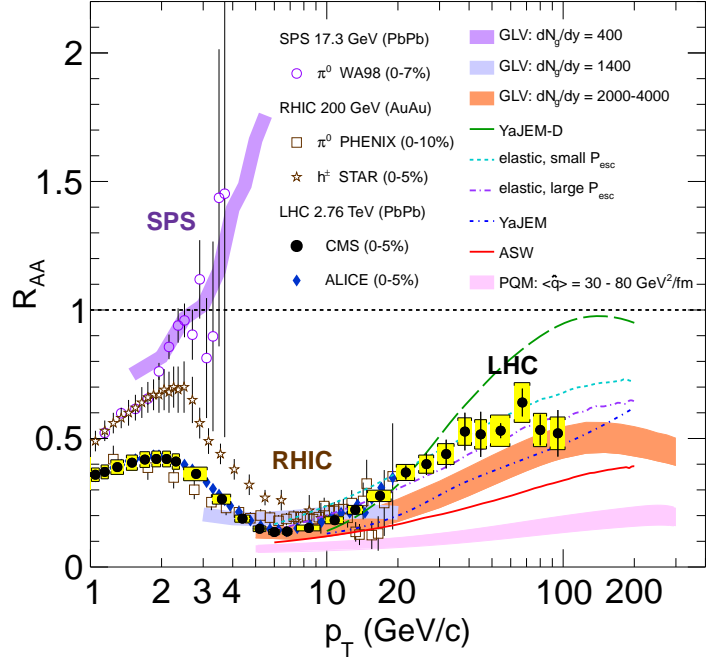


Figure 9: Transverse momentum dependence of nuclear modification factor R_{AA} for charged particles produced in central heavy-ion collisions at LHC and lower energies. The curves and bands represent different model calculations. Reproduced from [33].

580 3.2 Identified-hadron spectra

581 Study of the particle composition as a function of p_T reveals a mass hierarchy, interpreted as resulting
 582 from a common radial-velocity field created during the expansion of the dense-matter fireball. Such
 583 a collective flow arises in strongly interacting matter in the presence of a pressure gradient. Having
 584 the same velocity, heavier particles (e.g. protons) will acquire a larger momentum than lighter mesons.
 585 This effect is clearly visible in Fig. 10, where the p_T spectra for pions, kaons, and protons measured by
 586 the ALICE experiment [41, 42] exploiting various particle-identification techniques, are presented for
 587 the top 5 % central events. From the simultaneous blast-wave fit [43] to these spectra (excluding pions
 588 with $p_T < 0.5$ GeV and kaons with $p_T < 0.35$ GeV where resonance decays largely contribute), the
 589 kinetic freeze-out temperature (T_{kin} , temperature when the hadrons cease to interact) and an average
 590 radial velocity ($\langle\beta\rangle$) is estimated. The two parameters were extracted for different centralities, and
 591 they were found to be strongly correlated, since they both determine the slope of the p_T spectra. Both
 592 T_{kin} and $\langle\beta\rangle$ are higher compared to RHIC, and they depend on centrality: T_{kin} being lower for more
 593 central collisions, while $\langle\beta\rangle$ increases. The values reached for 5 % of most central collisions are $T_{kin} \approx$
 594 95 MeV and $\langle\beta\rangle \approx 0.65$, the latter being more than 10 % above the RHIC value. These spectra were
 595 compared further to various hydrodynamical-model calculations [44, 45, 46, 47], and a fair description
 596 for the bulk production, up to transverse momenta 2–3 GeV, i.e. where such models are applicable,
 597 is observed for central collisions. In some cases [47, 48] the agreement is improved by supplementing
 598 the hydrodynamical calculations with a hadronic rescattering code (UrQMD [49], in this occasion).
 599 The Krakow model [50, 51] uses bulk viscosity corrections at freeze-out to describe deviation from
 600 equilibrium, which seems successful in reproducing the data. But going to more peripheral collisions
 601 the hydrodynamical description becomes worse at higher p_T and shows the limits of the hydrodynamical
 602 models. This could indicate the onset of a non-thermal (hard) component, which in more peripheral
 603 collisions is not dominated by the flow-boosted thermal component [45].

604 The p_T spectra of identified charged hadrons are determined up to $p_T = 20$ GeV [52], exploiting the

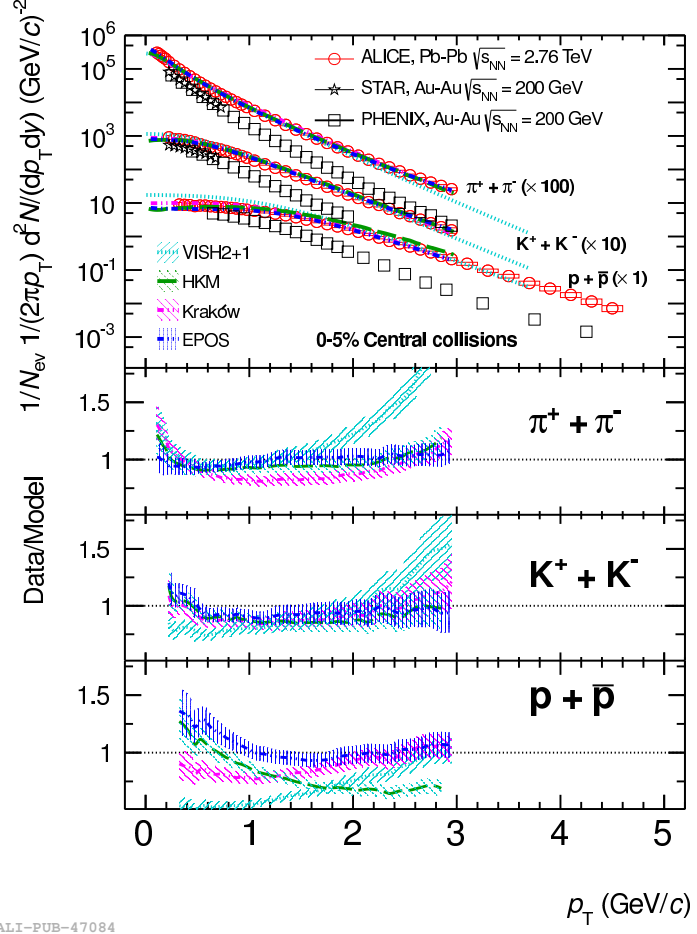


Figure 10: Transverse momentum spectra for pions, kaons, and protons (sum of particles and antiparticles) produced in 5 % of most central Pb–Pb collisions at LHC, compared to the RHIC measurements and different model calculations. Adapted from [41].

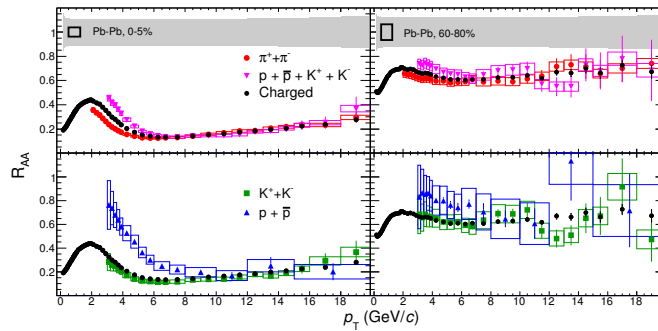


Figure 11: Nuclear modification factor R_{AA} for pions, kaons, and protons (sum of particles and antiparticles), and averaged for charged particles, as a function of p_T for central (left, 0–5 %) and peripheral (right, 60–80 %) Pb–Pb collisions. Reproduced from [52].

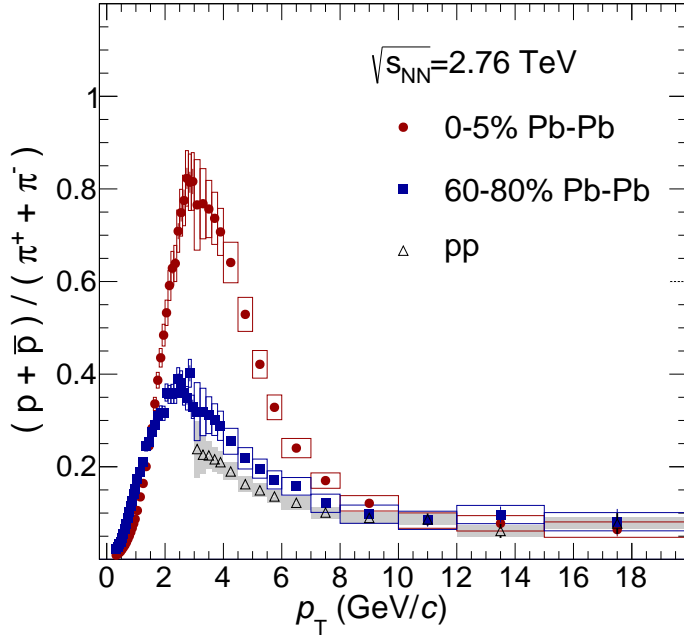


Figure 12: Ratio of proton-to-pion yields as a function of p_T measured in central (0–5 %) and in peripheral (60–80 %) Pb–Pb collisions, and in pp collisions. Reproduced from [52].

measurement of ionization energy losses in the ALICE TPC in the relativistic rise region. Figure 11 presents these results normalized to the pp baseline, as R_{AA} for pions, kaons, and protons, compared to the (averaged) charged-particle data. It is clearly seen that for p_T above 7–8 GeV the behaviour for all particle species coincides. For lower p_T a mass hierarchy appears: the heavier the particle, the lower its suppression. These observations suggest the presence of three regions in transverse momentum:

- bulk region, low p_T up to 2–3 GeV, where the production comes from the hadronization of high-density strongly-interacting matter created in a heavy-ion collision, reflecting collective radial flow, fairly described (at least for central collisions) by hydrodynamical models;
- intermediate region, in p_T up to 7–8 GeV, where still a mass splitting among various particle species persists that can be attributed a reminiscence of radial flow (the difference has to disappear for p_T values significantly larger than particle masses), however, additional ideas were put forward to push further in p_T this mass distinction, such as constituent-quark recombination [53] which would favour baryons to acquire larger p_T than mesons;
- fragmentation region, above 7–8 GeV in p_T , where the different hadron species exhibit a common suppression pattern, and consequently their relative abundances are the same as in pp collisions, naturally explained as being fragmentation products of a high- p_T parton coming from a hard scattering at early stage (which itself is quenched by the surrounding high-density matter).

To look in detail into the intermediate region, it is instructive to plot the proton-to-pion ratio as a function of p_T , Fig. 12. The striking effect is that for central collisions at p_T around 2.5–3 GeV this ratio is more than a factor three higher than the value for pp collisions. This so-called baryon anomaly was observed already at RHIC [54, 55], and certainly the low- p_T rise is explained by the hydrodynamical radial flow. In the intermediate region, where the hydrodynamics ceases to work, the behaviour is qualitatively described by models involving constituent-quark recombination [56] or baryon string-junction transfer along the axis of a fragmenting jet [57]. These models, however, tend to predict an anomalous baryon-to-meson ratio even for significantly higher p_T than actually observed.

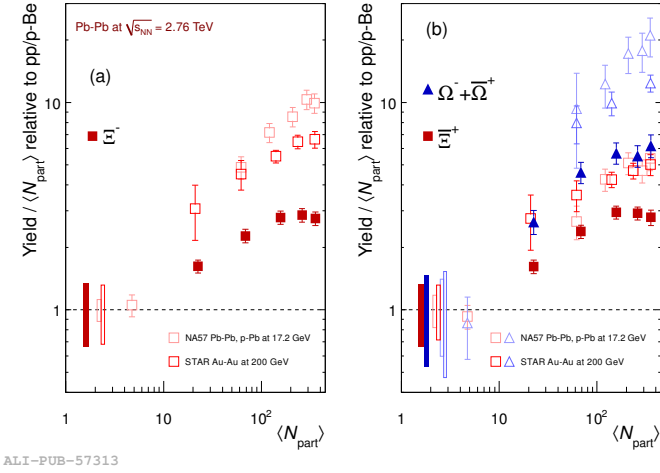


Figure 13: Strangeness enhancement for Ξ and Ω at the LHC as the function of the mean number of participants, compared to the results obtained at CERN SPS and RHIC. Reproduced from [65].

On the other hand, a smooth connection between the hydro-described bulk region and the normal-ratio fragmentation region, using a realistic radial-flow profile, will probably move the border between the intermediate and fragmentation regions to lower than observed values. Therefore, a comprehensive description of the particle production in the intermediate region is still an open, and experiment driven issue. Recently, a good description has been obtained by EPOS model [46], where the interaction between bulk matter (which thermalizes and flows) and jets is considered.

3.3 Strange-particle production

Historically, the enhancement of strangeness production was among the first signatures proposed to signal a qualitatively different state of matter, expected to be created in ultra-relativistic heavy-ion collisions [58, 59]. The strangeness increase in high-temperature QCD matter is motivated by two reasons: the relevant quark masses drop from their constituent to their bare values, and then the strange-quark mass becomes comparable to the temperature, consequently the production rates for different light quarks tend to equalize. Strangeness enhancement was already observed at lower energies, at the SPS [60, 61, 62, 63], as well as at RHIC [64]. The systematic study of strangeness production at the LHC is under way in ALICE [65, 66]. In addition to charged kaons, the measurements include topologically identified particles (K_s^0 , Λ , Ξ^- , and Ω^-), and resonances containing strangeness.

The enhancement of strangeness production is confirmed at the LHC, see Fig. 13, albeit the enhancement factor, expressed as the ratio of the yield per participant in AA collisions to that in pp (or pA) collisions, decreases slowly with the collision energy. This reflects the fact that the production of strange particles per pion in heavy-ion collisions practically saturates as $\sqrt{s_{NN}}$ reaches few tens of GeV, while in pp it still increases from RHIC to the LHC, and only at the highest energy ($\sqrt{s} = 7$ TeV) seems to cease its growth.

The strange-particle R_{AA} is also influenced by strangeness enhancement, especially in the bulk and intermediate p_T regions. As already mentioned, kaons, including K_s^0 , are above the pion curve. The strange baryons have larger R_{AA} than protons, and R_{AA} increases with the strangeness content, exceeding unity for Ω^- . With increasing p_T , the strangeness R_{AA} goes progressively closer to the common fragmentation behaviour for all other particle species, still being for Ω^- at $p_T \approx 7$ GeV above the others. These measurements are at this point limited by the available statistics.

Baryon-to-meson ratio in the strangeness sector is very similar to that of proton-to-pion. The Λ -to- K_s^0 ratio as a function of p_T is shown in Fig. 14 together with hydrodynamical- and recombination-model

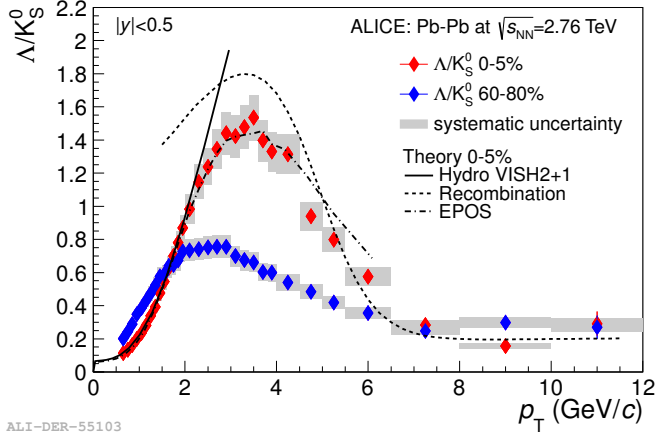


Figure 14: Ratio of Λ -to- K_s^0 yields as a function of p_T measured in central (0–5 %) and in peripheral (60–80 %) Pb–Pb collisions compared to model calculations. Reproduced from [66].

calculations [67, 68, 69]. The EPOS model [70], which includes the hydrodynamical expansion and, at higher p_T , the (mini-)jet fragmentation with an interaction between jets, describes the experimental measurement fairly well.

3.4 Resonance and light-nuclei production

The resonances are interesting to study in heavy-ion collisions, because of their short lifetime they may decay inside the medium, before the kinetic freeze-out. If a decay product scatter changing its momentum, the parent resonance cannot be observed by invariant-mass reconstruction, and that leads to an apparent depletion of the resonance yield, which is dependent on the resonance lifetime. On the other hand, resonances can be also recreated during the elastic scattering phase having a large cross-section for s -channel production at very low energies. Therefore, the comparison of the different-lifetime-resonance yields with hadronic-transport models gives valuable information about the time evolution during the late stage of heavy-ion collisions.

At the LHC, the ALICE collaboration reported the measurements of $K^*(892)^0$ and ϕ mesons. The yield of K^{*0} relative to other particles (e.g. K^-) decreases significantly for more central collisions, while the ϕ yield normalized in the same way is compatible with being independent of centrality. This is qualitatively understood by an order of magnitude different lifetimes for the two resonances (4.2 fm and 46 fm for K^{*0} and ϕ , respectively). A substantially lower production of K^{*0} in central collisions also means that the regeneration is not effective enough to compensate the decay rate. Similar observations were made at RHIC [71]. The ϕ meson, being relatively long-lived to be treated as stable on the time scale of the heavy-ion collision, is of special interest. Its mass is close to that of the lightest baryons, therefore, the ϕ p_T spectrum can differentiate mass-dependent effects and constituent-quark-number effects. Preliminary data indicates compatibility between proton and ϕ p_T spectra up to 5 GeV, favouring thus the radial-flow explanation of the baryon anomaly to the constituent-quark-recombination one.

The high density of particles produced in heavy-ion collisions implies substantial rates for light-nucleus and hypernucleus production. The interest of such measurement is to study the production mechanism of such state, their coalescence coefficients, and their thermodynamical equilibrium with other particles. The light nuclei, such as d, t, ${}^3\text{He}$, and ${}^4\text{He}$, and corresponding antinuclei, were observed in heavy-ion collisions at RHIC and the LHC, and quantitative results for d and ${}^3\text{He}$ were reported by ALICE. These measurements use the particle identification based on the specific ionization losses in

TPC and the TOF measurement. The production of hypernuclei (nuclei containing one or more strange baryons) is of additional interest since the (unknown) properties of hypernuclei, their masses and decays, can be measured. The ALICE collaboration reconstructed the ${}^3\Lambda H \rightarrow {}^3He + \pi^-$ decays, as well as the charge-conjugated ones, opening the study in this field at the LHC, following the first antihypertriton measurement at RHIC [72]. Searches for more exotic states, such as the H-dibaryon ($\Lambda\bar{\Lambda}$ bound state or six-quark state), the $\Lambda\bar{n}$ bound state, and the $\Phi(1860)$ pentaquark have not given any positive signal.

3.5 Particle yields

The particle yields at mid-rapidity are obtained by integration of the transverse-momentum spectra fitted to the blast-wave functional dependence (or other suitable function), in order to extrapolate below the lowest measured p_T . Traditionally, the particle yields in heavy-ion collisions are studied within statistical hadronization models [73, 74, 75, 76]. These models are based on the grand-canonical ensemble, describing the system with the temperature (T_{ch}), the baryon chemical potential (μ_b), and the volume in thermal and chemical equilibrium with the rest. Knowing these parameters it is straightforward to calculate the average number of various particles in the system. All the resonance and other unstable states, summed-up in the grand potential (usually with an upper mass cut-off about 2 GeV, as above the resonance spectrum is not well known), are decayed into observed particles and compared to the measurements. The temperature T_{ch} is interpreted as the chemical freeze-out temperature, below which the energy of hadronic re-scattering is lower than the threshold for inelastic interactions, and thus the particle composition remains unchanged.

The statistical models were used to describe the heavy-ion collision data from very low energies up to RHIC with a good agreement for most of the particle species. The temperature T_{ch} practically does not change with the collision energy, therefore, a reasonable estimate for LHC is the value observed at RHIC, $T_{ch} = 164$ MeV; the chemical potential has to be very low as the ratio particles to antiparticles is for all species compatible with unity; $\mu_b = 1$ MeV is usually assumed. The predictions using these parameter values are compared in Fig. 15 with the measurements of yield ratios: p/π and K/π , for different centralities (expressed by particle density). The conclusion is that the measured proton yield for central Pb–Pb collisions at the LHC is by a factor of about 1.5 lower than predicted. In order to describe the proton measurement, significantly lower T_{ch} is needed (about 152 MeV), but then the yields of multi-strange baryons are underestimated. Trying to fit the temperature to the available data gives an estimate of $T_{ch} \approx 156$ MeV, however, the fit description is not as good as it was at lower energies. Moreover, it is hard to expect that the chemical freeze-out temperature would decrease at higher energy.

It seems that such problems were there partly already at RHIC. The discrepancy being smaller, and uncertainties in proton-yield corrections, lead to the fact that it was considered not significant. There are few attempts to explain the lower proton yield at the LHC:

- The baryons can annihilate in re-scattering with antibaryons, even after chemical freeze-out. This will affect protons more than strange baryons, because protons have larger density, and the annihilations with a strange partner are penalized due to presence of kaon(s) in final state, which shrink the phase space and thus lower the cross section of such cross-flavour annihilation. The effect was confirmed with UrQMD calculations [47, 79, 80], and the particle density makes it larger at the LHC than at RHIC. It was also shown that multi-meson interactions, recreating the baryon–antibaryon pairs, are not, at decreasing temperature, effective enough to compensate the loss [81].
- The statistical hadronization model assumes strictly the same T_{ch} for all particles, which may not necessarily be true. Motivated by recent lattice QCD calculations, flavour- and mass-dependent prehadronic states in QGP may alter the effective phase-transition temperature resulting in a non-uniform freeze out [82]. This will consequently modify the yields predicted by the model.

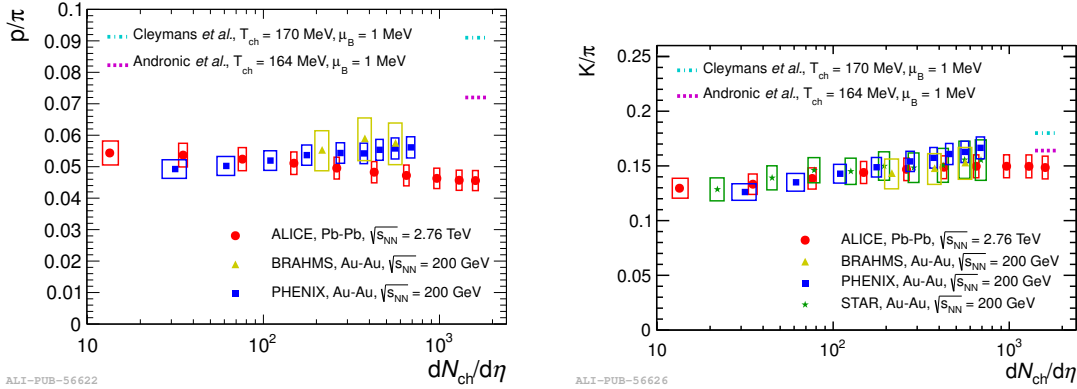


Figure 15: Ratios of proton-to-pion (left) and kaon-to-pion yields at mid-rapidity as a function of charged-particle density in Pb–Pb collisions compared to the RHIC measurements [77, 28, 78]. Reproduced from [42].

- The high-mass resonances, not accounted for in the model, would presumably increase mostly the pion yield. Because of the number of these resonances can raise exponentially with the mass [83, 84], even their production being exponentially damped, the effect may be non-negligible. This would lower the p/π model prediction [73].
- The statistical hadronization model can be modified, incorporating non-equilibrium effects. In fact the model was used also to describe particle yields in pp, and even in e^+e^- , interactions, however, an additional parameter suppressing strangeness production had to be used. Introducing two parameters regulating the population of phase space, separately for light-quarks and strange quark, allows for good description of the experimental measurements. [85, 86]

The lower-than-expected proton yield observed at the LHC was one of the first surprises from the heavy-ion programme, and its origin has yet to be established.

4 Non-flow correlations

In this section various types of particle correlations, which are not caused by a collective behaviour developed in strongly interacting matter, are discussed. These are typically two-, or a few-, particle correlations arising due to a quantum interference, an interaction between the particles, a common source of production, such as a resonance decay, and a string or (mini-)jet fragmentation. The study of this type of correlations gives information about the space–time evolution of the system, and may shed light on particular production mechanisms.

4.1 Femtoscopic correlations

The term femtoscopy is often employed to indicate methods to measure spatial and time scales at a $\mathcal{O}(1)$ fm level. Basically, two effects are exploited: interference between identical particles and final state particle interactions. The identical-particle interference is consequence of the symmetrization of the wave function. It is connected to the Hanbury-Brown and Twiss (HBT) method proposed to measure stellar sizes [87], therefore it is sometimes called also in the heavy-ion field HBT method. The production of identical bosons (e.g. pions) with close momenta will be enhanced by such an effect, and that of identical fermions (e.g. protons) will be suppressed. The correlation length in the momentum space is inversely proportional to the spatial size of the source region, assuming that the particles are

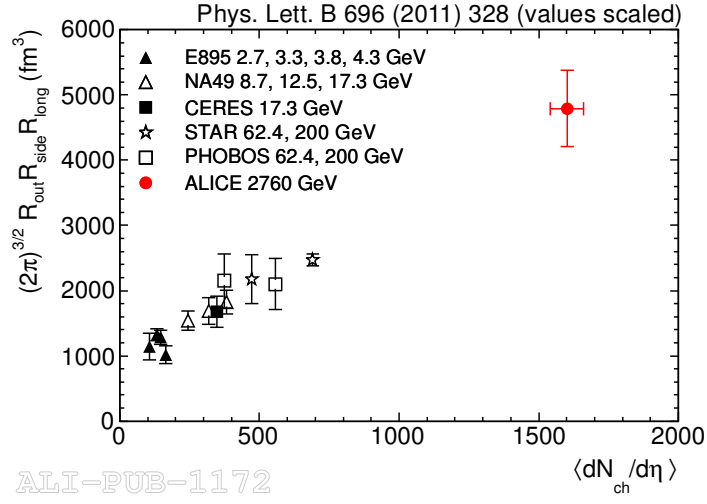


Figure 16: Homogeneity volume for $k_T = 0.3$ GeV as a function of the charged-particle density, measured in heavy-ion collisions at different energies. Adapted from [88].

emitted incoherently. However, the measured correlation is affected by other effects, such as Coulomb interactions, resonance decays, and final state particle interactions, which have to be duly taken into account in the analyses. The latter effect, being often of a short-range nature and present also for non-identical particles, can itself be exploited for femtoscopic studies.

The first results were obtained for like-sign pion–pion correlations with early Pb–Pb data at the LHC [88]. The analysis was performed in three dimensions, decomposing the relative momentum between the two pions in the longitudinally co-moving system (centre-of-mass system boosted along the beam direction such that the two-pion longitudinal momentum is zero) into its ‘out’ (direction of the momentum of the pion pair), ‘side’ (direction perpendicular to the pair momentum and the beam axis), and ‘long’ (along the beam axis) components. The like-sign two-particle distribution in the three-dimensional relative momentum is normalized to that obtained for pairs of particles from different events (event mixing). At small relative momentum the correlation function exhibits the Bose–Einstein enhancement peak, which is fitted with an expression accounting for the incoherent pion emission from a three-dimensional Gaussian-density source and Coulomb repulsion between particles. As a result the Gaussian HBT radii R_{out} , R_{side} , and R_{long} are extracted. The analysis is performed as a function of k_T (one-half of the total pair transverse momentum). The HBT radii are found to be significantly larger (by 10–35 %) than those measured at RHIC [89], and show a decreasing trend with increasing k_T , as also observed in heavy-ion collision experiments at lower energies [90]. This is a characteristic feature of expanding particle sources since the HBT radii describe the homogeneity length rather than the overall size of the particle emitting system. The homogeneity length is defined as the size of the region that contributes to the pion spectrum at a particular momentum.

The energy dependence of the HBT radii is usually expressed as a function of the cubic root of the charged-particle pseudorapidity density, i.e. as $(dN_{ch}/d\eta)^{1/3}$. The approximately linear increase (at a given k_T) is well-described by hydrodynamical calculations [91, 92]. The product of the three radii, measured at different energies at $k_T = 0.3$ GeV, is shown in Fig. 16 as a function of the charged-particle pseudorapidity density $dN_{ch}/d\eta$. This product, multiplied by a factor $(2\pi)^{3/2}$ due to Gaussian distribution normalization, representing then the homogeneity volume, increases linearly with the particle density. At the LHC the homogeneity volume for pion emission for the 5 % most central Pb–Pb collisions doubles compared to that at the top RHIC energy. Within a hydrodynamic scenario the decoupling time for hadrons (τ_f , corresponding to kinetic freeze-out) can be extracted from the k_T dependence of R_{long} ($\tau_f \propto R_{\text{long}}$) [93]. The decoupling time, estimated this way for different collision energies, is

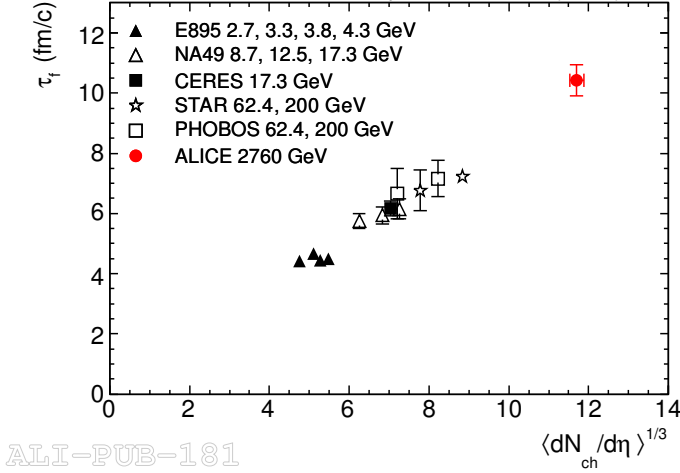


Figure 17: Decoupling time as a function of the cube root of charged-particle pseudorapidity density, measured in heavy-ion collisions at different energies. Reproduced from [88].

presented in Fig. 17. It increases linearly with $(dN_{ch}/d\eta)^{1/3}$, and reaches for most central LHC collisions a value by a factor 1.4 larger than was observed at RHIC. Note that the estimate for τ_f was done for an assumed kinetic freeze-out temperature $T_{kin} \approx 120$ MeV, if one were to use the latest measured value (Sec. 3.2), the decoupling time would increase to 13–14 fm.

In the study of two-pion correlations, the assumption was that the pion emission is incoherent, i.e. the source is fully chaotic. In such conditions the strength of the Bose–Einstein correlations is maximal, and would decrease for a source with a lower degree of chaoticity. Such a situation may be created in heavy-ion collisions, if some kind of condensate would be present or formed (e.g. colour-glass condensate, disoriented chiral condensate). The degree of chaoticity can be assessed comparing two- and three-pion correlations. A recent analysis [94] found that the genuine three-pion correlation is suppressed relative to the two-pion correlation, assuming fully chaotic pion emission. This suppression decreases with pion-triplet momentum, and at low momentum (pion $p_T \sim 0.3$ GeV) may correspond to a coherent fraction in charged pion emission of $(22 \pm 12)\%$.

4.2 Fluctuations

Study of event-by-event fluctuations provides a tool to characterize the thermodynamic properties of the system. Such fluctuations are also affected by the system evolution. The fluctuations of conserved quantities in a finite phase space window, such as the net charge of the system described in [95], are predicted to be sensitive signals of QGP formation and of the phase transition and may provide an important insight on the properties of strong interactions. In the QGP phase, the charge carriers are quarks with their fractional charges, whereas particles in the hadron phase carry unit charge. The fluctuations in the net charge depend on the squares of the charge states present in the system. Consequently, the net-charge fluctuations in the QGP phase are expected to be significantly smaller compared to those in the hadron phase. The event-by event fluctuations of the net charge in a specific phase-space window (for example a given pseudorapidity interval around mid-rapidity) are usually quantified by the D variable [96], defined as:

$$D = \langle N_+ + N_- \rangle \langle \delta(N_+/N_-)^2 \rangle \approx 4 \langle \delta(N_+ - N_-)^2 \rangle / \langle N_+ + N_- \rangle. \quad (2)$$

Here $N_{+,-}$ are the numbers of particles of the two charges in that window, angle brackets denote the average value over the ensemble of events, and δ indicates the variance of the quantity under the square

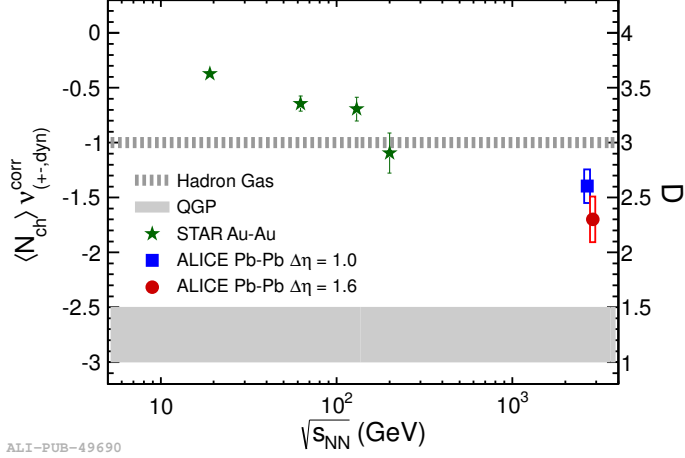
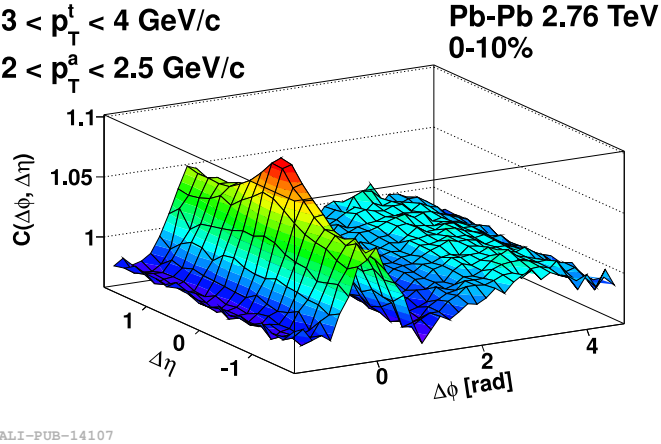


Figure 18: Energy dependence of net-charge fluctuations represented as D-measure (defined in the text) in the most central collisions. The two ALICE measurements are for two different pseudorapidity intervals $\Delta\eta$ centred around mid-rapidity, and the STAR results are for $\Delta\eta = 1$. The D values are shown on the right-hand ordinate and the shaded areas correspond to the two predictions according the legend. The quantity of the left-hand side ordinate represents the way how the D values are measured, and it is not discussed here. Reproduced from [95].

sign. The value of D measures the fluctuation of the net charge ($N_+ + N_-$) per entropy unit, and is predicted to be around 3 for hadron gas and significantly lower, 1–1.5, for the QGP phase [97]. Figure 18 presents the energy dependence of the D measure obtained by the STAR experiment [98] at RHIC and by ALICE at the LHC in the most central collisions. The fluctuations are expected to be diluted during the medium evolution and thus the D measure may not reach the value predicted for the QGP phase, however, a clear tendency going closer to that prediction with increasing energy is observed.

Event-by-event fluctuations of the mean transverse momentum of charged particles are studied as a function of the charged-particle multiplicity in Pb–Pb collisions with the ALICE experiment, and significant non-statistical fluctuations are observed. The dynamical mean p_T fluctuations arise from correlations among the p_T of the final-state particles, e.g. due to resonance decays, jets, or quantum correlations. To account for such conventional contributions, similar studies are performed in pp, where these correlations are also present. These fluctuations are expected to decrease with increasing particle density (collision centrality), as $(dN_{ch}/d\eta)^{-1/2}$ under the assumption of independent sources. The measured dependence for peripheral collisions (corresponding to centrality percentiles in the range 60–90 %) follows the pp extrapolation, however, already there the particle-density dependence has a power close to -0.4 instead of $-1/2$. This is interesting, because significant differences in the mean p_T are observed between pp and Pb–Pb in that multiplicity range [99]. At larger particle densities the Pb–Pb fluctuation results deviate from the pp extrapolation: an enhancement in the 40–60 % centrality range is followed by a pronounced decrease for more central events, which indicates a strong reduction of fluctuations towards central collisions. This centrality dependence is compatible with that observed at RHIC [100]. The Pb–Pb data can not be described by models based on independent nucleon–nucleon collisions such as HIJING [101, 102]. Models which include initial state density fluctuations and their effect on the development of collectivity in the final state such as AMPT [103] are in reasonable qualitative agreement with the data. This suggests a connection between the observed transverse momentum fluctuations and azimuthal correlations, and their relation to fluctuations in the initial state of the collision.



ALICE-PUB-14107

Figure 19: Example of the two-particle correlation function in $\Delta\varphi$ and $\Delta\eta$ for trigger and associated particle selected in p_T intervals displayed in the upper-left corner. The top 10 % of most central Pb–Pb collisions are used. Reproduced from [104].

4.3 Angular correlations

The angular correlations between two particles are widely used to study various phenomena of both non-flow and collective-flow origin. Here, the method and some applications to non-flow studies is described. The exploitation of the angular correlations for investigation of the azimuthally-dependent flow is explained in Sec. 5. The two-particle correlation between pairs of particles is measured as a function of the azimuthal difference $\Delta\varphi$ (defined usually within $\pi/2$ and $3\pi/2$) and pseudorapidity difference $\Delta\eta$. Various kinds of particle pairs are used: they can be all charged particles, pairs selected by charge (like sign, unlike sign), pairs when one particle (trigger) has given p_T or type while the second particle (associated) may have some other characteristics, etc. The two-dimensional distribution is constructed for pairs of particles from the same event, and basically two types of the normalization are used: each event is normalized (per number of pairs, or number of triggers) and then the events are summed up, or the events are first summed up and then normalized to the total number (of pairs or triggers). Therefore, one has to be careful, when comparing the results from different experiments, which may have employed different normalization. Then a second two-dimensional distribution is constructed for pairs of particles from the different events (or a trigger particle form one event and all associated from another one). This mixed-event distribution is usually uniform in the $\Delta\varphi$ direction and has a triangular shape in the $\Delta\eta$ direction, reflecting the geometrical acceptance: maximum at $\Delta\eta = 0$, dropping to zero at $\Delta\eta = \pm$ the detector size in pseudorapidity. The second distribution is normalized to unity at its maximum (i.e. at $\Delta\eta = 0$), and then used to divide the normalized distribution obtained for particle pairs from the same event. In this way, the acceptance and detection efficiency are taken into account.

An example of such two-dimensional two-particle particle correlation is illustrated in Fig. 19. This is obtained for trigger–associated particle pairs selected according their p_T as indicated in the figure. Some typical structures are apparent:

- the peak around $(\Delta\varphi, \Delta\eta) = (0, 0)$ is due to (mini-)jets, sometimes a much narrower peak is also visible on top of that, caused by HBT correlations (for like-sign pairs), or by gamma conversions (for unlike-sign pairs);
- the near-side ridge at $\Delta\varphi = 0$ continuing from the jet peak along the $\Delta\eta$ direction to larger $\Delta\eta$ values, this is presumably caused by the elliptic and higher-harmonic flow (see Sec. 5);
- the away-side ridge at $\Delta\varphi = \pi$ along the $\Delta\eta$ direction, where the second jet may appear (often

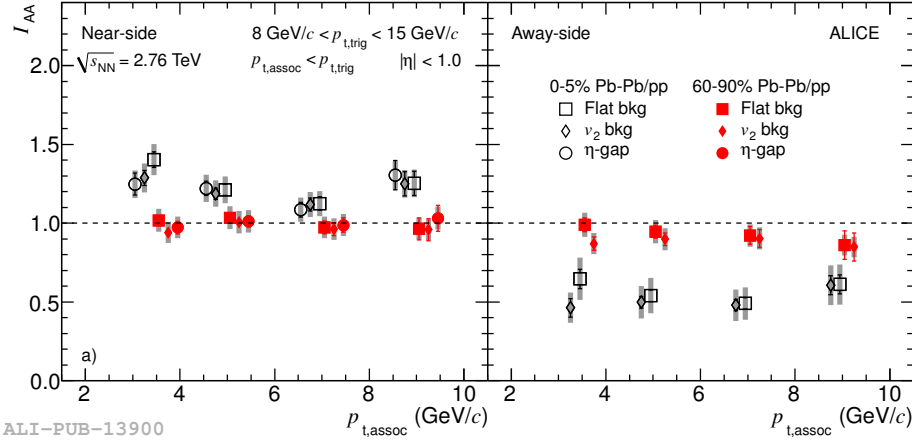


Figure 20: Near-side (left) and away-side (right) I_{AA} as a function of the transverse momentum of associated particles. The results are shown for peripheral (60–90 %) and central (0–5 %) Pb–Pb collisions. The three values shown for each measurement correspond to the three background subtraction methods described in the text. Reproduced from [105].

quenched), now spread along $\Delta\eta$ because the parton–parton system at the origin of the two jets moves longitudinally with respect to the collision centre-of-mass system, in addition the flow azimuthal modulation also contributes here.

The angular two-particle correlations are analyzed by studying their centrality development, and often by projecting them on one of the axes, excluding or not some structures discussed above.

The two-particle correlations are used to study parton quenching at p_T below $\mathcal{O}(10)$ GeV [105], where the full jet reconstruction is difficult due to background fluctuations [106]. In the example shown here the selection requires: a trigger within $8 < p_T^t < 15$ GeV while the associated p_T^a is a variable parameter, respecting $p_T^a < p_T^t$. The two-dimensional correlation is projected on the $\Delta\varphi$ axis in order to measure the number of associated particles correlated to the trigger particle in the near-side and the away-side jet structures. The background from the underlying event, possibly modulated by elliptic flow, has to be subtracted. This is done using three methods: a flat background obtained by the ZYAM (Zero Yield At Minimum) method (the minimum between the near- and the away-side peaks is used to evaluate the background level), a background modulated according the available elliptic-flow v_2 measurements, and a flat background estimated according to the value in the region $|\Delta\varphi| < \pi/2$ and $|\Delta\eta| > 1$ ($\Delta\eta$ -gap). After background subtraction the distribution is integrated around the near- and away-side peaks, in the ± 0.7 and $\pi \pm 0.7$ $\Delta\varphi$ intervals, respectively. The per-trigger yields of associated particles, obtained this way, are normalized to the same yields measured in pp collisions. Such a ratio is denoted I_{AA} and it represents the nuclear modification factor of the conditional yields. In Fig. 20 the near- and away-side I_{AA} are presented as a function of associated-particle p_T^a for peripheral and central Pb–Pb collisions. The results are practically independent on p_T^a , and for peripheral collisions compatible with unity, i.e. no nuclear modification is observed. For central collisions, the away-side I_{AA} is around 0.6, which is interpreted as a manifestation of jet quenching. On the near-side the I_{AA} is above unity, such an effect was not observed at lower energies. The near-side enhancement could be understood as due to a modification of the fragmentation function, possibly caused by jet quenching and a trigger bias. This measurement constrains various models, some of those showed to be capable to describe such an enhancement [107].

The jet-shape studies measuring the jet-structure widths in $\Delta\varphi$ and $\Delta\eta$ directions, exploited the triggered two-particle correlations as well. It was reported that the $\Delta\eta$ jet-structure size increases for more central Pb–Pb collisions, while in the $\Delta\varphi$ direction such an increase, if any, is much smaller.

This could be explained by an interaction of the jet with longitudinally flowing medium. The particle composition of the jet-like structure was also studied. The p/ π ratio is measured in $(\Delta\varphi, \Delta\eta)$ regions, both outside and inside the jet structures selected in the correlation plot. Correcting the jet region with properly weighted outside-jet measurement, the p/ π ratio for the jet structure is obtained. While the outside-jet p/ π ratio reproduces the heavy-ion baryon anomaly (see Sec. 3.2), the result for the jet structure is compatible with the expectation for the jet fragmentation in pp collisions.

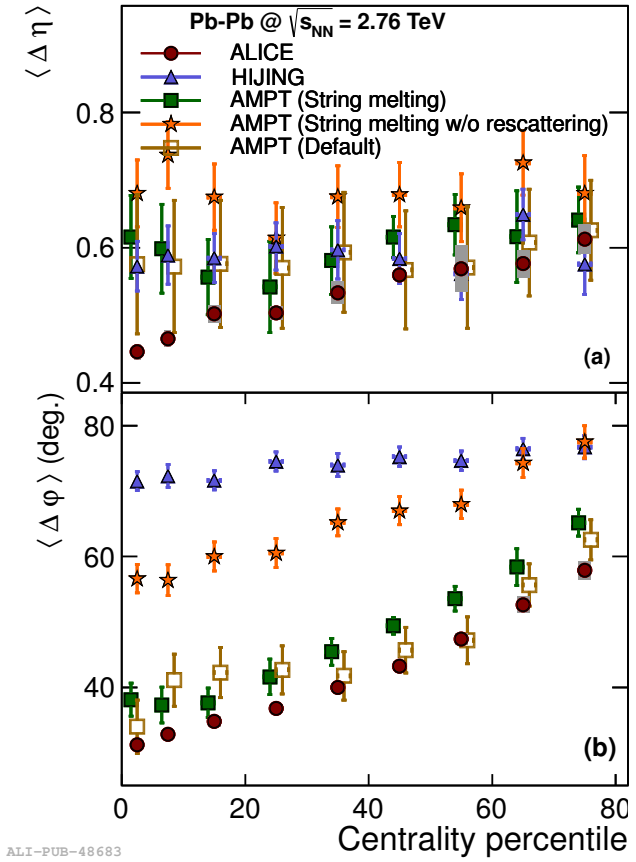


Figure 21: Charge balance function widths in longitudinal (upper part - a) and azimuthal (lower part - b) directions as a function of collision centrality, expressed in percentiles. Model calculations are presented with markers according to the legend. Reproduced from [108].

The study of the charge balance function is performed using the correlations constructed for unlike-sign and like-sign particle pairs separately [108]. The balance function is defined as one half of the difference between the unlike-sign and like-sign correlations, and measures the distance over which the charge of particles is compensated. The widths of the balance function in the two directions, $\langle \Delta\varphi \rangle$ and $\langle \Delta\eta \rangle$, are shown in Fig. 21 as a function of the collision centrality. The measurement indicates that the charge is compensated in both directions on a shorter scale for more central collisions. Such behaviour was already observed at RHIC [109], however, the $\langle \Delta\varphi \rangle$ and $\langle \Delta\eta \rangle$ values are significantly larger at the LHC. The model calculations [101, 103] presented in Fig. 21 have difficulties to reproduce the centrality dependencies in both directions.

4.4 Chiral magnetic effect

Under the influence of the strong magnetic field along the direction of the angular momentum generated by the colliding nuclei, the quark spin alignment and the imbalance of the left- and right-handed quarks,

Figure 22: Centrality dependence of the multi-particle correlator defined in text as $\langle \cos(\psi_{\pm,\alpha} + \psi_{\pm,\beta}) \rangle$. The ALICE results are obtained from the cumulant analysis. The triangles represent the three-particle correlations from HIJING [101] corrected for the experimentally measured v_2 . A model prediction for the like-sign correlations incorporating the chiral magnetic effect for LHC energies [115] is shown by the solid line. The shaded band represents the centrality dependence of the charge independent correlations. Reproduced from [113].

would generate an electromagnetic current [110, 111, 112]. Subsequent quark fragmentation into charged hadrons may induce a charge separation along the direction of the magnetic field (perpendicular to the reaction plane, defined by the beam axis and the centres of the colliding nuclei). This phenomenon is called the Chiral Magnetic Effect (CME). Azimuthal correlations among particles provide a powerful tool for the experimental study of particle production with respect to the reaction plane [113].

Let's denote by ψ_{\pm} the azimuthal angle of a particle of given charge with respect to the reaction plane. The orientation of the reaction plane itself is estimated by different techniques used in the studies of azimuthal asymmetry, Sec. 5. The multi-particle correlator $\langle \cos(\psi_{\pm,\alpha} + \psi_{\pm,\beta}) \rangle$ ('multi-particle' because it depends on the reaction-plane angle, determined with other particles) probes the magnitude of the parity-odd amplitude possibly present in the azimuthal distribution with respect to the reaction plane [114]. Such correlator also suppresses the background (non-flow) correlations unrelated to the reaction plane. It can be expressed as the difference of two terms: $\langle \cos \psi_{\pm,\alpha} \cos \psi_{\pm,\beta} \rangle$ and $\langle \sin \psi_{\pm,\alpha} \sin \psi_{\pm,\beta} \rangle$, the latter term quantifies the out-of-plane (i.e. in the direction of magnetic field) charge correlations sensitive to the CME. In order to evaluate the two terms separately, the two-particle correlator $\langle \cos(\psi_{\pm,\alpha} - \psi_{\pm,\beta}) \rangle$ is used, which is independent of the reaction plane angle, however, susceptible to large background contributions. This second correlator is equal to the sum of the two terms mentioned above. It should be mentioned that both correlators could be affected by other effects, such as momentum conservation, local charge conservation, and fluctuations in the initial energy density.

The centrality dependence of the multi-particle correlator $\langle \cos(\psi_{\pm,\alpha} + \psi_{\pm,\beta}) \rangle$ for like-sign (labeled as 'same') and unlike-sign (labeled as 'opp.') particle pairs is presented in Fig. 22. The contribution from the CME to the correlations of like-sign and unlike-sign pairs is expected to be similar in magnitude and opposite in sign, however, these correlations could be modified by the medium, that may result in the dilution of the correlations for unlike-sign particles. The LHC results are (unexpectedly) compatible with the RHIC measurements [116]. This is not true for the second (two-particle) correlator, may be due to different background contributions. In Fig. 22 the experimental results are compared to a model prediction for like-sign correlations [115], which predicts a significantly smaller effect at the LHC than at RHIC. The magnitude of the effect and its energy dependence crucially rely on the duration and time evolution of the magnetic field, which is at present a matter of intense discussions. To conclude, a clear signal compatible with a charge-dependent separation relative to the reaction plane is observed and can be used to constrain theoretical calculations.

5 Flow correlations

5.1 Introduction

While the previous section covered physical mechanisms which induce correlations between multiple hadrons, this section covers the phenomenon of "collective flow", which leads to the correlations of essentially all the particles in every event. This results from the translation of anisotropies in the initial shape of the colliding nuclei into anisotropies in momentum space, something that would not occur if individual nucleon-nucleon collisions emitted independently of each other. The characterization of a "shape" in a final state particle distribution is typically performed using a Fourier decomposition

963 of the azimuthal angle distribution of final state particles. Of course, averaging over an ensemble of
964 independent events would lead to the observation of no net anisotropy. Thus, the presence of harmonic
965 oscillations in the final state requires the estimation of an “event plane” from the particle themselves,
966 with an axis that points in the direction of the largest momentum flow.

967 While this phenomenon was observed decades ago in the collisions of large nuclei at low energies,
968 this was straightforward to understand as the reinteraction of the initial baryons and the produced
969 hadrons, which would thermalize and evolve as a “hadron gas”. However, its persistence at higher
970 energies, particularly at RHIC where the value of v_2 averaged over p_T was approximately twice as large
971 as it was at the CERN SPS [117], surprised many who expected the hot system to become more dilute
972 and more weakly-interacting at higher energies.

973 Collective flow was a major piece of the RHIC program, and its characterization in terms of hydrody-
974 namics was a crucial piece of evidence in the RHIC discovery of the strongly-coupled quark gluon plasma
975 (sQGP) [118, 119, 120, 121]. Crucial aspects of collective flow, on the experimental and theoretical sides
976 at RHIC, have been:

- 977 • Based on theoretical calculations, the average elliptic flow, scaled by the eccentricity, is thought
978 to reach a limiting value in the limit where the viscosity can be ignored. RHIC data achieved
979 this limit both integrally (integrated over p_T) and for $v_2(p_T)$, which rises linearly until viscous
980 corrections become large.
- 981 • When studied as a function of particle type, it is found that heavier particles show a smaller v_2
982 at the same p_T at low p_T , while this hierarchy flips above 1.5 GeV, where protons typically have a
983 50% higher value of v_2 . This behavior has been explained by the hadronization of the system via
984 constituent quarks which recombine into baryons with $v_2(\text{baryon}) = (3/2) \times v_2(\text{meson})$ [122, 123].
- 985 • The deviations from ideal behavior can be systematically calculated by viscous corrections, and
986 all RHIC data point to a small but significant value of the ratio of shear viscosity to entropy
987 density (η/s) [124].
- 988 • While difficult to calculate in the strongly-coupled limit, where the approximations required for
989 kinetic theory break down, AdS/CFT-based calculations have shown that a wide range of strongly-
990 coupled systems have a lower-bound on $\eta/s = 1/4\pi$ [125]. The RHIC experimental data suggest
991 values of 1-2 times this bound, although estimates are limited by theoretical uncertainties related
992 to the modeling of the initial state [124].
- 993 • When studying smaller systems (particularly Cu+Cu), it was found that accounting for the event-
994 by-event position of the nucleons in the nuclear wave functions showed scaling in the quantity
995 v_2/ϵ between Cu+Cu and Au+Au, when plotted as a function of the transverse density of charged
996 particles at mid-rapidity, estimated by $dN_{ch}/d\eta/S$, where S is the overlap area of the two nu-
997 clei [126].

998 5.2 Methods

999 Harmonic flow is a global modulation of essentially all of the particles in an event relative to an
1000 event plane appropriate to each harmonic. However, there are additional sources of multi-particle
1001 correlations, some which lead to global correlations (momentum conservation) and others which only
1002 lead to correlations local in angular space (e.g. resonance decays and jets). Thus, care must be taken
1003 to minimize such “non flow” correlations.

1004 One of the earliest methods for measuring flow was the “event plane” method, which calculates an
1005 event plane using a forward detector and correlates all particles with this event plane, based on the

1006 so-called “Q-vector” for each order n [127]:

(3)

1007 From this, the n -th order event plane Ψ_n is simply determined as the angle of the Q-vector itself. From
 1008 the definition of the Q-vector, the angle is n -fold ambiguous, but this has no effect on the extracted v_n
 1009 coefficient, which is defined as

$$v_n = \frac{v_n^{obs}}{\text{Res}\{n\Psi_n\}} = \frac{\langle \cos(n[\phi - \Psi_n]) \rangle}{\langle \cos(n[\Phi_n - \Psi_n]) \rangle} \quad (4)$$

1010 where Φ_n is the direction of the true event plane. The latter quantity cannot be observed directly and so
 1011 the resolution parameter must be derived from comparison of different detector regions. This is typically
 1012 done by comparing symmetric pseudorapidity regions separated from the region being measured:

$$\text{Res}\{n\Psi_n^{\text{P(N)}}\} = \langle \cos n(\Psi_n^{\text{P(N)}} - \Psi_n) \rangle = \sqrt{\langle \cos n(\Psi_n^{\text{P}} - \Psi_n^{\text{N}}) \rangle} \quad (5)$$

1013 Non-flow contamination is typically most difficult to control when the subevents used to determine the
 1014 event plane and resolution are close in η to each other or close to the measured particles. Another method
 1015 is to use multi-particle cumulants to explicitly remove lower order correlations [128, 129, 130, 131]. These
 1016 can be calculated either from a generating function formalism, or through moments of the Q-vector itself.
 1017 They are more or less sensitive to non-flow depending on the order of the cumulant. For example, the
 1018 two-particle cumulant is quite sensitive to effects from resonance decay and jet fragmentation. However,
 1019 the four particle cumulants are generally much less so, since it explicitly removes short-range two particle
 1020 correlations. A third method is to use the “Lee Yang zeroes” approach, which accounts for correlations
 1021 of all lower orders using a different generating function [132, 133]. The method relates the zeros of a
 1022 complex function to the magnitude of the relevant flow harmonics. While the method is thought to be
 1023 robust against most sources of non-flow, it is particularly sensitive to multiplicity fluctuations, and so
 1024 is calculated using event samples with similar multiplicities within a given centrality interval. These
 1025 subsamples are then averaged within the desired centrality interval to give the final result.

1026 Another approach is to measure two-particle correlations as a function of $\Delta\eta$ and $\Delta\phi$, and decompose
 1027 them into harmonics using either fits or Fourier transformations [134, 104, 135]. If the two-particle
 1028 distribution can be factorized into the product of single particle distributions, $1 + \sum_n v_n \cos(n[\phi - \Psi_n])$,
 1029 then the two particle distribution, for $\Delta\eta$ regions selected to suppress jets and other sources of non-flow,
 1030 takes the form:

$$\frac{dN_{\text{pair}}}{d\Delta\phi} \propto 1 + 2 \sum_n^\infty v_{n,n}(p_T^a, p_T^b) \cos n\Delta\phi \quad (6)$$

1031 Where $v_{n,n}(p_T^a, p_T^b) = v_n(p_T^a)v_n(p_T^b)$.

1032 5.3 Elliptic flow

1033 The first LHC data on elliptic flow was released by the ALICE collaboration soon after the first collisions,
 1034 and is shown in Figure 23. The elliptic flow was estimated using three methods: 2-particle cumulants
 1035 (v_{22}), 4-particle cumulants (v_{24}) and Lee-Yang Zeros (LYZ). The first method is known to be sensitive
 1036 to correlation from jets, which have a larger contribution at the LHC than at RHIC, and the latter
 1037 method was only used for integral flow. The integral flow was found to be larger than that measured at
 1038 RHIC, but only by about 15-20%. What was surprising was that, as a function of p_T (but only measured
 1039 out to 4 GeV) the magnitude of v_2 was found to be quantitatively very similar to that measured in
 1040 the STAR experiment at RHIC, using similar cumulant methods. Although a similar scaling has been
 1041 observed in the very low energy data on inclusive $v_2(p_T)$ from STAR taken during the recent RHIC
 1042 energy scan, there is no fundamental understanding yet of how this scaling arises. It suggests that most

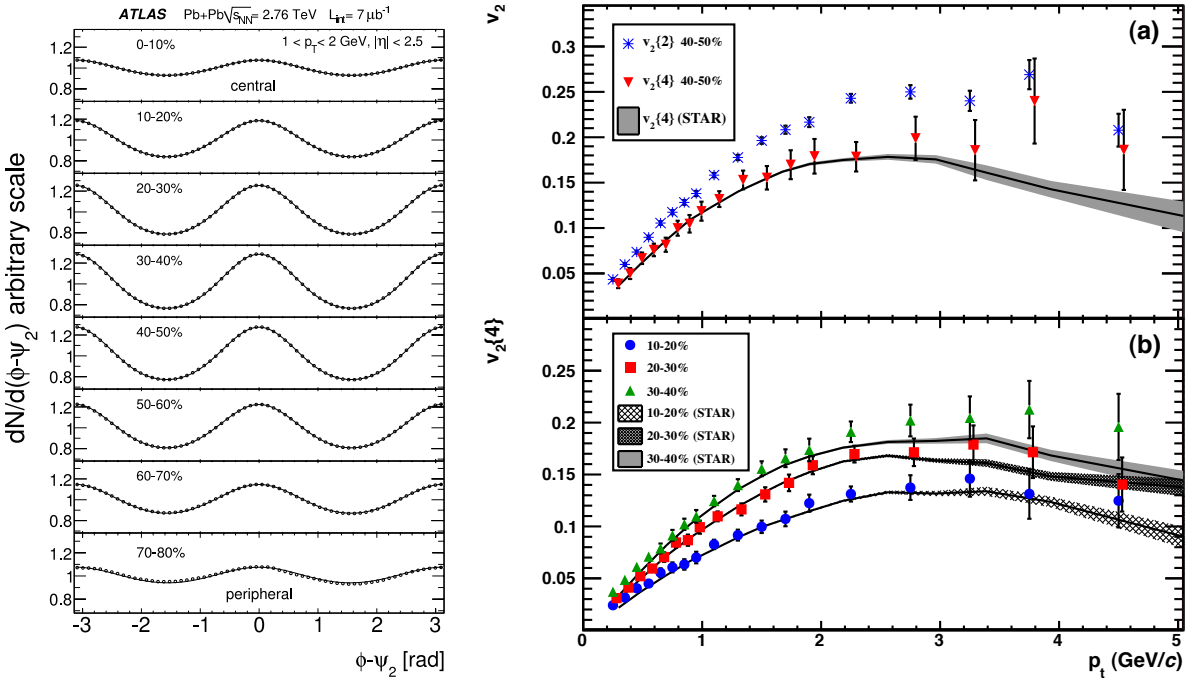


Figure 23: (left) ATLAS data showing the evolution of anisotropy relative to the reaction plane, as a function of centrality [136] (right) First ALICE data on v_2 in Pb+Pb collisions at the LHC [137].

of the variation in the integral elliptic flow results from the change in the spectral shape of inclusive hadrons. A hydrodynamic calculation by Luzum was able to reproduce this result soon after its release, based on a scaling of the initial energy density according to the measured charged-particle multiplicity, and assuming no change in the medium transport properties [138]. The first v_2 measurement at higher p_T was performed by ATLAS [136], showing the transition from the low p_T behavior, understood by viscous hydrodynamics, to the higher p_T values presumably explained by the path-length dependence of energy loss of jets. By comparison with PHENIX data on π^0 particles, this shows that the scaling of v_2 extends to high p_T as well, within the large statistical errors of the lower-energy measurement.

The dependence of the inclusive elliptic flow on the initial state geometry was studied carefully by CMS, who performed a careful extrapolation of the integral v_2 down to $p_T > 0$ GeV, using simultaneous measurements of dN/dp_T , to match with the lower energy PHOBOS data. To factor out the initial shape and size of the overlap region, a Monte Carlo Glauber model was used to match the centrality selections made with the CMS forward calorimeter. From these, the eccentricity and overlap area were calculated according to the definitions from subsection 5.2. The CMS data, shown superimposed on data from RHIC, is shown in Figure 24(right), and overlaps the PHOBOS data in the most peripheral collisions and shows a continuous rise in the more central collisions, except perhaps in the most central interval.

The CMS data shown in Figure 25 illustrates the p_T and centrality dependence of $v_2(p_T)$, comparing directly the different methods of flow reconstruction used for v_2 . While it is clear that the 2-particle cumulant is the most contaminated by non-flow, particularly at high p_T , one also observes some systematic differences between all three methods, particularly where the flow is the strongest.

The previous results have all been for unidentified hadrons. This choice provides the largest phase space coverage (particularly in p_T) and allows for comparisons between experiments with different particle identification capabilities. However, a study separating the different hadron species is crucial, given the previous measurements at RHIC showing the strong differences between them. The ALICE data showing identified particles (separated using the dE/dx measured in the ALICE TPC) for $p_T > 3$

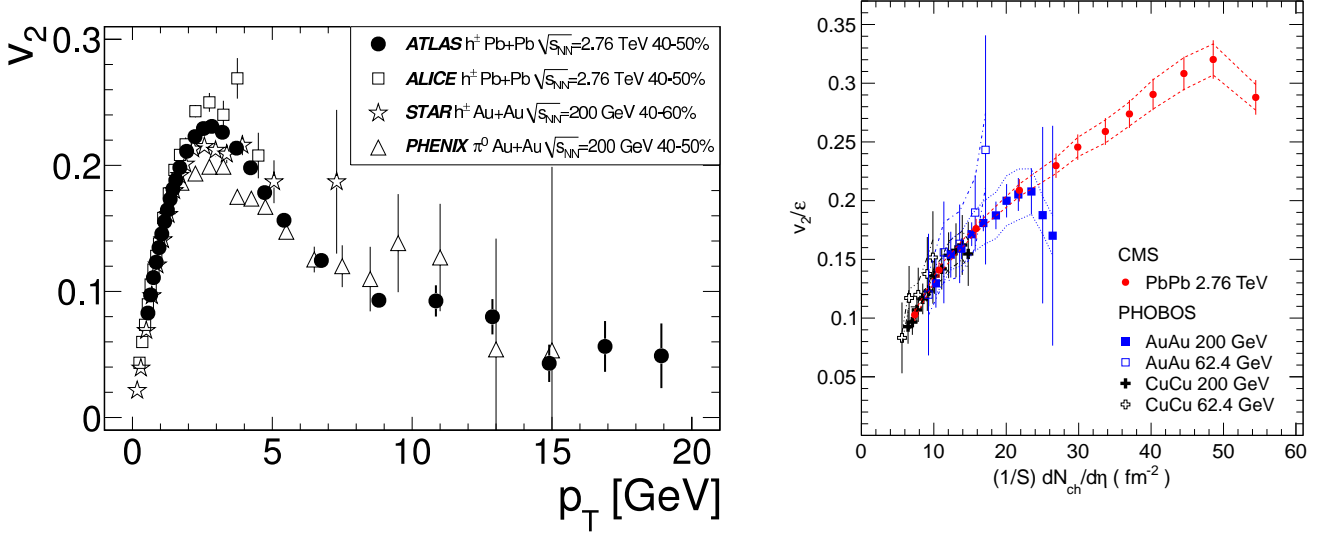


Figure 24: (left) ATLAS data showing the invariance of $v_2(p_T)$ with beam energy [136] (right) CMS compilation showing the observed scaling of v_2/ϵ vs. $(1/S)dN_{ch}/d\eta$ [139].

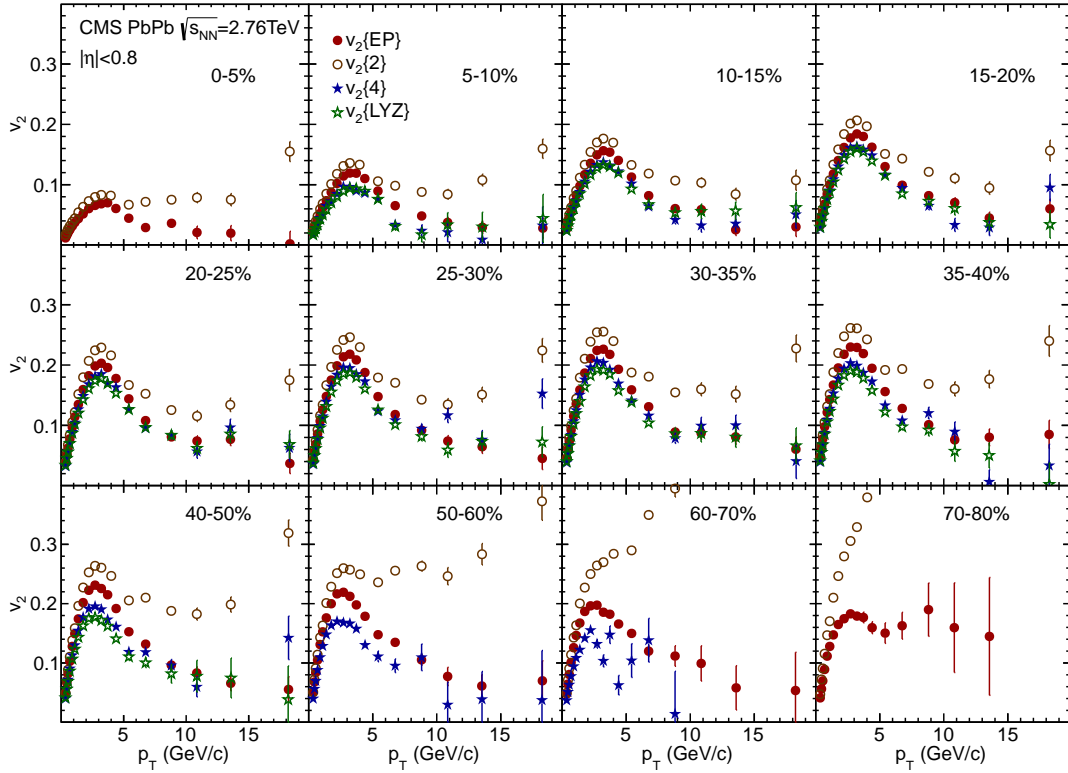


Figure 25: CMS data showing $v_2(p_T)$ in centrality intervals, using four different methods of extracting v_2 : event plane (EP), 2-particle cumulants, 4-particle cumulants, and Lee-Yang Zeros [139].

1069 GeV is shown in Figure 26(left). The charged pion data on $v_2(p_T)$ is quantitatively similar to the
 1070 PHENIX π^0 data over the p_T range where they overlap. The proton-antiproton v_2 are found to be
 1071 substantially larger than the pion values over the measured p_T range, although it is clear that the

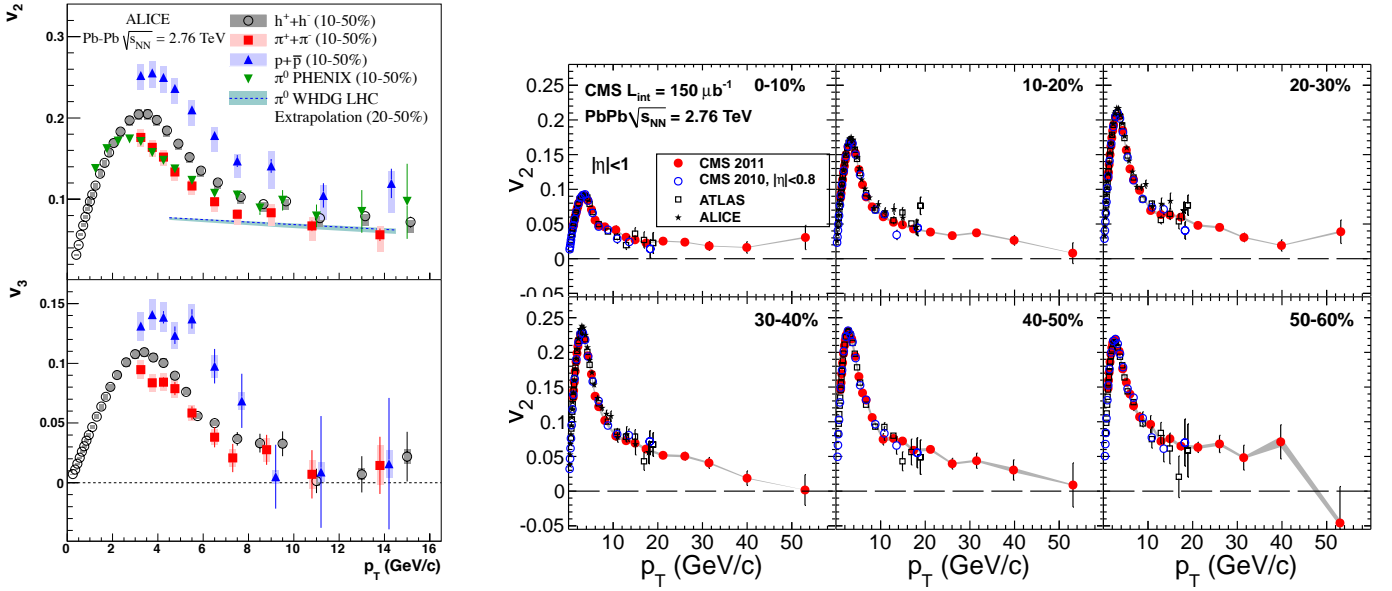


Figure 26: (left) ALICE data showing $v_2(p_T)$ for identified hadrons, for $|\eta| < 0.8$ [140] (right) CMS data showing the v_2 for unidentified hadrons at very high p_T , out to 50 GeV [141]

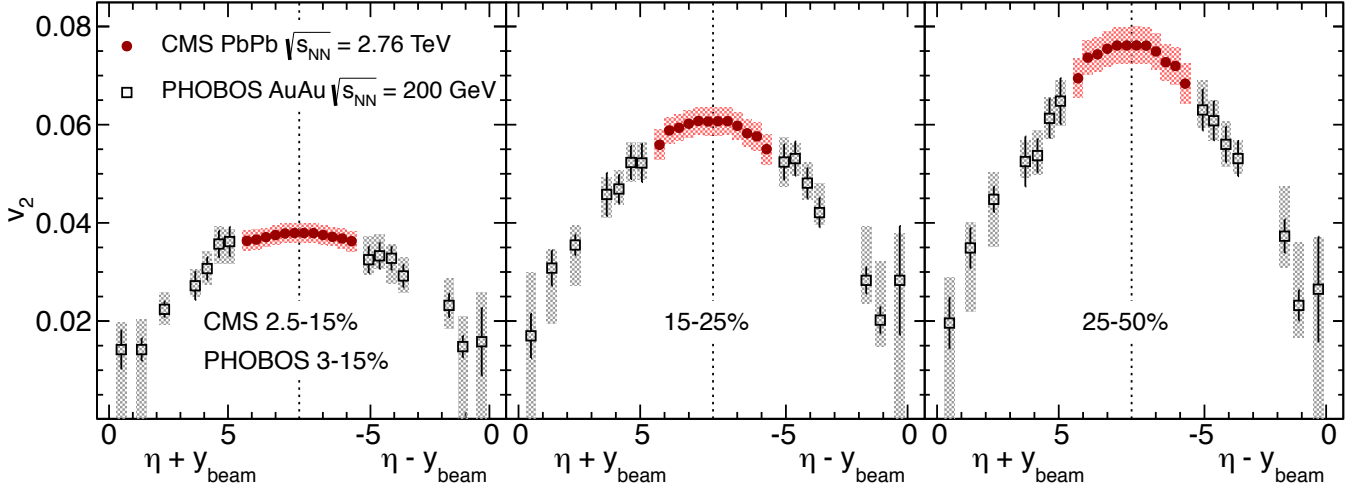


Figure 27: CMS data showing v_2 for unidentified hadrons as a function of $\eta - y_{\text{beam}}$, averaged over $0 < p_T < 3$ GeV (using an extrapolation procedure to cover $p_T < 300$ Mev). Results are compared to data from $\sqrt{s_{\text{NN}}} = 200$ GeV at large η from the PHOBOS experiment at RHIC [139].

peak-plateau structure seen in the inclusive hadron data is not explained primarily by one particular hadron type. Also, at the highest p_T measured, the protons and pions are quite close, although the protons remain systematically higher out to 14 GeV. CMS extends the hadron p_T range out to the full range provided by the LHC in 2011, using a high p_T high level track trigger. The data, shown in Figure 26(right), show that the plateau observed setting in above 6 GeV extends out to 50 GeV, with only mild decreases observed within the stated uncertainties.

Another intriguing way to compare with the lower energy data is suggested by studies performed by the PHOBOS collaboration, which found that the integrated $v_2(\eta)$ is the same for different colliding

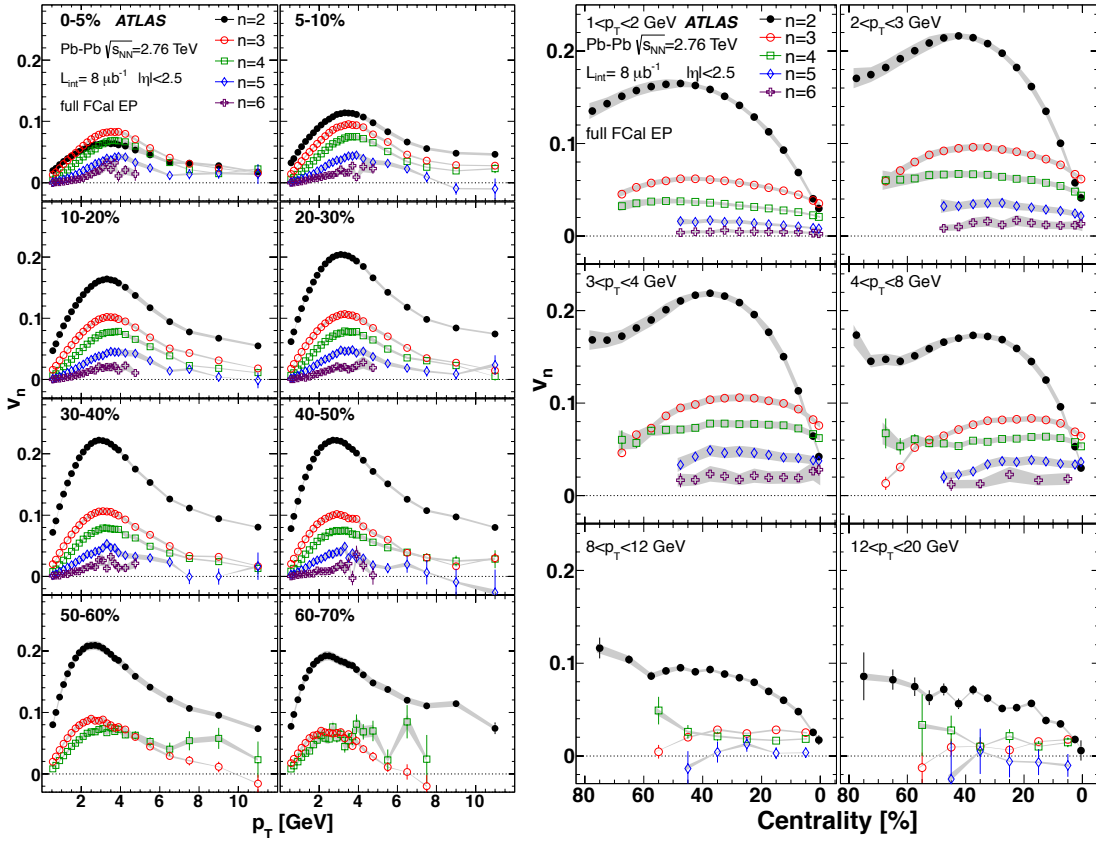


Figure 28: (left) ATLAS data showing $v_n(p_T)$ for different centrality intervals and $|\eta| < 2.5$, for $n = 2–6$. Very little dependence on η is observed [134]. (right) The same ATLAS data, in p_T intervals, showing the approximate centrality dependence of $v_3 - v_6$ [134].

beam energies, when plotted in the rest frame of one of the projectiles. This is the phenomenon of so-called “limiting fragmentation”, where many quantities are found to depend only on their rapidity relative to either beam or projectile. Figure 27 shows $v_2(\eta)$ as a function of $\eta - y_{\text{beam}}$ (in the forward hemisphere) and $\eta + y_{\text{beam}}$ in the backward hemisphere. While the CMS and PHOBOS data points do not overlap in any measured region, they appear to be continuous in the forward LHC kinematics and the mid-rapidity RHIC kinematics. However, it is clear that the behavior of the CMS data is much more suggestive of a boost-invariant central plateau, while the PHOBOS data did not show similar behavior.

5.4 Higher order harmonics

Although the realization that v_2 was sensitive to fluctuations in the nuclear overlap, particularly from the event-wise random positions of nucleons in each nuclei, several more years elapsed before it was suggested to look for higher-order harmonic flow, particularly odd-orders [142, 143]. Many authors argued that symmetric systems would have a zero v_1 , v_3 , v_5 , etc, but had not yet considered the effect of fluctuations. By mid-2011, all of the LHC and RHIC experiments had significant measurements of many of the higher-order contributions, up to v_6 which was the limit of the statistics in the 2010 run.

CMS released the first evidence for the presence of higher-order harmonics in the two-particle correlation function. ALICE released the first measurements of $v_3 - v_5$ up to $p_T = 4$ GeV, using two and four particle cumulants [135], and followed up with an extensive study of two-particle correlations in Ref. [104]. ATLAS released the first large scale study of higher harmonics for unidentified hadrons,

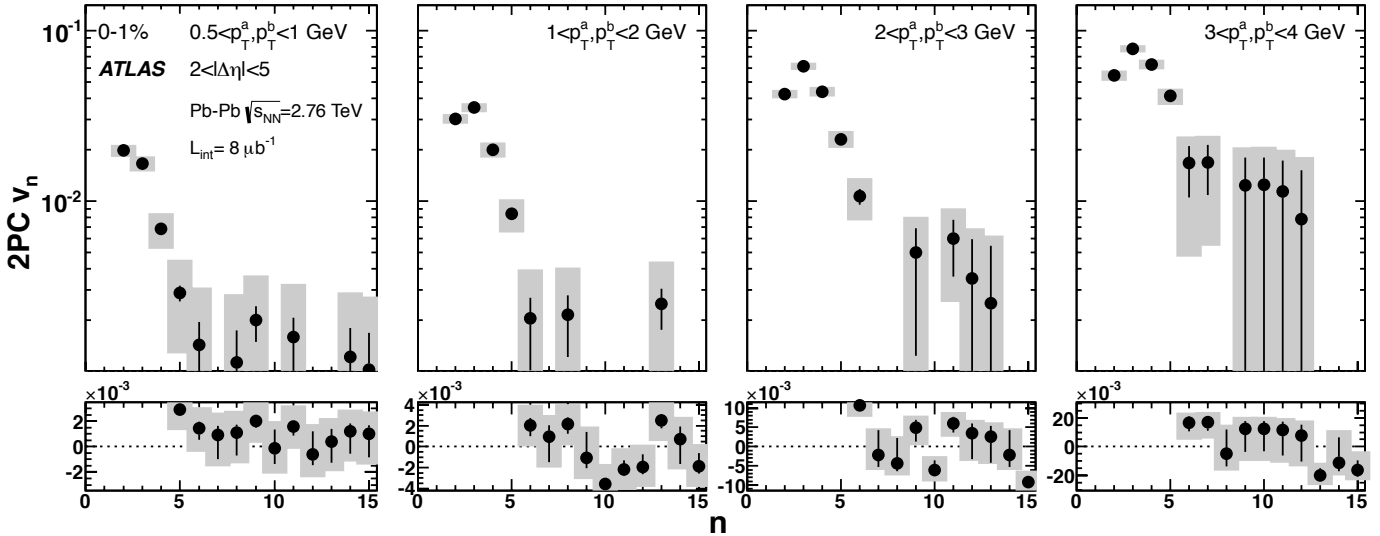


Figure 29: ATLAS data showing the n dependence of v_n in four p_T intervals, which are effectively angular power spectra at different resolution scales.

1099 with the first complete experimental measurements of

1100 The ATLAS data shown in Figure 28(left) and (right) show the harmonics $v_2 - v_6$ as a function of
 1101 p_T in centrality intervals from the most central 0-5% to the most peripheral 70-80%. The the figure on
 1102 the left shows that the pattern is consistently the same for all harmonics: a rapid rise starting at low
 1103 p_T , a peak around 3 GeV, and a rapid decrease out to higher p_T . While all of the experiments have
 1104 demonstrated that v_2 does not necessarily go to zero at high p_T , it remains an open question about
 1105 the higher harmonics, which can only be resolved with higher statistics. The right figure shows the
 1106 centrality dependence in small p_T intervals, demonstrating that v_2 is fundamentally different than the
 1107 higher harmonics, having a much milder centrality dependence. While v_2 mainly reflects the overall
 1108 geometric shape of the system, the higher harmonics seem to mainly reflect fluctuations. However, the
 1109 decrease in magnitude with increasing n is generally thought to reflect the presence of viscous effects.
 1110

1111 Another representation of this data is given in Figure 29, which shows the “angular power spectrum”,
 1112 the n dependence of $v_2(p_T)$ for particular intervals in p_T and centrality. The fall-off with increasing n is
 1113 a general feature, of the data which is expected to be driven by viscous corrections that increase with
 1114 n .

1115 While the two-particle analyses from ALICE, ATLAS and CMS all utilized a $v_{1,1}$ term in their fits,
 1116 the first measurements did not extract a single-particle v_1 contribution, since momentum conservation
 1117 is expected to be a substantial effect. The first published extraction of v_1 from experimental data was
 1118 performed by a theoretical team using published ALICE data, doing a fit of the form $V_{1\Delta}(p_T^a, p_T^b) =$
 1119 $v_1(p_T^a)v_1(p_T^b) - kp_T^a p_T^b$. ATLAS also measure directed flow using a similar approach, fitting $v_1(p_T)$.
 1120 The value of v_1 was also found to vary only modestly with centrality, suggesting it too arises from
 1121 fluctuations.

1122 The two-particle technique was only able to extract the rapidity-even contribution to v_1 , ALICE
 1123 performed an analysis using the Ψ_1 plane determined event-by-event with their ZDCs, which have a
 1124 four-fold transverse segmentation [144]. Figure 31(a) shows the integrated v_1 signal for $p_T > 0.15$ GeV
 1125 as a function of hadron pseudorapidity, where a linear dependence with a negative slope is observed
 1126 for the rapidity-odd v_1 signal, and a constant negative value is found for the rapidity-even v_1 . The
 1127 latter is consistent with the previous extractions of v_1 from both the ALICE and ATLAS data. As seen
 1128 in Figure 31(c) the negative slope is similar to what was found by STAR at two RHIC energies, but
 1129 with a much larger slope, suggesting a much smaller “tilt” angle in the x-z plane at higher energies.

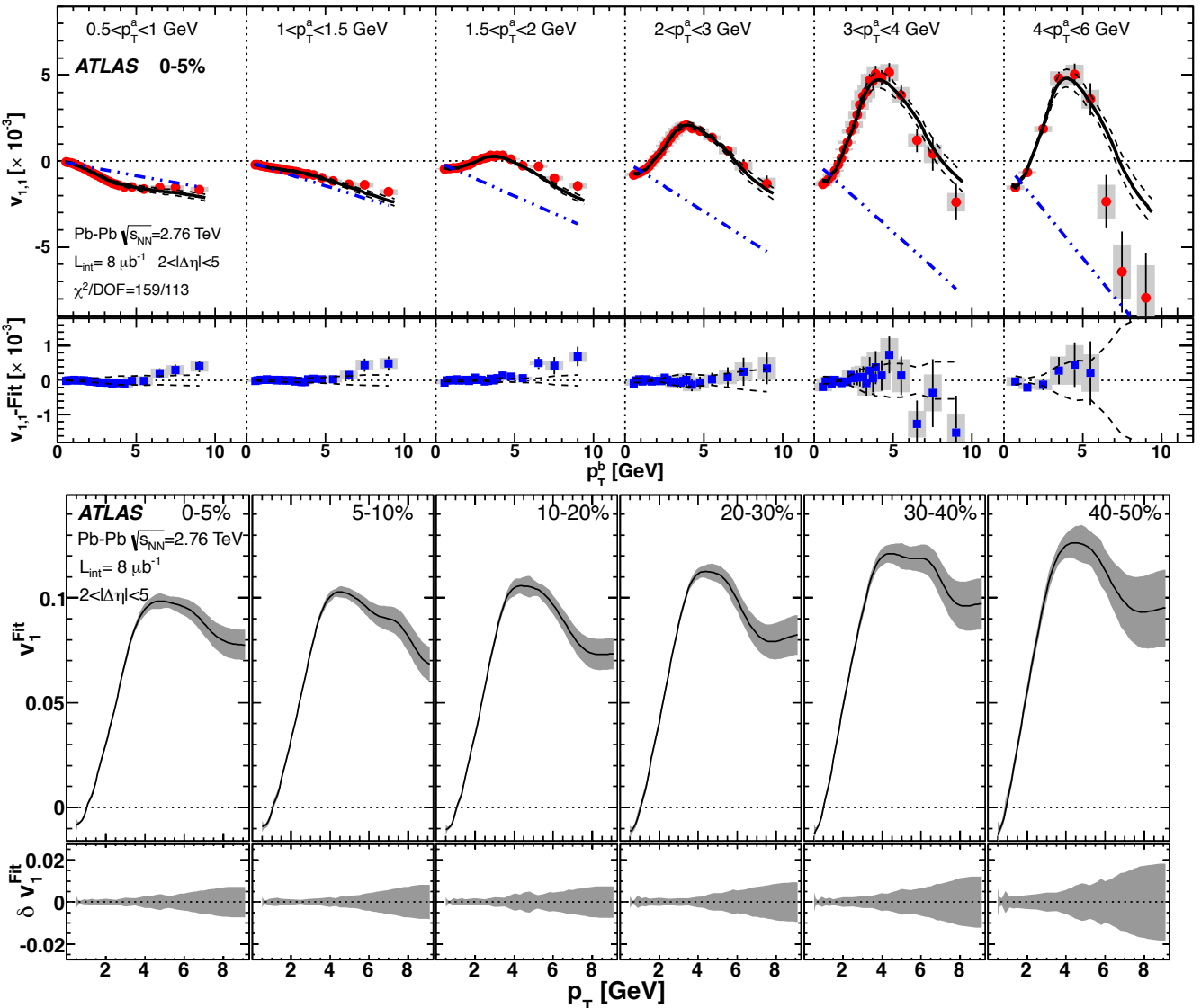


Figure 30: (top) ATLAS data showing the amplitude of $v_{1,1}$ the dipole modulation in the 2-particle correlation function, as a function of p_T^b for ranges in p_T^a . The fit used to extract the functional form of $v_1(p_T)$ is shown [134]. (bottom) The extracted functional form of $v_1(p_T)$, from the fits shown above, as a function of centrality [134].

Figure 31(b) shows the mean relative momentum shift in the spectator plane, illustrating that there is no net momentum flow at $\eta = 0$ but it increases with η proportionally to the v_1 .

5.5 Flow fluctuations

The same geometric fluctuations that lead to the presence of the higher harmonics are also expected to lead to event-by-event fluctuations in the individual coefficients. This has been studied using two methods. ATLAS developed a data-driven method to unfold the measured v_n distributions ($P(v_n)$) with a Bayesian technique [145]. The distributions $P(v_n)$ are shown in Figure 32 for v_2 , v_3 and v_4 for a selected set of centrality intervals. It is clear that the fluctuations are large in all selected samples. Although the distributions are not Gaussian, but are rather projections of a 2D Gaussian (also known as a Bessel-Gaussian distribution), the distributions are typically quantified using the first two moments, the mean and standard deviation. These can also be estimated by combining different estimates of v_n ,

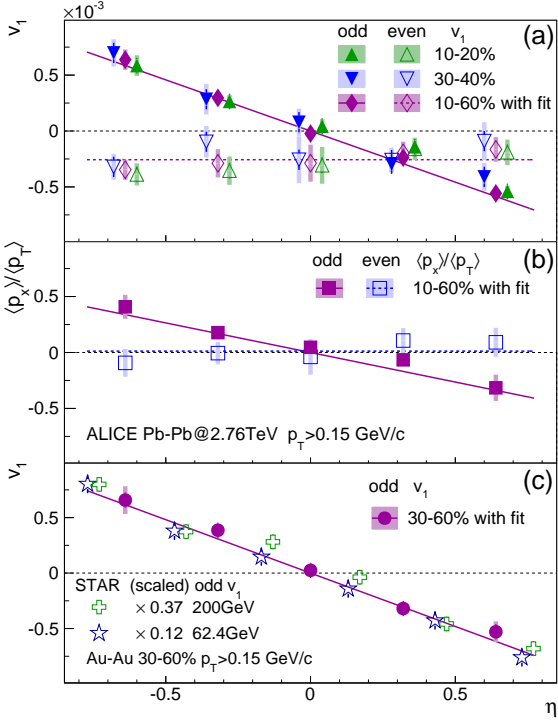


Figure 31: ALICE data on directed flow, measured in the plane determined by spectator neutrons as observed in the ALICE ZDCs.

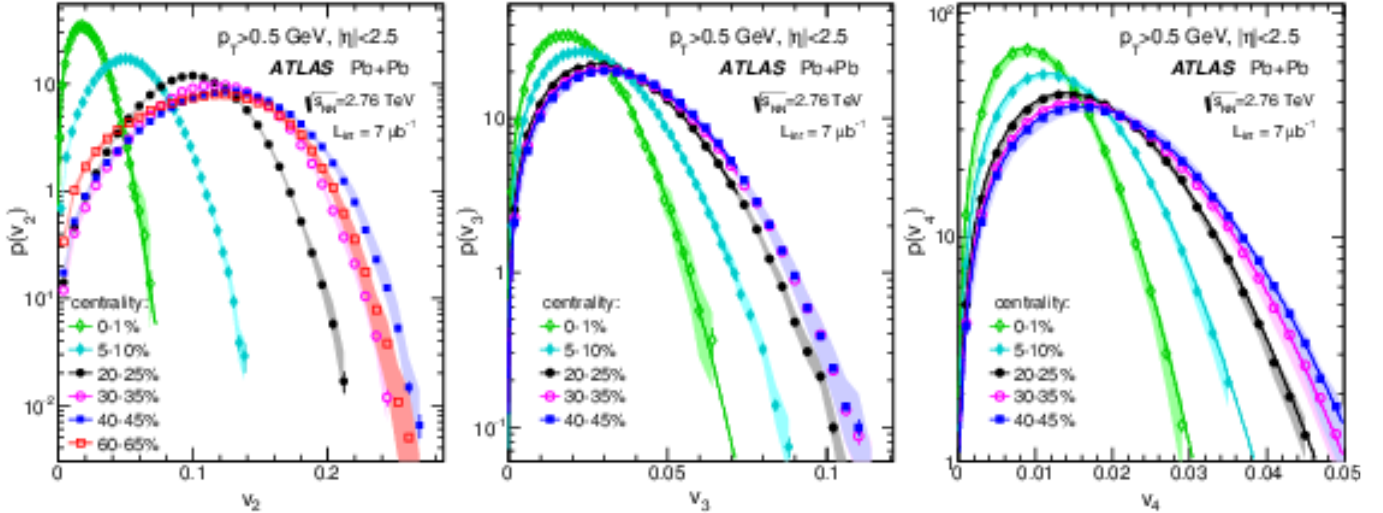


Figure 32: ATLAS data on the event-wise distributions of the harmonic coefficients $v_2 - v_4$ presented in a selection of centrality intervals, from Ref. [145].

in particular using the event-plane and 4-particle cumulant methods. Based on the analysis of Ref., the difference between these quantities is twice the variance, while their sum is twice the squared mean. Figure 33(left) shows CMS data [146] on $\sigma/\langle v_2 \rangle$ derived from cumulants, compared with the ATLAS data derived from the fully unfolded distributions. While the v_2 fluctuations compare well between the two methods, the ATLAS and CMS results on v_3 are quite different, possibly from the inapplicability of the cumulant approach for this quantity. The ATLAS results are essentially constant for all centrality intervals at around 0.5, which is the value one gets ($\sqrt{4/\pi - 1}$) if the fluctuations are described by a

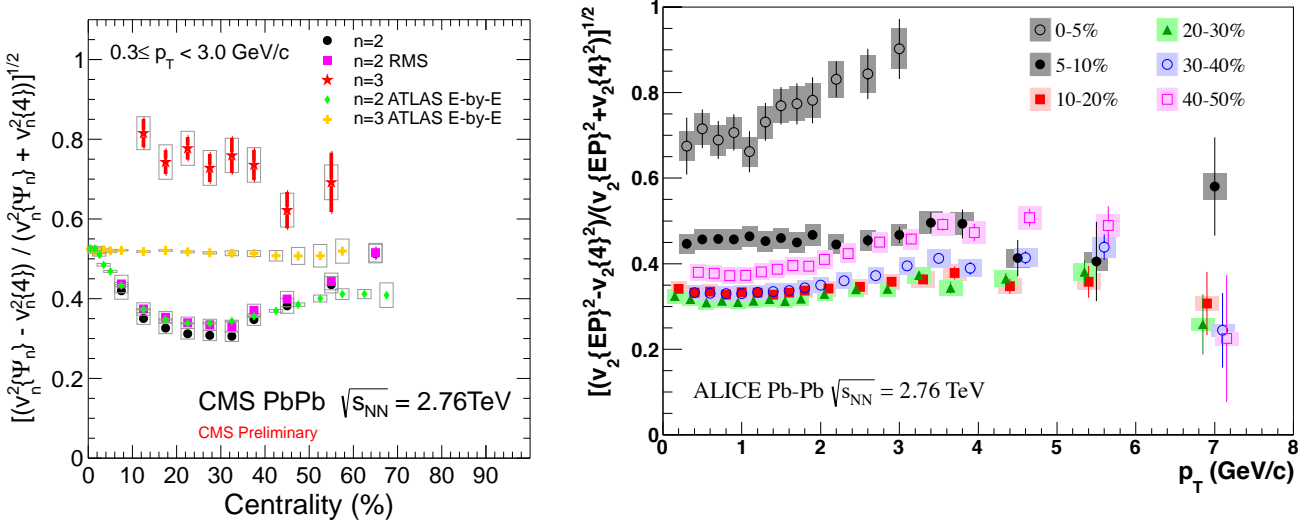


Figure 33: (left) CMS data on the centrality dependence of the standard deviation of v_2 divided by the mean, for $0.3 < p_T < 3$ GeV, extracted via the differences between the EP and cumulant results [146]. (right) ALICE data on the p_T dependence of the same quantity, out to $p_T = 8$ GeV, for a selected set of centrality intervals [140].

1147 2D Gaussian, projected along the radial direction. Figure 32(left) shows ALICE data [140] on $\sigma/\langle v_2 \rangle$
 1148 derived using a similar approach as CMS. For centrality intervals from 5-60%, the overall magnitude
 1149 is similar to that seen by the other experiments. However, this figure points out that the fluctuations
 1150 have essentially no centrality dependence out to moderately large p_T , about 8 GeV, which reaches into
 1151 the plateau region typically associated with differential energy loss.

1152 6 Electroweak probes

1153 While a primary topic in the study of heavy ion collisions is the modification of jets in the hot and dense
 1154 nuclear medium, typical analyses of hard processes have assumed that the structure of a nucleon in a
 1155 nucleus-nucleus collision is quantitatively the same as one in a nucleon-nucleon collision. From analyses
 1156 of lepton-nucleus deep inelastic scattering data, it is known that cross sections do not scale linearly with
 1157 the number of nucleons, as might be expected simply from the availability of scattering centers. The
 1158 deviations from this scaling are referred to generally as “nuclear shadowing”, and are typically shown
 1159 as a function of Bjorken x for different ranges in the hardness scale Q^2 . The region around $x \sim 0.1$
 1160 corresponds to the valence quark region for a standard nucleon, and this is usually enhanced. The
 1161 region above this, $x \geq 0.2$ is typically suppressed (the so-called “EMC effect”), while the region below
 1162 $x \ll 0.1$ is also suppressed down to very small values of x . The latter phenomenon is more typically
 1163 known as “nuclear shadowing” and is thought to arise generally from quantum mechanical effects which
 1164 deplete the numbers with small fractions of the nucleon momentum.

1165 It is important to understand the magnitude of these sorts of effects in the realistic environment of
 1166 a heavy ion collision, in order to properly interpret measurements of hard process rates relative to a
 1167 nucleon-nucleon reference system. At the RHIC collider, this was addressed early in the experimental
 1168 program through measurements of high p_T particles in deuteron-gold collisions. Presumably, any gross
 1169 effects related to modifications of nucleon structure in the nuclear environment would show up as
 1170 modifications in this system. It was found that hadrons above ~ 2 GeV were produced at expected rates
 1171 near $\eta = 0$, confirming that the high p_T suppression observed in the early days of the RHIC program

1172 did not arise from changes in nucleon structure, and strengthening the case for jet suppression in the
1173 hot and dense medium. However, it was also found that hadrons and J/ψ particles were suppressed at
1174 forward angles, in the direction of the incoming deuteron, especially in more “central” d+Au collisions,
1175 and enhanced slightly at backwards angles, in the direction of the nucleus. These features are in
1176 broad agreement with predictions from calculations incorporating the nuclear shadowing observed in
1177 lepton-nucleus DIS.

1178 While the measurement of hadronic final states in proton (or deuteron)-nucleus collisions is thought
1179 to give useful information on modifications in the initial state of these simpler systems, the above-
1180 mentioned observed modifications of jets precludes similar observables giving similar information in
1181 heavy ion collisions. For this reason, great attention has been given to the measurement of “penetrating
1182 probes”, particles which do not interact strongly after they are produced. While charged leptons and
1183 neutral photons, of course, do not interact strongly, they come predominantly from jets and hadrons
1184 at relative low $p_T < 20$ GeV. However, at high p_T , most leptons are known to arise from the decay of
1185 electroweak bosons (Z and W particles). Furthermore, isolated photons at high p_T are predominantly
1186 “prompt”, i.e. arising from the direct interactions of quarks and gluons and not from electromagnetic
1187 decays of hadrons (π^0 and η).

1188 While the production cross sections for the heavy bosons are prohibitively small at the top RHIC
1189 energies (200 GeV per nucleon-nucleon collision), the LHC provides the first heavy ion system where
1190 all of the electroweak bosons are produced at substantial rates. This section presents measurements of
1191 all three particles in Pb+Pb collisions at the LHC, and shows their comparisons either with nucleon-
1192 nucleon reference data, or cross sections calculated with perturbative QCD using standard structure
1193 functions. The main physics goals of these measurements are twofold

- 1194 • To establish whether the production of the vector bosons is proportional to the nuclear thickness
1195 or, equivalently, the number of binary nucleon-nucleon collisions
- 1196 • To see whether any modifications of vector boson production can be observed, and if they can be
1197 attributed to modifications of the nuclear PDFs

1198 Theoretical calculations provide some guidance as to the magnitude of the modifications of standard
1199 PDFs expected in nPDFs, but substantial uncertainties remain due to the different parameterizations of
1200 the existing nDIS data. One feature which is predicted generically, however, is the decreasing magnitude
1201 of nuclear modifications with increasing Q^2 . As shown in Fig., the large magnitude of shadowing
1202 expected at low Q^2 (i.e. low p_T) is reduced substantially even by $Q^2 = 100$ GeV. Thus, the large values
1203 of M_Z and M_W are already 80-90 GeV, naturally lead to nuclear modifications only at the 10-15% level.

1204 6.1 Measurements of W and Z bosons in Pb+Pb collisions

1205 The first observation of vector bosons in Pb+Pb collision was performed by the ATLAS experiment with
1206 a set of 38 Z candidates obtained in the first heavy ion run in 2010, which was followed several months
1207 later by a CMS result comparing with theoretical calculations. However, the statistical power of the
1208 2010 sample was not sufficient to make strong conclusions about the Z production rates as a function
1209 of the nuclear thickness. The situation has improved dramatically with a published measurement of
1210 W bosons by CMS, also from the 2010 dataset, but benefiting from the large increase in the W cross
1211 section compared with Z . ATLAS has also published the yield and spectrum of Z bosons from the much
1212 larger 2011 Pb+Pb dataset. Together these give a relatively complete first look at the behavior of heavy
1213 vector bosons in heavy ion collisions.

1214 The CMS W measurement was performed using the CMS inner tracker, which covers $|\eta| < 2.4$ and
1215 the CMS muon spectrometer, which covers $|\eta| < 2.4$ using a variety of gaseous detectors (CSC, DT,
1216 with RPCs used for triggering), but was restricted to $|\eta| < 2.1$ in this particular analysis. The ATLAS Z

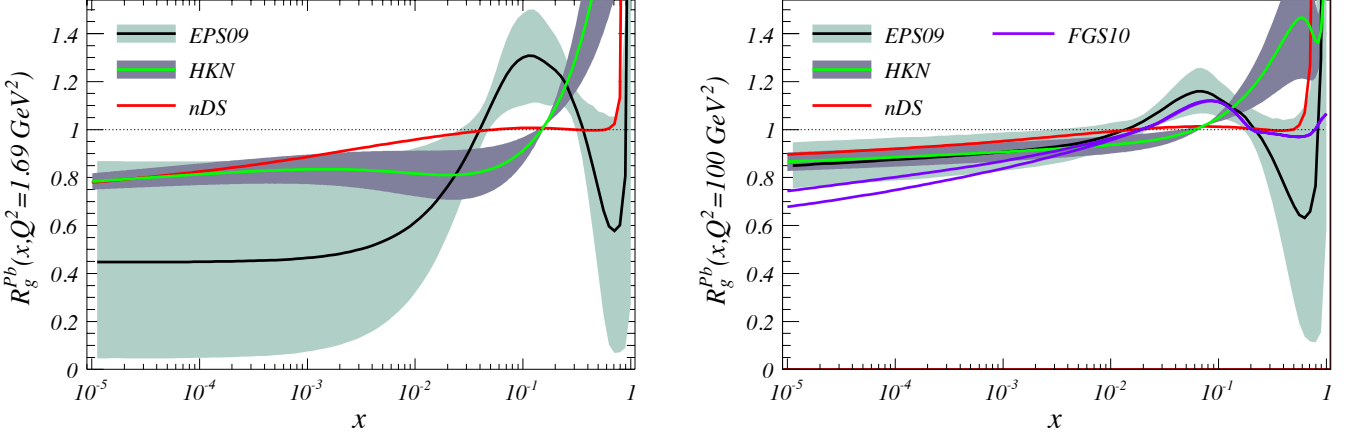


Figure 34: (left) Modifications to proton PDFs expected from different nPDF implementations, for $Q^2 = 1.69 \text{ GeV}^2$, (right) Modifications to proton PDFs expected from different nPDF implementations, for $Q^2 = 100 \text{ GeV}^2$ from Ref. [147].

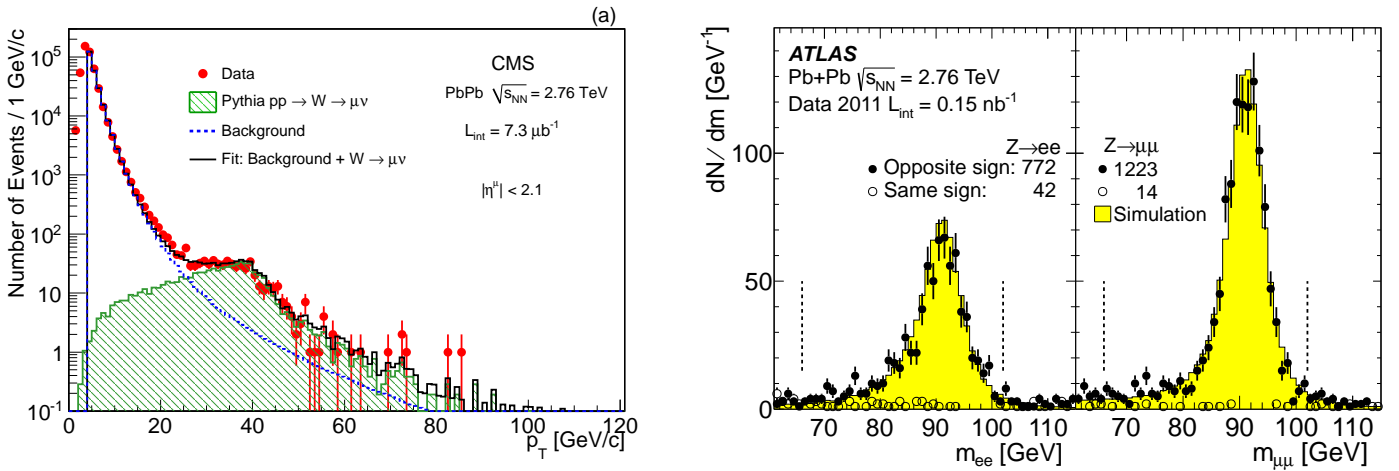


Figure 35: (left) Single muon spectrum, after selection cuts, from CMS data [148] (right) Dimuon mass spectrum, in electron and muon channels from ATLAS data [149].

measurement was performed combining dilepton decays in the muon and electron channels. The ATLAS muon spectrometer uses drift tubes and cathode strip chambers to measure muons with $|\eta| < 2.7$ in tandem with the ATLAS inner detector covering $|\eta| < 2.5$. Electrons are measured in ATLAS using the inner detector in association with the ATLAS calorimeter system, which is particularly finely segmented in η for $|\eta| < 2.5$, allowing rejection of jet backgrounds.

As shown in Figure 35(left) from CMS, the single muon spectrum at high p_T clearly shows a contribution from W bosons as a peak near 40 GeV. The backgrounds from jets are strongly reduced by calculating the missing p_T for each event with a high $p_{T\text{muon}}$, based on tracks with $p_T > 3 \text{ GeV}$. The background from Z bosons is removed by removing muons which combine with a second muon in the same event that reconstructs to a mass near the Z mass. After selections, about 540 W candidates were found in the 2010 Pb+Pb data. Figure 35(right) shows the dimuon and dielectron mass spectrum after requiring $p_T > 10 \text{ GeV}$ for the muons, and $p_T > 20 \text{ GeV}$ for the electrons. The Z lineshape is in good agreement with simulations for both dielectron and dimuon channels. After selections, about 2000 Z candidates were reconstructed in the 2011 Pb+Pb data.

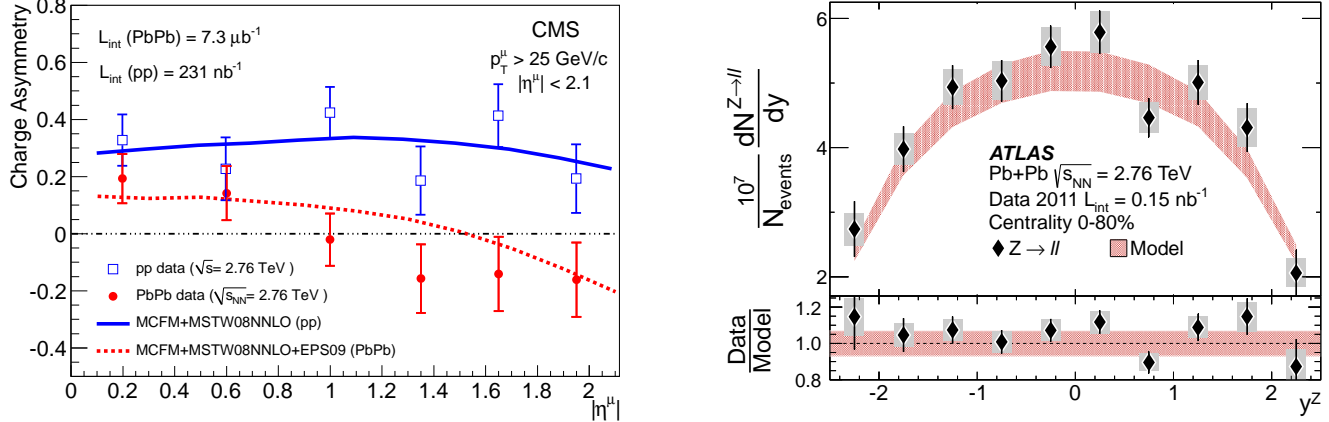


Figure 36: (left) Charge asymmetry for W candidates, from CMS data [148] (right) Rapidity dependence of dN_Z/dy compared to PYTHIA scaled to the NNLO cross section [149]

Figure 36(left) shows the pseudorapidity dependence of the charged lepton asymmetry for the muons associated with W candidates ($A_\mu = (N_{W^+} - N_{W^-})/(N_{W^+} + N_{W^-})$), both for Pb+Pb and p+p data at the same CM energy ($\sqrt{s_{NN}} = 2.76 \text{ TeV}$). The evident differences between the Pb+Pb and p+p stem primarily from the neutrons in the Pb nuclei, which modify the expected charge distribution, particularly in the forward direction where the Bjorken x probed is sensitive to the valence quarks. Both data sets are compared with NNLO calculations of the W charge asymmetry and good agreement is found for both p+p and Pb+Pb. While this suggests that no large nPDF effects are needed to accommodate the existing data, it was pointed out in Ref. [150] that the scale factors in EPS09 formalism will cancel out in the charge asymmetry ratio, making this quantity suboptimal for isolating nPDF modifications.

Figure 36(right) shows the rapidity dependence of the per-event Z boson yield in the 0-80% centrality interval in Pb+Pb collisions from the 2011 ATLAS Pb+Pb data. The data is compared to the same distribution from PYTHIA (version 6.425), scaled to the NNLO total cross section, and the appropriate mean nuclear thickness. Good agreement is found between the heavy ion data and the absolutely-scaled PYTHIA reference, the ratio between them being consistent with unity within the stated uncertainties. While small effects at the 10-15% level are not ruled out, nor are they required to make sense of the current measurements.

The centrality dependence of the separate W charge states and the total from CMS is shown in Figure 37(left), as a function of the number of participating nucleons, and for the p+p data. While p+p shows a clear difference between positive and negative W's, reflecting the charges of the initial protons, there is little difference between them in the Pb+Pb data, reflecting the additional down quarks introduced via the neutrons in the Pb nuclei. The heavy ion data shows a clear scaling with centrality, once the W yields – both for the charge-separated yields, and the total – are scaled by the number of binary collisions. A similar message is found in the ATLAS Z data, shown in Figure 37(right), which shows the Z yield, scaled by the number of binary collisions, also as a function of the number of the mean number of participating nucleons for each centrality interval. The ATLAS data also shows that the centrality dependence is the same for the dielectron and dimuon channels, and even for selected intervals in the Z p_T .

6.2 Measurement of isolated photons in Pb+Pb collisions

The measurement of photons in heavy ion collisions is also an important contribution to the study of the Pb+Pb initial state, with some advantages and disadvantages. Unlike Z and W bosons, no energy

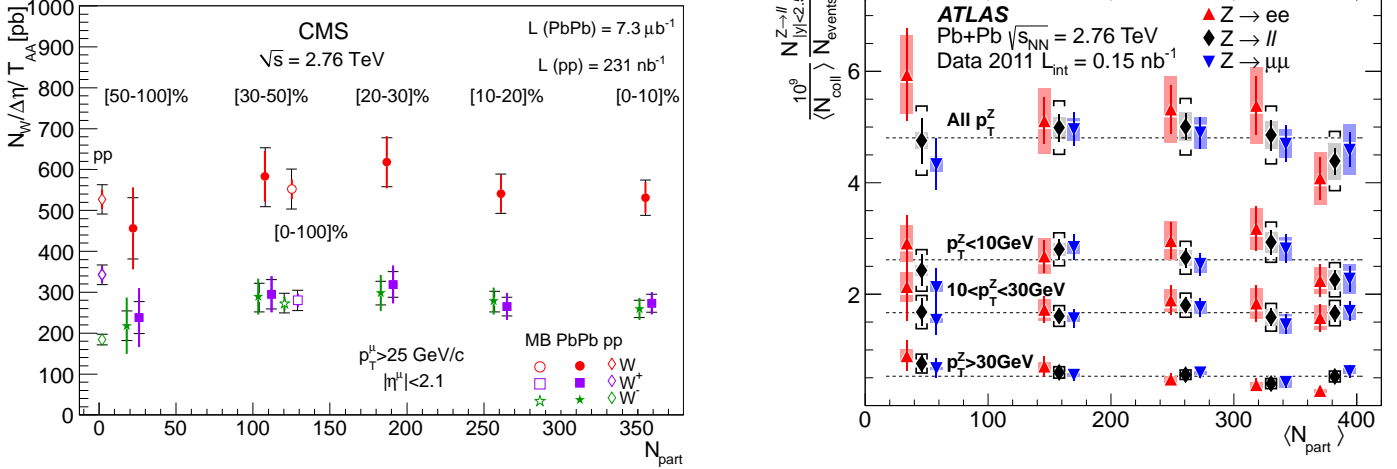


Figure 37: (left) Yield per collision for W candidates, from CMS data [148] (right) Yield per collision for Z's, in both electron and muon channels from ATLAS data. [149]

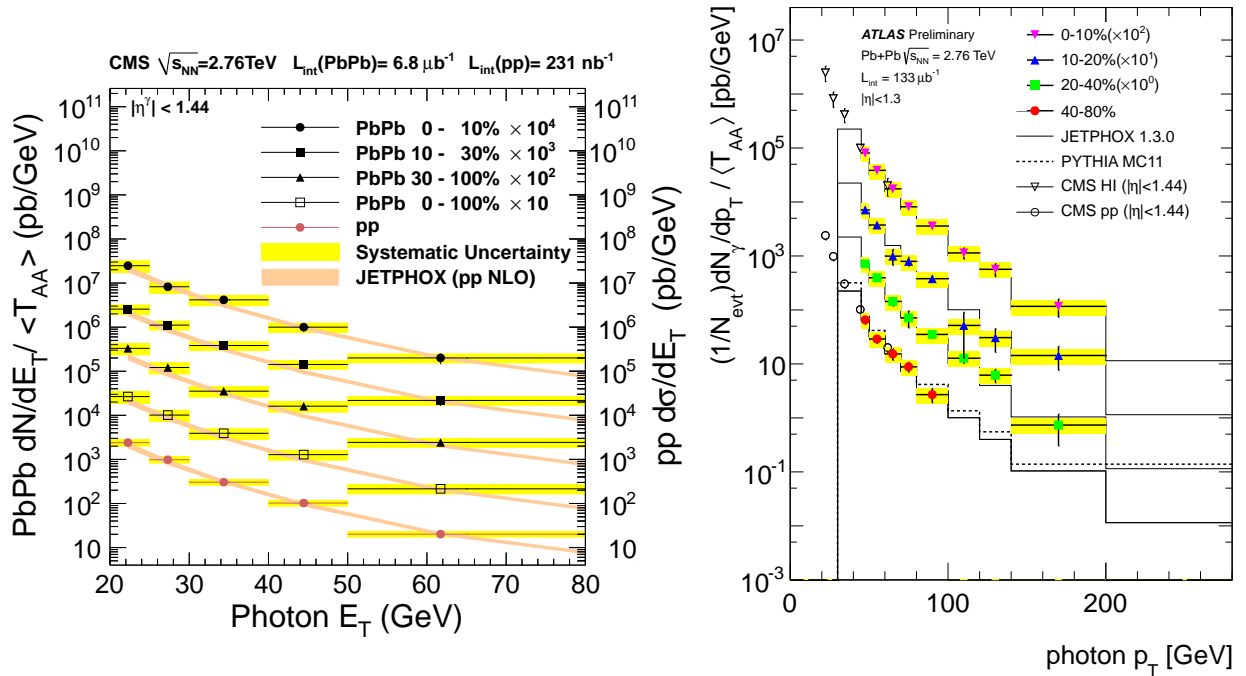


Figure 38: (left) Photon yields scaled by the mean nuclear thickness function for $|\eta| < 1.44$, from CMS data [151] (right) The similar quantity from ATLAS, for $|\eta| < 1.3$, from ATLAS data [152].

from the initial 2-to-2 scattering process is used in the boson mass, and so the cross sections at high p_T are substantially higher at the same transverse momentum. However, photon measurements do not provide a clear mass peak, and nor are they associated with a track measured in an inner tracker. This means that backgrounds are an irreducible part of the measurement, particularly at low p_T , where one expects large contribution from jet fragmentation into high momentum neutral pions or eta mesons.

At low p_T , ALICE has performed a preliminary measurement of the spectrum of direct photons using the so-called “subtraction” method [153]. In this approach, inclusive photons are measured, and

1268 the contribution from hadron decays is estimated through a combination of direct measurements and a
1269 cocktail based on m_T -scaling. Using this, the remaining contribution from direct photons is extracted
1270 and compared to perturbative QCD calculations. This has been performed on 7 TeV p+p data, and
1271 good agreement with pQCD is found. In the 0–40 % centrality interval in Pb+Pb, good agreement
1272 is found above $p_T = 4$ GeV with a scaled NLO calculation at the Pb+Pb CM energy. However, an
1273 excess is observed below 4 GeV, which is fit by an exponential and gives an inverse slope parameter of
1274 $T_{\text{LHC}} = 304 \pm 51^{\text{syst+stat}}$ MeV. By comparison to a similar measurement from PHENIX, which observes
1275 an inverse slope of $T_{\text{PHENIX}} = 221 \pm 19^{\text{stat}} \pm 19^{\text{syst}}$ MeV for the 0–20% centrality interval at the top RHIC
1276 energy [154], ALICE concludes that the initial temperature at the LHC is higher than that measured
1277 at RHIC.

1278 At high p_T , two primary techniques are used to increase the purity of the photon sample, which
1279 is typically $O(0.1\%)$ based on the expected relative yields of photons and jets. The first is to select
1280 photon candidates as electromagnetic clusters which pass a set of selection criteria, trained on photon
1281 simulations to efficiently reject electromagnetic decays while keeping most of the produced photons.
1282 These criteria involve both the “shape” of the cluster (since photon showers are typically quite narrow),
1283 as well as the presence of energy in the “hadronic” section of the experimental calorimeters (since photon
1284 showers should typically be well-contained in the front electromagnetic sections). The second technique
1285 is to require that the photon candidate is “isolated”, i.e. only a limited amount of ambient energy,
1286 including both electromagnetic and hadronic contributions, is allowed to be present near the photon.
1287 In the context of a heavy ion collision, where there is typically a substantial amount of uncorrelated
1288 energy present, techniques must be applied to estimate and remove this energy event by event. However,
1289 even after doing this, one must account for real photons with an upward fluctuation of ambient energy
1290 nearby (“leakage”) as well as fake photons with a downward fluctuation, passing the nominal selection
1291 criteria. Thus, shower-shape discriminators are typically combined with an isolation requirement, and
1292 various means exist to combine this information to estimate the true purity of a photon sample in a
1293 data-driven fashion.

1294 The CMS photon measurement is performed using electromagnetic clusters in the CMS ECAL, with
1295 the CMS tracks and HCAL used to tag backgrounds from electrons or hadronic decays. The signal from
1296 prompt isolated photons is extracted using a two-component template fit to the distribution of $\sigma_{\eta\eta}$, a
1297 variable which reflects the width of the cluster in the η direction. The signal is derived from PYTHIA
1298 γ +jet events, embedded into real Pb+Pb data events. The background distribution is derived from a set
1299 of photon candidates which are required to fail the isolation selection. After subtracting the extracted
1300 backgrounds and correcting for efficiency and resolution effects, the yield of photons is presented as a
1301 function of p_T in three centrality intervals as well as a minimum-bias (0–100%) interval. A similar analysis
1302 performed on pp data is also shown. In Figure 38(left), both the heavy ion and pp data are compared
1303 with an NLO pQCD calculation (using the JETPHOX package) by scaling the calculation by the mean
1304 nuclear thickness function $\langle T_{\text{AA}} \rangle$ relevant for each interval. It is found that the NLO calculations agree
1305 with the pp and heavy ion data in all cases, within the stated statistical and systematic uncertainties.
1306 This demonstrates that, like the Z and W results, the photon yields scale with the number of binary
1307 collisions. However, while the Z and W results focused on integrated yields, the photons show that
1308 there is also no modification of the spectral shape.

1309 ATLAS performed a similar analysis, using the “double sideband” technique to estimate the photon
1310 fraction in each p_T and centrality interval for $|\eta| < 1.3$. In Figure 38(right), the preliminary ATLAS
1311 data is shown compared with both the CMS data and JETPHOX 1.3.0 results. The ATLAS and CMS
1312 data agree well (given the 5% difference in the η range) and ATLAS data agree with JETPHOX out to
1313 $p_T = 200$ GeV.

1314 7 Jet quenching

1315 The vastly increased production cross sections for very high p_T hard-scattered jets at the LHC compared
1316 to RHIC, combined with the moderate growth of soft particle production forming the “underlying
1317 event”, opened a new era in studies of jet quenching. The improved signal to background allowed
1318 the use of standard reconstruction techniques, calibration methods, background subtraction methods
1319 and jet observables developed and well characterized for studies of p+pcollisions. Typically jets in LHC
1320 heavy-ion collisions have been reconstructed using the infrared-safe anti- k_t jet clustering algorithm [155]
1321 with the radius parameter R varying from $0.2 < R < 0.5$.

1322 Early measurements of hadron production at RHIC clearly showed a large suppression (up to a
1323 factor of five to six) in the production rates of high p_T particles in heavy-ion collisions compared to a
1324 properly scaled pp reference distribution [156, 157]. Similarly, the “jet quenching” phenomenon was
1325 observed in the suppression of back-to-back hadron production in central heavy ion collisions [156, 157].
1326 Yet nearly a decade after the first observation, a detailed understanding of the physics of parton energy
1327 loss in the hot and dense medium remained elusive. A review of the theoretical state-of-the art before
1328 LHC startup can be found in [158].

1329 Compared to hadron-based observables such as those employed at RHIC, measurements of recon-
1330 structed jet, dijet and photon-jet final states promise much greater control over the type and kinematics
1331 of the initial scattering process and access to information about the energy flow in the evolution of the
1332 collision process not otherwise accessible.

1333 7.1 Dijet correlations

1334 The first jet-based observables discussed here are derived from dijet correlations. Within hours after the
1335 first heavy-ion collisions at LHC were recorded, it became obvious that there was a large abundance of
1336 events where a high p_T reconstructed jet (e.g. $p_T \approx 100 \text{ GeV}/c$) was not accompanied by a back-to-back
1337 high p_T partner jet.

1338 In the first study of jets in PbPb collisions at LHC ATLAS used azimuthal correlations and the
1339 momentum asymmetry between the leading and subleading jets to characterize the modification of
1340 their properties relative to pp collisions [159]. The jet pairs were selected to have relative azimuthal
1341 angle $\Delta\phi = |\phi_1 - \phi_2| > \pi/2$ and their momentum asymmetry was determined as

$$A_J = \frac{E_{T1} - E_{T2}}{E_{T1} + E_{T2}}. \quad (7)$$

1342 The leading jet was required to have a transverse energy in the calorimeter of $E_{T1} > 100 \text{ GeV}$, and the
1343 subleading jet was selected to have $E_{T2} > 25 \text{ GeV}$, after correction for the calorimeter energy response.

1344 In Fig. 39 the dijet asymmetry and $\Delta\phi$ distributions for PbPb data (solid markers) are shown in four
1345 bins of collision centrality. They are compared with PYTHIA MC calculations, including a background
1346 simulation using the HIJING event generator. Also shown are data from 7 TeV p+pcollisions (open
1347 circles).

1348 A clear centrality evolution of the dijet asymmetry distribution can be seen, while the azimuthal dijet
1349 correlations remain largely unchanged. For peripheral events, the PbPb dijet asymmetry is comparable
1350 to that seen in PYTHIA and p+pcollisions. For central events however, the A_J distribution widens
1351 significantly, showing a large increase in unbalanced dijet events. A similar measured by CMS, using
1352 the full 2010 Pb+Pb data set, confirmed these observations [160]. The observed trend can be naturally
1353 understood in models of parton energy loss in the hot and dense medium, where the back-to-back
1354 partons will typically traverse different path lengths, and therefore suffer different amounts of energy
1355 loss.

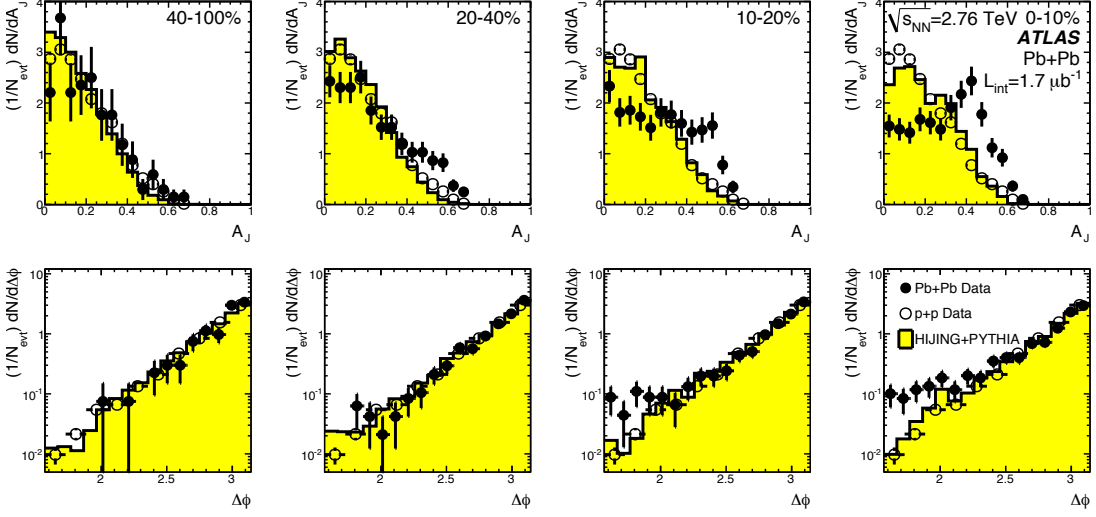


Figure 39: (top) Dijet asymmetry distributions for data (points) and HIJING+PYTHIA simulations (solid yellow histograms), as a function of collision centrality. Proton-proton data from $\sqrt{s} = 7$ TeV is shown as open circles. (bottom) Distribution of $\Delta\phi$ between the two jets, for data and HIJING+PYTHIA in four bins of centrality. Reproduced from [159].

The initial ATLAS and CMS dijet asymmetry analyses [159, 160] were extended using a large dataset of PbPb collisions collected in 2011 by the CMS collaboration at $\sqrt{s_{\text{NN}}} = 2.76$ TeV [161]. For this analysis, the events were reconstructed using the CMS “particle-flow” algorithm [162, 163], which attempts to identify all stable particles in an event (electrons, muons, photons, charged and neutral hadrons) by combining information from all sub-detector systems. Jets were then reconstructed, after background subtraction, using the anti- k_T sequential recombination algorithm, with radius parameter $R = 0.3$ [155].

To study the momentum dependence of the amount of energy loss, Fig. 40 presents the dijet asymmetry in bins of leading jet p_T , for 0–20% central events. The distributions show the $p_{T,2}/p_{T,1}$ ratio, instead of A_j , as a more intuitive way of quantifying the dijet momentum asymmetry.

One observes a strong evolution in the shape of the distribution across the various p_T bins, while a significant difference between PbPb data and PYTHIA+HYDJET simulations persists even for the highest p_T bin. The jet momentum dependence of the energy loss can be examined by measuring the dijet asymmetry as a function of leading jet momentum. This was studied by CMS, using $\langle p_{T,2}/p_{T,1} \rangle$. Figure 41 shows the p_T dependence of this ratio for three bins of collision centrality, with PYTHIA+HYDJET simulations shown as squares and PbPb data shown as points.

For all data and simulations, a rising trend of $\langle p_{T,2}/p_{T,1} \rangle$ as a function of leading jet momentum is seen. This is a result of the improving jet energy resolution with increasing jet p_T and the evolution in jet kinematics as described by the PYTHIA calculations. Importantly, the data show a significantly larger jet asymmetry in central events than in the simulations and in peripheral and p+p data. This effect persists to the highest p_T measured, showing that even the highest p_T jets in PbPb collisions ($p_T > 350$ GeV/c) suffer energy loss as they traverse the medium. A detailed understanding of the energy loss p_T dependence (e.g. fractional vs constant energy loss) will require a full jet MC calculation taking the detector response as a function of p_T into account.

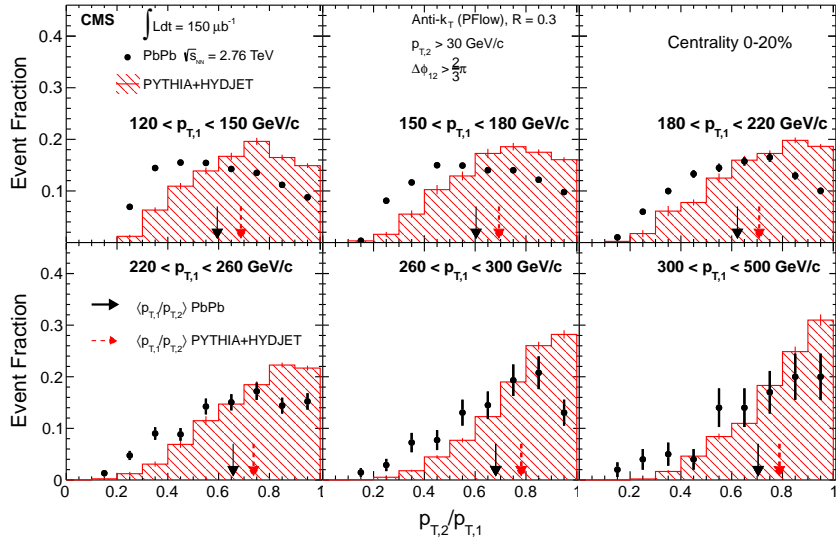


Figure 40: Dijet asymmetry ratio, A_J , in bins of leading jet transverse momentum from $120 < p_{T,1} < 150 \text{ GeV}/c$ to $p_{T,1} > 300 \text{ GeV}/c$ for subleading jets of $p_{T,2} > 30 \text{ GeV}/c$ and $\Delta\phi_{1,2} > 2\pi/3$ between leading and subleading jets. Results for 0–20% central PbPb events are shown as points, while the histogram shows the results for PYTHIA dijets embedded into HYDJET PbPb simulated events. The error bars represent the statistical uncertainties. Reproduced from [161].

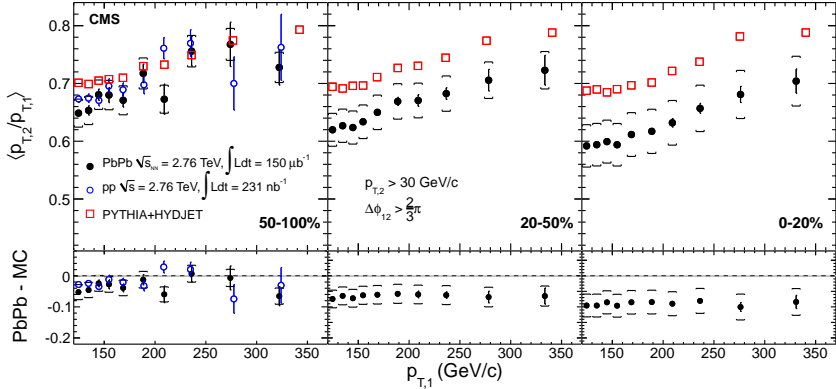


Figure 41: (Top): Dijet momentum ratio $\langle p_{T,2}/p_{T,1} \rangle$ as a function of leading jet p_T in three bins of collision centrality. PbPb data are shown as points, with brackets indicating systematic uncertainties. PYTHIA+HYDJET calculations are shown as squares. In the peripheral bin, pp data are displayed as open circles. (Bottom): Difference of $\langle p_{T,2}/p_{T,1} \rangle$ between the PbPb results and PYTHIA+HYDJET reference. Reproduced from [161].

1380 7.2 Suppression of jet yields

1381 A complementary approach to the study of parton energy loss using dijet asymmetry measurements is
 1382 offered by studies of the nuclear modification factor R_{AA} of jet yields relative to a p+p reference or the
 1383 centrality evolution of R_{CP} relative to peripheral events.

1384 Measurements of the inclusive jet production rates were performed by ATLAS [164] and ALICE. As
 1385 a result of the path length dependence of parton energy loss in the medium, a reduction in the observed
 1386 jet yield at a given p_T is expected for more central Pb+Pb collisions, compared to an N_{coll} scaled p+p
 1387 or peripheral reference.

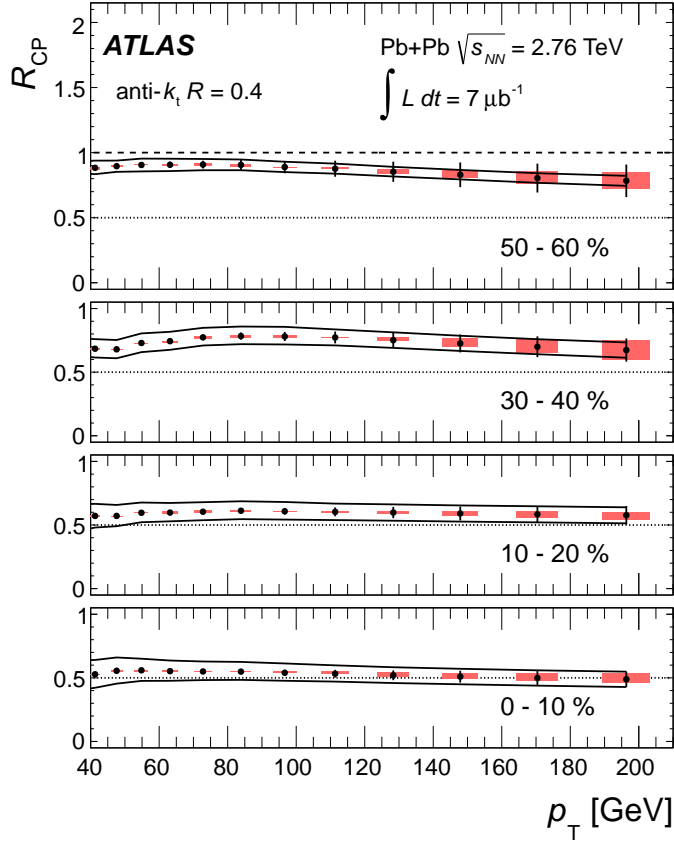


Figure 42: p_T dependence of jet R_{CP} for $R = 0.4$ jets, in four bins of collision centrality. Error bars indicate statistical errors while shaded boxes indicate partially correlated systematic uncertainties. The solid lines show fully correlated uncertainties. Reproduced from [164].

The resulting R_{CP} values are shown in Figure 42 for $R = 0.4$ jets as a function of jet p_T in four bins of collision centrality. Uncertainties are shown as statistical uncertainties, partially correlated systematic uncertainties, and fully correlated uncertainties.

For all centralities only a weak dependence of R_{CP} on jet p_T is observed. In contrast, a strong suppression of the jet yield is evident in central collisions, with R_{CP} only reaching a value of about 0.5. This is reminiscent of the value of charged hadron R_{AA} observed by CMS at very high p_T which also reaches a value of about 0.5. The centrality evolution of R_{CP} is consistent with expectations based on the increasing in-medium pathlength traversed by the partons.

Further insight into the pathlength dependence of parton energy loss may be gained by studying the dependence of the jet yield on the jets azimuthal angle relative to the event plane in peripheral Pb+Pb collisions. This allows the selection of jets traversing different length of the medium at the same medium conditions, whereas the centrality dependence of R_{CP} reflects both the changing pathlength and potential changes in the medium density with centrality.

Related measurements have been performed using the azimuthal dependence of charged hadron yields at intermediate p_T [165, 166, 167, 136, 140], and very high p_T [141]. For mid-peripheral events, a finite v_2 for charged hadrons was observed for p_T in excess of 40 GeV/c. Compared to these results, jet based measurements offer the advantage of a more direct relationship between p_T and direction of the observed jet and the initial parton.

The result of the ATLAS v_2 measurement for jets reconstructed with the anti- k_T algorithm in 2.76 TeV Pb+Pb collisions is shown in Fig. 43 as a function of jet p_T in bins of collision centrality [168].

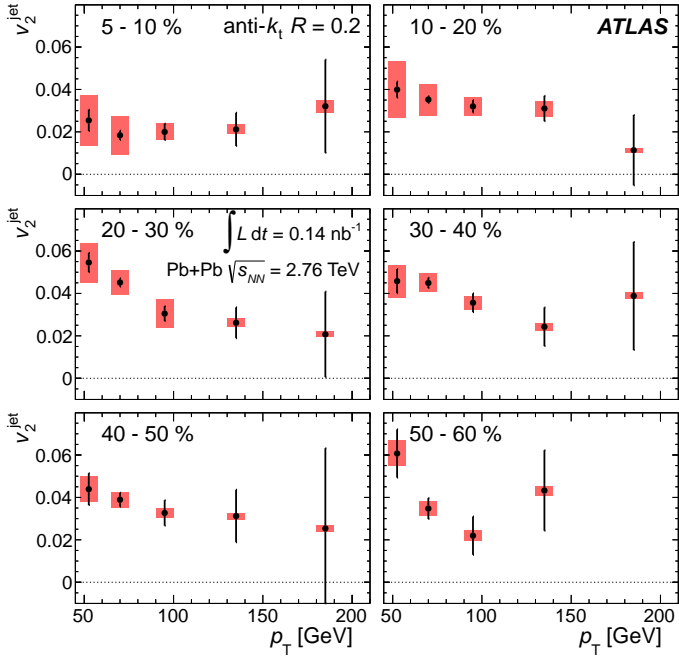


Figure 43: v_2^{jet} as a function of jet p_T in six bins of collision centrality. Error bars indicate statistical uncertainties and systematic uncertainties are shown as shaded boxes. Reproduced from [168]

1408 A finite value of v_2 is observed for all centrality and p_T , reaching up to 0.05 for mid-central collisions
 1409 and low jet p_T . The results are in good agreement with those for high p_T charged hadrons covering a
 1410 comparable range of initial parton p_T [141].

1411 7.3 Modification of jet structure

1412 In addition to the p_T and centrality dependence of the suppression, its dependence on the jet clustering
 1413 radius parameter or cone-size is also of great interest, as different energy loss mechanisms may lead to
 1414 different amounts of energy transport out of the jet cone [169, 170, 171]. This should manifest as a
 1415 cone-size dependence of the observed jet suppression.

1416 Such a dependence can be seen in Fig.44, which shows the ratio of R_{CP} values for $R = 0.3, 0.4$
 1417 and 0.5 jets compared to an $R = 0.2$ jets baseline, as a function of p_T for central events, measured by
 1418 ATLAS [164].

1419 The cancellation of various systematic uncertainties allows the observation of a significant jet
 1420 radius dependence of R_{CP} , in particular for lower jet p_T . A detailed comparison needs to consider the
 1421 p_T associated with using different radius parameters to reconstruct the same jets.

1422 Further insight into modifications of the momentum and angular structure of jets in heavy-ion
 1423 collisions can be gained by measurements of observables used for jet studies in elementary interactions,
 1424 such as fragmentation functions and jet shapes. Fragmentation functions describe the probability for a
 1425 parton to fragment into hadrons carrying certain fractions of the parton energy. In vacuum, the parton
 1426 radiation and splitting processes lead to a well-understood characteristic shape of the fragmentation
 1427 function [172].

1428 Figure 45 shows the fragmentation functions for leading and subleading jets for 0-30% central
 1429 collisions, obtained by CMS [173]. Data for Pb+Pb are shown in bins of dijet asymmetry A_J , and
 1430 compared to a p+p based reference. The lower row of plots shows the ratio of the ratios between
 1431 the PbPb and pp-based fragmentation functions. It is important to note, and has led to occasional
 1432 confusion, that these fragmentation functions are measured relative to the *observed* jet momentum, not

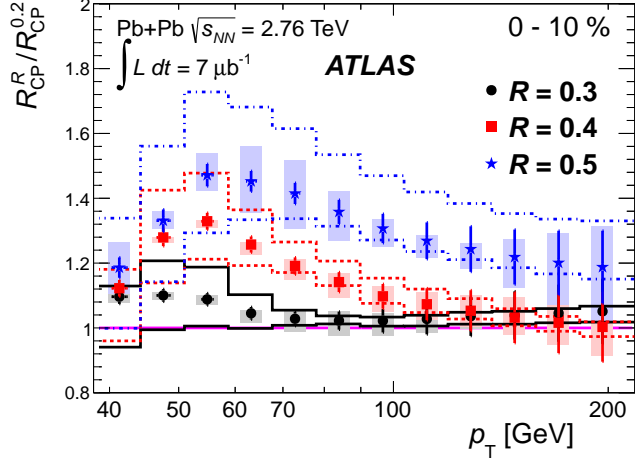


Figure 44: Ratios of R_{CP} values between $R = 0.3, 0.4$ and 0.5 jets and $R = 0.2$ jets as a function of p_T in the $0-10\%$ centrality bin. The error bars show statistical uncertainties. The shaded boxes indicate partially correlated systematic errors. The lines indicate systematic errors that are fully correlated between different p_T bins. Reproduced from [164].

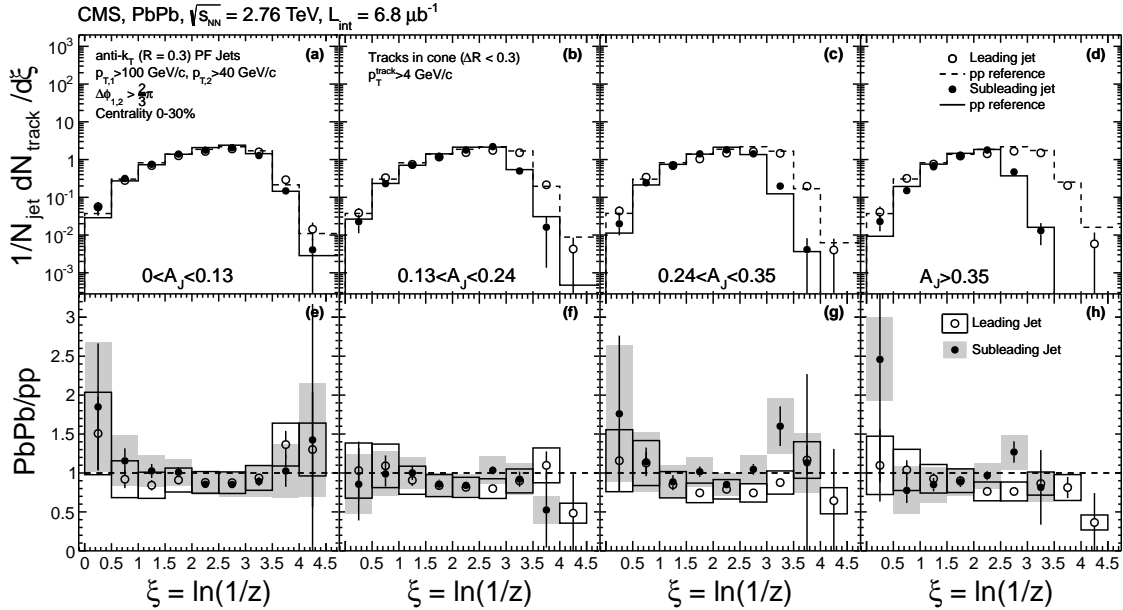


Figure 45: (a–d) Fragmentation functions for the leading (open circles) and subleading (solid points) jets in four regions of A_J in central PbPb collisions compared to the pp reference. (e–h) Ratio of each fragmentation function to its pp-based reference. Error bars shown are statistical. The systematic uncertainty is represented by hollow boxes (leading jet) or gray boxes (subleading jet). (i–l) Jet p_T distributions in PbPb collisions in four regions of A_J compared to a pp-based reference. Only statistical uncertainties are shown. Reproduced from [173].

with respect to the initial parton momentum, which can not be directly observed for dijet events in hadronic collisions.

Within the uncertainties of this first measurement, no significant modification of the fragmentation functions in Pb+Pb collisions is observed. This is true even for dijets with large asymmetry, i.e. where

the subleading jet has suffered significant energy loss. It is important to note however that only hadron fragments with $p_T > 4 \text{ GeV}/c$ have been considered in this measurement.

Complementary information about the angular structure of the jets and its modification by the in-medium shower evolution can be obtained by measuring jet shapes, i.e. the jet transverse momentum profile as a function of radial distance to the jet axis [174, 175, 176, 177, 178, 179, 180]. The differential jet shape, $\rho(r)$, is defined as

$$\rho(r) = \frac{1}{\delta r} \frac{1}{N_{\text{jet}} \text{ jets}} \sum_{r-\delta r/2}^{r+\delta r/2} \frac{\sum p_T^{\text{track}}}{p_T^{\text{jet}}} \quad (8)$$

Here r is the radial distance from the jet axis and the transverse momenta of the reconstructed track and jet are p_T^{jet} and p_T^{track} , respectively.

In the CMS measurement of jet shapes[181], the jet cone is divided into six concentric rings with radial width $\delta r = 0.05$. The transverse momentum profile is determined using the p_T sum for charged particles with $p_T > 1 \text{ GeV}/c$ in each ring, compared to the fraction of the total jet p_T carried by these particles. As for the fragmentation functions, the Pb+Pb jet shapes are compared to a p+p based reference.

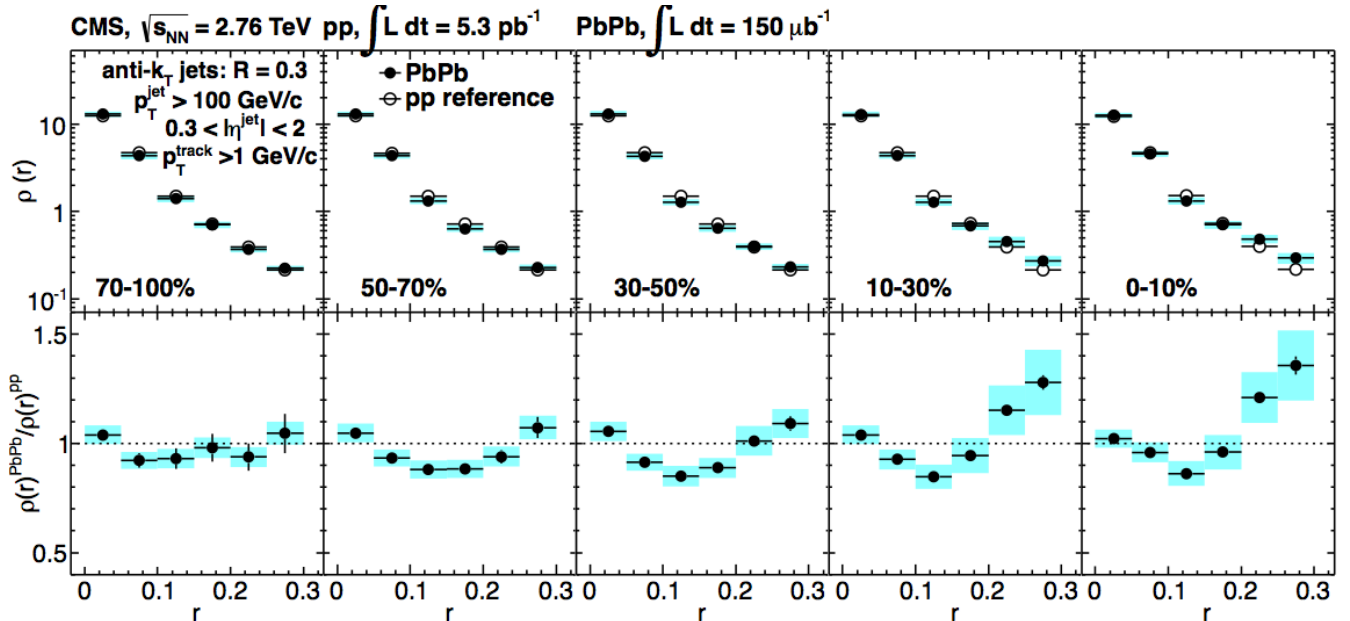


Figure 46: (Top): Differential jet shapes in Pb+Pb collisions (filled circles) as a function of distance from the jet axis for inclusive jets with $p_T^{\text{jet}} > 100 \text{ GeV}/c$ in five bins of centrality. The p+p-based reference is shown with open symbols. The shaded regions represent the Pb+Pb systematic uncertainties. Statistical uncertainties are smaller than the marker size. (Bottom): Jet shape ratios $\rho(r)^{\text{Pb+Pb}} / \rho(r)^{\text{pp}}$. Error bars show the statistical uncertainties and shaded boxes indicate the systematic uncertainties. Reproduced from [181]

The top row of Fig. 46 shows the differential jet shapes measured in Pb+Pb collisions and the p+p based reference, while the bottom row shows the ratio of the Pb+Pb and p+p distributions. The results are presented in five bins of collision centrality, from most peripheral 70–100% (left) to most central 0–10% (right). For both systems, only a small amount of the total jet energy is carried by particles more than $r > 0.2$ away from the jet axis. However, for central Pb+Pb collisions a large enhancement of the energy fraction at the largest distance to the jet axis ($r = 0.25\text{--}0.3$) can be seen. This is qualitatively

consistent with the R_{CP} ratios for different jet radii seen by ATLAS, where also an additional part of the jet energy is captured when moving beyond $R = 0.2$. This observation is in line with the trends predicted in [169, 182], although these calculations were done for a different energy and at parton level rather than hadron level.

7.4 Energy flow in dijet events

The jet measurements discussed so far clearly demonstrate that partons traversing the hot and dense medium suffer significant path-length dependent energy loss. A fraction of the “lost” energy can be recovered at radii of $r = 0.2\text{--}0.5$ from the jet axis, although even for the largest radius parameters used at LHC, a large suppression of inclusive jets and large dijet asymmetries are observed.

This naturally begs the question of the detailed energy flow in the events containing asymmetric dijets events, i.e. what is the angular and momentum distribution of the particles carrying the complementary momentum balance to the asymmetric dijet system? *A priori* the energy balance could possibly be found at low (thermal) momenta and very large radial distance to the jet axis. Therefore traditional jet-track correlation techniques relying on background subtraction are ill suited to answer this question, as even the largest dijet energy differences of several 10’s of GeV are much smaller than fluctuations in the transverse energy carried by the underlying event.

Information about the overall momentum balance in the dijet events can be obtained by exploiting conservation of transverse momentum. CMS studied the transverse momentum balance in these events using the projection of missing p_{T} of reconstructed charged tracks onto the leading jet axis [160]. Event-by-event, this was calculated as

$$\langle p_{\text{T}}^{\parallel} \rangle = \sum_i -p_{\text{T}}^i \cos(\phi_i - \phi_{\text{Leading Jet}}), \quad (9)$$

summing all tracks with $p_{\text{T}} > 0.5$ GeV/c and $|\eta| < 2.4$. Leading and subleading jets were required to have $|\eta| < 1.6$. Instead of a background subtraction, this method relies on the cancellation of the underlying event fluctuations when averaging over many events to obtain $\langle p_{\text{T}}^{\parallel} \rangle$. This method requires a tight $\Delta\phi_{1,2} > 5\pi/6$ selection for the dijet, as the underlying event is not ϕ -symmetric on an event-by-event basis.

Figure 47 shows $\langle p_{\text{T}}^{\parallel} \rangle$ as a function of A_J for two angular regions relative to the leading and sub-leading jet axes, “in-cone” ($\Delta R < 0.8$) and “out-of-cone” ($(\Delta R > 0.8)$). The top row shows results for PYTHIA+HYDJET simulations and the bottom row shows Pb+Pb data. Integrating over all particle momentum ranges (solid points), the overall momentum balance of the events is recovered within uncertainties as the negative $\langle p_{\text{T}}^{\parallel} \rangle$ in the in-cone region is balanced by a positive value in the out-of-cone angular range.

Focussing on asymmetric dijet events ($A_J > 0.33$), both data and MC exhibit an in-cone imbalance of $\langle p_{\text{T}}^{\parallel} \rangle \approx -20$ GeV/c. This is balanced by an out-of-cone contribution of $\langle p_{\text{T}}^{\parallel} \rangle \approx 20$ GeV/c. The key observation is that in the Pb+Pb data the out-of-cone contribution is found in the $0.5 < p_{\text{T}} < 4$ GeV/c region, while in MC more than 50% of the balance is carried at high $p_{\text{T}} > 4$ GeV/c. The MC results can be interpreted as resulting from initial or final-state radiation (e.g. three-jet events). For Pb+Pb events with large A_J a large part of the momentum balance is carried by soft particles ($p_{\text{T}} < 2$ GeV/c) at large angles to the jet axes ($\Delta R > 0.8$). This measurement therefore has provided crucial information about the fundamental properties of the energy loss process in the medium.

7.5 Photon-jet correlations

The use of the dijet and inclusive jet observables discussed in the previous sections to extract information about the absolute energy loss of the partons traversing the medium suffers from uncertainties about

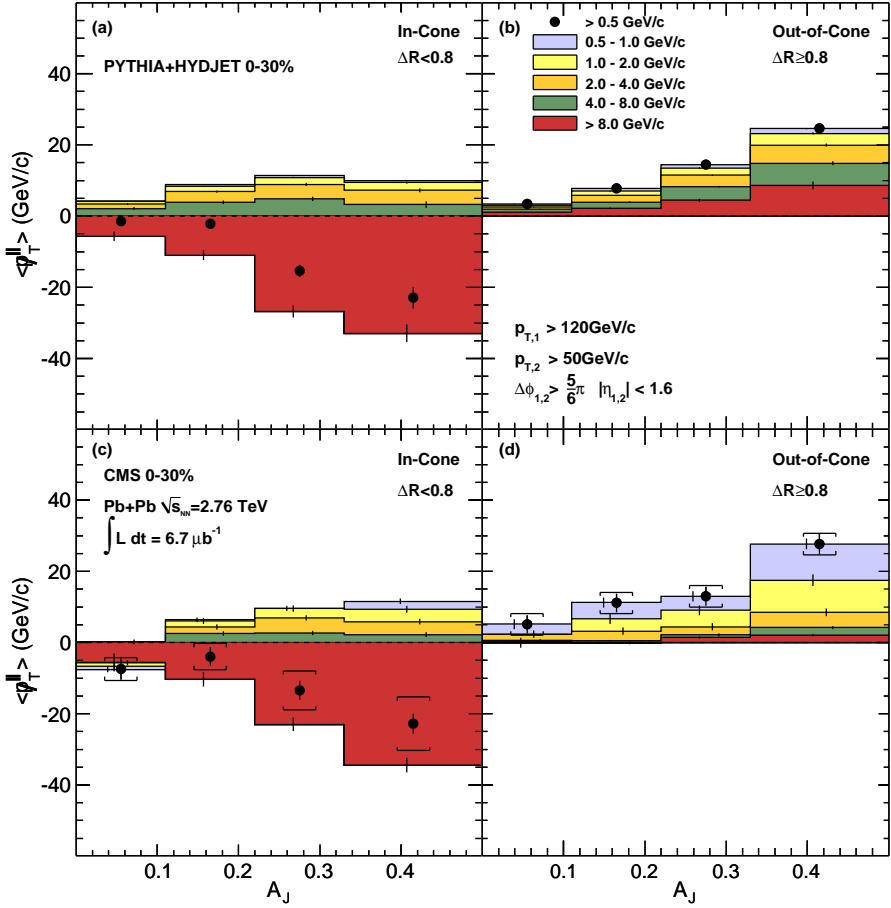


Figure 47: Average missing transverse momentum, $\langle p_T^\parallel \rangle$, for tracks with $p_T > 0.5$ GeV/c, projected onto the leading jet axis (solid circles). The $\langle p_T^\parallel \rangle$ values are shown as a function of dijet asymmetry A_J for 0–30% centrality, inside ($\Delta R < 0.8$) one of the leading or subleading jet cones (left) and outside ($\Delta R > 0.8$) the leading and subleading jet cones (right). For the solid circles, vertical bars and brackets represent the statistical and systematic uncertainties, respectively. For the individual p_T ranges, the statistical uncertainties are shown as vertical bars. Reproduced from [160].

1498 the initial parton kinematics. E.g. for the dijet asymmetry measurements in general both partons will
 1499 suffer some amount of path-length dependent energy loss, leading to ambiguities in the quantitative
 1500 interpretation of the results due to possible surface-biases.

1501 These ambiguities can be largely overcome in studies of photon-jet events, where the photon closely
 1502 determines both the initial direction and momentum of the back-to-back associated parton on an event-
 1503 by-event basis. Events where the photon and parton initial kinematics are most closely correlated
 1504 can be selected experimentally using an isolation requirement, which increases the fraction of events
 1505 with “leading order” prompt photons in the photon-jet sample. The first measurement of isolated
 1506 photon-jet correlations was performed by CMS for a $150\mu\text{b}^{-1}$ Pb+Pb dataset [183]. To select “isolated
 1507 photons”, the energy in a cone around the photon candidate was required to be less than a threshold
 1508 parameter [184], following a standard procedure developed for the analysis of p+p collisions. In the
 1509 Pb+Pb environment, the isolation cut is applied after a subtraction of an event-by-event estimate of
 1510 the underlying event contribution.

1511 Following the approach for the study of dijet correlations, the photon-jet pairs are characterized in

1512 terms of their azimuthal correlation, $\Delta\phi_{J\gamma} = |\phi^{\text{jet}} - \phi^\gamma|$, and momentum ratio, $x_{J\gamma} = p_T^{\text{jet}}/p_T^\gamma$. In addition,
 1513 the fraction of photons without back-to-back jet partner, $R_{J\gamma}$, is studied, to provide information
 1514 about events where the jet lost sufficient energy to fall below the detection threshold. For the CMS
 1515 photon-jet analysis, photons were required to have $p_T^\gamma > 60 \text{ GeV}/c$ and $|\eta^\gamma| < 1.44$. The associated jets
 1516 were selected with $p_T^{\text{jet}} > 30 \text{ GeV}/c$ and $|\eta^{\text{Jet}}| < 1.6$. To study the correlations of photons with their
 1517 associated jets (rather than photon-inclusive jet or photon-leading jet correlations), contributions from
 1518 coincidental photon-jet pairs were removed using a mixed event technique. In addition, the contribution
 1519 of background photons from e.g. hadron decays were corrected using a data driven technique. The
 1520 purity of the isolated photon-jet sample was further enhanced by requiring $\Delta\phi_{J\gamma} > \frac{7}{8}\pi$. Similar to the
 1521 dijet correlations, no angular broadening beyond the pp data and MC reference was seen in the Pb+Pb
 1522 data.

1523 The photon-jet momentum correlations in Pb+Pb data were compared to a PYTHIA+HYDJET reference
 1524 calculation as a function of collision centrality. The resulting $x_{J\gamma}$ distributions are shown in Fig. 48.
 1525 Also shown is $\langle x_{J\gamma} \rangle$ distribution for 2.76 TeV pp data, showing consistency with the PYTHIA+HYDJET
 1526 calculation within the large statistical uncertainties. The separate open and shaded red systematic
 1527 uncertainty boxes illustrate the anti-correlation of uncertainties across bins for the unity-normalized
 1528 distributions.

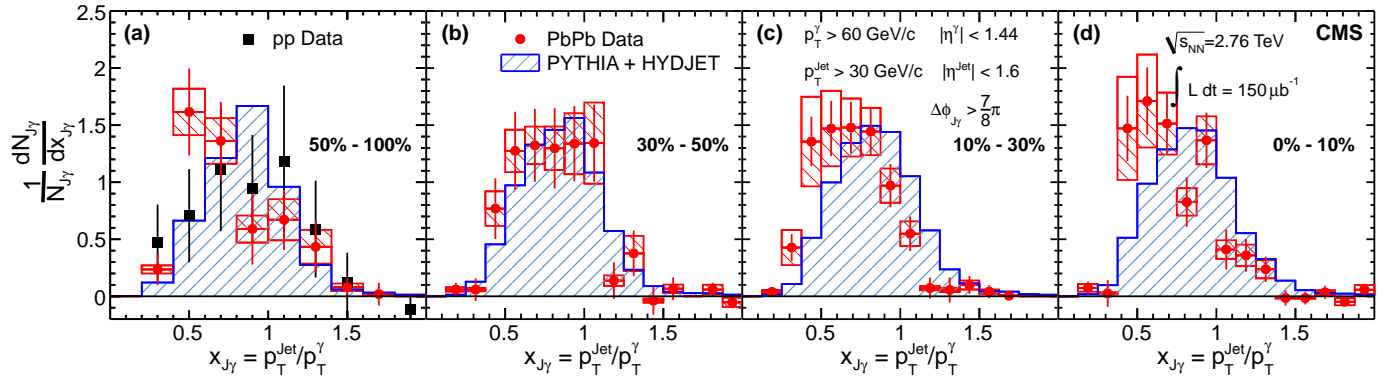


Figure 48: Distribution of the photon/jet momentum ratio, $x_{J\gamma}$, in four bins of collision centrality. The distributions are normalised to unit area. All panels compare Pb+Pb data (filled circles) to p+p data at 2.76 TeV (filled squares), and to the PYTHIA+HYDJET MC simulations (shaded histogram). Error bars show the statistical uncertainties and boxes show the (anti-correlated) systematic uncertainties. Reproduced from [183].

1529 For the most central events, the photon-jet momentum balance was found to be $\langle x_{J\gamma} \rangle_{0-10\%} =$
 1530 $0.73 \pm 0.02(\text{stat.}) \pm 0.04(\text{syst.})$, compared to a value of 0.86 predicted by PYTHIA+HYDJET at the same
 1531 centrality. This shift does not include photon-jet events where the jet fell below the 30 GeV/c analysis
 1532 threshold. The $x_{J\gamma}$ observations are therefore complemented by studies of the fraction of photons with
 1533 a jet partner, $R_{J\gamma}$. The value of $R_{J\gamma} = 0.685 \pm 0.008(\text{stat.}) - 0.698 \pm 0.006(\text{stat.})$ for
 1534 PYTHIA+HYDJET to $R_{J\gamma} = 0.49 \pm 0.03(\text{stat.}) \pm 0.02(\text{syst.}) - 0.54 \pm 0.05(\text{stat.}) \pm 0.02(\text{syst.})$ for central
 1535 Pb+Pb collisions. Combining these observations, the photon-jet studies provide clear evidence of parton
 1536 energy loss in the medium in events that are largely free of surface and reconstruction biases for the
 1537 jets. Future measurements vs high statistics p+p reference data and with increased Pb+Pb statistics
 1538 will therefore allow a quantitative determination of the absolute parton energy loss in the medium as a
 1539 function of parton p_T .

1540 8 Heavy-flavour production

1541 Measurement of charm and beauty production plays a special role in heavy-ion physics: it provides
1542 a calibrated probe, as the input p_T spectra are calculable from perturbative QCD and measurable in
1543 pp collisions. In addition, this probe is conserved from its production at early stage of the collision
1544 until it escapes from interaction region, and is eventually detected. This enables a direct access to its
1545 interactions in the QGP, including the low- and intermediate- p_T regime. Two observables are studied:

- 1546 • transverse momentum dependence of the nuclear modification factor R_{AA} for charm and beauty
1547 particles;
- 1548 • azimuthal-flow anisotropy of charm and beauty particles, measured as the elliptic-flow coefficient
1549 v_2 .

1550 These two topics are closely connected: the in-medium heavy-quark energy loss lowers the momenta of
1551 heavy quarks, they may then thermalize in the system, and thus participate in the collective-flow dy-
1552 namics. The simultaneous measurement of the two quantities opens the possibility of the determination
1553 of the heavy-flavour transport coefficients.

1554 Two methods are exploited to detect heavy-flavour particles. Reconstruction of invariant mass of
1555 exclusive particle decays in a secondary vertex, displaced from the interaction one, is the primary tool. A
1556 second method uses the lepton (μ^\pm or e^\pm) p_T spectra to infer the heavy-flavour spectra, presuming that
1557 the leptons are produced in semi-leptonic decays of heavy-flavour particles. This way, however, a (p_T -
1558 dependent) mixture of charm and beauty is measured. Sometimes a requirement that the lepton is not
1559 coming from the interaction vertex is used, which helps to eliminate the background, especially at lower
1560 p_T (below 4 GeV). The B-meson production is also accessible with the inclusive decay $B \rightarrow J/\psi + X$,
1561 using J/ψ decays separated from the interaction point.

1562 8.1 Heavy-flavour particle spectra

1563 The p_T spectra of heavy-flavour particles are measured at the LHC in pp and Pb–Pb (and p–Pb)
1564 collisions. The pp results are compared to perturbative QCD calculations and other models, giving
1565 information about preferred values for parameters, such as renormalization and factorization scales.
1566 The charm-particle spectra are measured down to very low p_T (down to 1 GeV in pp) allowing for
1567 precise determination of the total charm cross section at LHC energies. The pp spectra also serve as a
1568 normalization for Pb–Pb measurements.

1569 In general, the heavy-flavour spectra in heavy-ion collisions are expected to be also suppressed with
1570 respect to those in pp interactions, due to the energy quenching of heavy quark when traversing the
1571 dense medium. However, the energy loss of heavy quarks is predicted to be different than that of light
1572 quarks. For the energy loss by bremsstrahlung radiation, the quark energy loss will be mass dependent.
1573 The radiation is suppressed in directions close to that of the quark, for angles below $\Theta_0 \approx m/E = 1/\gamma$,
1574 due to a destructive interference (m , E , and γ being the quark mass, energy, and gamma-factor,
1575 respectively). The heavier the quark, the larger the exclusion region (i.e. Θ_0 , at a given momentum),
1576 resulting in smaller energy loss for heavy quarks compared to the light ones. This is the so called dead-
1577 cone effect introduced for the vacuum radiation [1] and later applied to the medium-induced radiation
1578 in a similar way [2]. The predicted mass hierarchy is pronounced at p_T comparable with quark masses,
1579 and goes progressively away at very high p_T . Recent model calculations include both the radiation and
1580 collisional energy loss, which results in larger suppression of heavy quarks, and gets values closer to the
1581 expectation for light ones.

1582 There are other effects that modify the expected suppression pattern. At the LHC energies, the
1583 light-flavour particles at $p_T \sim \mathcal{O}(10)$ GeV are mostly produced in gluon fragmentation, contrary to

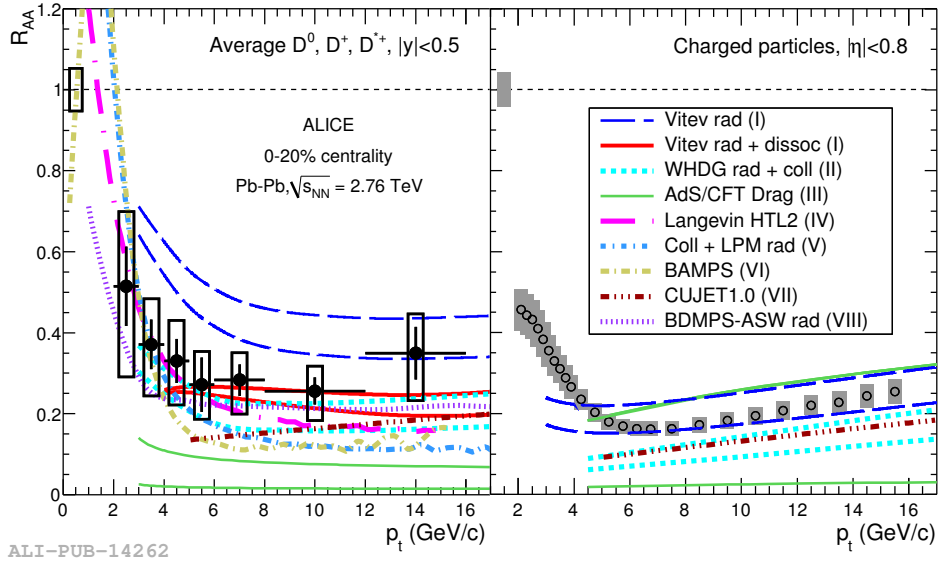


Figure 49: Average D-meson R_{AA} (left) and charged particle R_{AA} (right) as a function of p_T for the centrality between 0–20 %. The normalization uncertainties shown at unity in abscissa are almost fully correlated. The curves represent various model calculations, referred in the text, in some cases depicted as a range. Reproduced from [1].

heavy-flavour ones produced by fragmentation of the corresponding heavy quarks. Gluons have larger colour charge than quarks by a factor 9/4, consequently a gluon has to suffer more energy loss than a quark. This colour-charge effect is reinforcing the expected difference in suppression between the light- and heavy-flavour particles. Further effects of less importance, taken into account in various models, are nuclear modification of structure functions and harder fragmentation function of heavy quarks compared to the light sector.

Charm mesons are identified in the following decay modes: $D^0 \rightarrow K^- \pi^+$, $D^+ \rightarrow K^- \pi^+ \pi^+$, and $D^{*+} \rightarrow D^0 \pi^+$ (and their antiparticles), requiring the decay vertex to be displaced from the interaction point. The yields of D mesons are corrected for the feed-down from beauty decays, obtained with model simulations. This contamination amounts to 5–15 % of the yields, depending on p_T and the particle type. The p_T spectra are measured both in pp [1] and Pb–Pb [1] collisions, and used to construct the nuclear modification factor R_{AA} . The p_T dependencies of R_{AA} for three studied D-mesons are, as expected, compatible. Therefore, the results are combined into an average D-meson R_{AA} according to their statistics, dominated by the D^0 . Figure 49 compares the average D-meson R_{AA} as a function of p_T in central Pb–Pb collisions, with that of charged particles. The D-meson R_{AA} is perhaps a little bit above the charged-particle one, hinting at less suppression for charm quark, but the difference, if any, is very small. This tendency was recently confirmed with higher statistics charm measurements. The model calculations overlayed on data in Fig. 49 are (I) [185, 171], (II) [186], (III) [187], (IV) [188, 189], (V) [190, 191], (VI) [192], (VII) [193], and (VIII) [38]. The various models show varying degrees of agreement with the charm results, and in general the inclusion of collisional energy loss improves the description. In model (I) the agreement is obtained by introducing in-medium dissociation of D mesons, in addition to radiative energy loss. The remaining models, which compute also the charge-particle R_{AA} , have not reached good description for both cases, albeit some being not far.

Recently the family of measured D mesons was enlarged with the study of $D_s^+ \rightarrow K^+ K^- \pi^+$ decay. As a consequence of strangeness enhancement in heavy-ion collisions discussed in Sec. 3.3, the presence of strange quark may lead to a relative increase of D_s production with respect to other D-mesons. Reported preliminary results show the D_s R_{AA} in p_T region 4–12 GeV above the D-meson R_{AA} , however, still

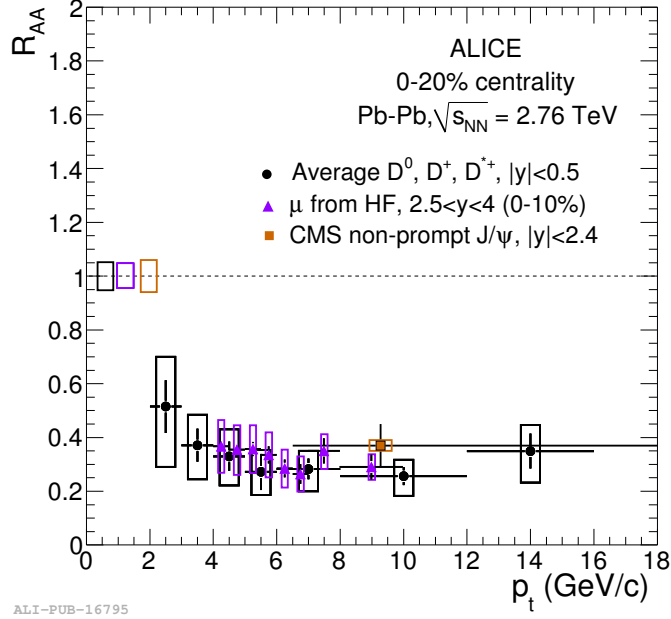


Figure 50: Heavy-flavour muon R_{AA} as a function of p_T compared to the average D-meson R_{AA} . Results are for 0–20 % centrality class of Pb–Pb collisions. CMS preliminary result for beauty R_{AA} from measurement of non-prompt J/ψ is shown with square. Reproduced from [1].

1611 within large uncertainties.

1612 The behaviour of the charm-meson R_{AA} was confirmed by the measurement of the muon spectrum
 1613 in the forward region $2.5 < y < 4$. The contribution from pion and kaon decays is subtracted from
 1614 the measured muon spectrum, and the results are presented for $p_T > 4$ GeV, where this background
 1615 contribution falls below 10 %. The obtained muon p_T spectrum thus represents a mixture of muons
 1616 from semi-leptonic charm and beauty decays, presumably still dominated by charm at the lowest p_T
 1617 and progressively becoming beauty dominated for $p_T > 6$ GeV. An analogous analysis of pp data is
 1618 used for normalization, and the resulting heavy-flavour muon R_{AA} is presented in Fig. 50. The muon
 1619 p_T , being correlated with the heavy-flavour-particle p_T , is systematically smaller than the latter one
 1620 (for p_T above a few GeV). Still, the comparison with the D-meson R_{AA} shows qualitative agreement,
 1621 since the p_T dependence is rather flat. A similar measurement using electrons in mid-rapidity region
 1622 was also reported [194].

1623 In Fig. 50 the preliminary CMS result for R_{AA} from the measurement of non-prompt J/ψ is
 1624 shown [195]. The non-prompt J/ψ particles are selected with careful analysis of the position of the
 1625 J/ψ -decay point with respect to interaction vertex. These J/ψ 's are practically exclusively coming from
 1626 B-meson decays. Recently reported detailed higher-statistics results on the centrality dependence of
 1627 the R_{AA} for non-prompt J/ψ [196] (in p_T range 6.5–30 GeV) in comparison with the ALICE D-meson
 1628 data (in p_T range 8–16 GeV) demonstrate clearly the larger R_{AA} for the beauty production than for
 1629 the charm production, except for peripheral collisions, where the measurements are within their un-
 1630 certainties. The shift between the p_T ranges takes into account that the J/ψ momentum is lowered in
 1631 the decay. This is for the first time that, as expected, the energy loss for beauty smaller than that for
 1632 charm is experimentally observed.

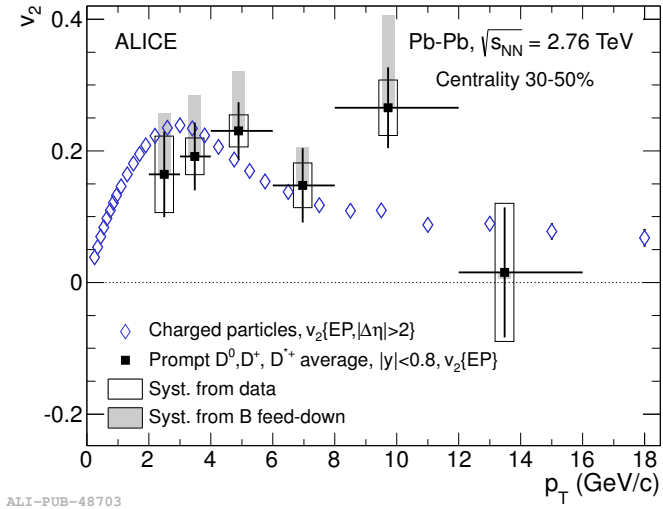


Figure 51: Elliptic-flow coefficient v_2 obtained with the event-plane method, as a function of p_T for the centrality 30–50 %, averaged for D^0 , D^+ , and D^{*+} , compared to the charged-particle measurement. Reproduced from [1].

1633 8.2 Heavy-flavour elliptic flow

1634 The primary cause of the elliptic azimuthal asymmetry is the asymmetric collision geometry: in semi-
 1635 central collisions the overlapping region of the two nuclei has an almond shape, elongated in the direction
 1636 perpendicular to the event plane (the plane defined by the beam axis and the centres of the colliding
 1637 nuclei). The elliptic flow of charm was studied by the ALICE collaboration for D mesons using the
 1638 event-plane method. To estimate the azimuthal position of the event plane, charged tracks detected
 1639 in the TPC are exploited. Then the yields of different D mesons are measured in the four azimuthal
 1640 quadrants defined with respect to the event plane. From the yields in the two in-plane and in two
 1641 out-of-plane quadrants the elliptic-flow coefficient v_2 is calculated. This is done independently for the
 1642 three mesons: D^0 , D^+ , and D^{*+} , and, as the v_2 values are compatible, they are then averaged applying
 1643 beforehand the feed-down correction like in the case of the D -meson R_{AA} . The v_2 results for the average
 1644 D meson are presented in Fig. 51 for the centrality in the range 30–50 %. The comparison with the
 1645 charged-particle v_2 obtained with the same method reveals a similar behaviour: the v_2 values for p_T
 1646 between 2–8 GeV are compatible. This is the first direct observation of non-zero v_2 for a heavy-flavour
 1647 particle. The large value of the charm v_2 at p_T around 2 GeV is interpreted as a signature of the
 1648 in-medium thermalization of charm quarks.

1649 At higher p_T a positive v_2 can be generated by the difference in the in-medium path lengths for charm
 1650 quarks emitted inside the in-plane azimuthal quadrants compared to those emitted in the out-of-plane
 1651 quadrants. The shorter path length for the in-plane partons implies less suppression, i.e. larger R_{AA}
 1652 for particles produced in this direction, than for those produced in the out-of-plane direction. In fact,
 1653 the results can be presented as an azimuthally-dependent R_{AA} , which is equivalent to the azimuthally-
 1654 integrated R_{AA} and the v_2 . The interpretation of the high- p_T v_2 as a path-length effect opens the
 1655 possibility of studying the in-medium path-length dependence of the parton energy loss.

1656 The v_2 results for D mesons are complemented by the recently reported elliptic-flow measurements
 1657 at forward rapidities ($2.5 < y < 4$) for the muons from heavy-flavour decays. They show an effect
 1658 of similar magnitude. Indication of non-zero heavy-flavour v_2 using the semi-leptonic decays were
 1659 previously published by RHIC experiments [2].

9 Quarkonium production

Measurements of quarkonium production promise to yield important information about the strongly-interacting system formed in heavy-ion collisions. The in-medium dissociation of quarkonium states in these collisions is expected to reflect both the state's binding energy as well as the temperature of the medium, leading to a sequential suppression or disappearance of the various charmonium and bottomonium states [197, 198].

J/ψ production in heavy-ion collisions has been studied over a wide range of collision energies at the CERN SPS and RHIC, with a strong suppression of J/ψ yields observed in central collisions for $\sqrt{s_{NN}} \approx 20$ to 200 GeV [199, 200, 201]. The interpretation of the observed suppression is complicated by the presence of Cold Nuclear Matter effects such as nuclear absorption and (anti-) shadowing. A quantitative description furthermore needs to take into account feeddown from excited states, which contribute a significant fraction of the inclusive J/ψ yield in p+p collisions. Finally, and perhaps most importantly, the large abundance of deconfined charm quarks at RHIC and higher energies requires the consideration of a recombination component in addition to direct J/ψ production, which may mask the suppression of the initial J/ψ formation [202, 203, 204, 205].

The large increase in the charm cross-section at LHC should magnify these regeneration effects compared to lower energy collisions, and thus provide the opportunity to disentangle suppression and regeneration effects in a study of the collision energy, p_T and rapidity dependence of J/ψ production.

The LHC collision energies also facilitate high statistics studies of the Υ family, where the three $\Upsilon(nS)$ states are connected by the common initial bottom pair production and similar kinematics, but distinguished by the hierarchy of their binding energies. In an in-medium dissociation picture, one therefore expects a distinct pattern in the suppression of the $\Upsilon(nS)$ states.

9.1 Charmonium suppression in PbPb collisions

J/ψ production in Pb+Pb collisions can be characterized relative to the N_{coll} -scaled p+p reference distributions, using the R_{CP} and R_{AA} nuclear modification factors introduced earlier. A strong suppression of high- p_T inclusive J/ψ in the dimuon decay channel was observed in central Pb+Pb collisions at $\sqrt{s_{NN}} = 2.76$ TeV relative to peripheral Pb+Pb collisions by ATLAS [206] and with respect to p+p collisions by CMS [195].

Results for the suppression of low p_T J/ψ production from ALICE are shown in Fig. 52 for $p_T > 0$ GeV/c (square markers) and $p_T > 3$ GeV/c (diamond markers), together with CMS data [195] for rapidity $1.6 < |y| < 2.4$ and $p_T > 3$ GeV/c (triangle markers).

Within uncertainties, neither p_T range shows a strong dependence of J/ψ suppression on rapidity. The suppression is stronger than predicted for shadowing effects in the Color Singlet Model [207] and the Color Evaporation Model [208]. Neither model predicts a strong rapidity dependence.

A stronger initial state suppression has been seen in the Color Glass Condensate (CGC) model [209], predicting $J/\psi R_{\text{AA}} \approx 0.5$. This prediction can be confronted with the p_T dependence of J/ψ suppression, where initial state suppression models typically lead to a stronger suppression at lower p_T . In contrast, possible J/ψ regeneration effects in statistical hadronization [202, 203] or partonic transport [205, 210] models are expected to enhance J/ψ yields at low p_T due to the higher phase space density of charm quarks at lower p_T .

Data from ALICE and CMS on the p_T dependence of the $J/\psi R_{\text{AA}}$ integrated over a wide range of Pb+Pb collision centrality are shown in Fig. 53. Although the measurements cover different rapidity ranges ($2.0 < |y| < 4.0$ vs $1.6 < |y| < 2.4$) a common, strong p_T evolution of $J/\psi R_{\text{AA}}$ is seen, ranging from ≈ 0.8 at low p_T to ≈ 0.4 for $p_T > 5$ GeV/c. This observation clearly favors models including a low- p_T enhancement due to charm recombination.

An even more striking observation is shown in the bottom panel of Fig. 53, which compares the

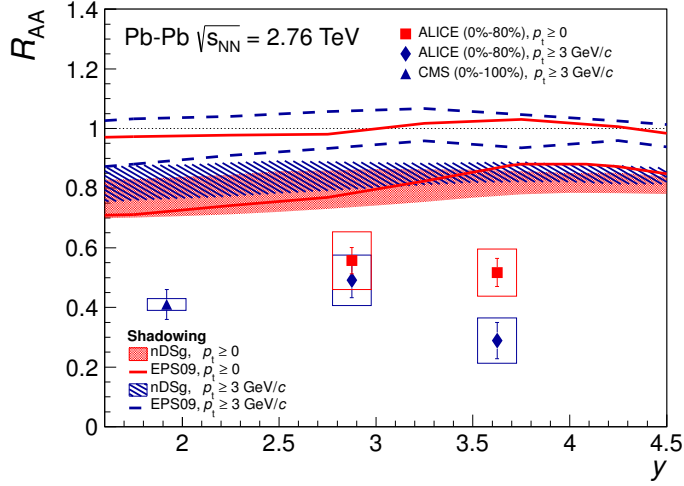


Figure 52: Inclusive J/ψ R_{AA} measured in $\text{Pb}+\text{Pb}$ collisions at $\sqrt{s_{NN}} = 2.76 \text{ TeV}$ as a function of rapidity for two p_T ranges. Total systematic uncertainties are displayed as open boxes, not including uncertainties on the p+p luminosity and T_{AA} scaling factor. These are 5.2% and 8.3% for ALICE and CMS, respectively. Two model predictions are shown [207, 208] including only shadowing effects for nDSg (shaded areas) and EPS09 (lines) nPDFs. Reproduced from [].

1706 ALICE forward-rapidity J/ψ R_{AA} for 0%–20% central $\text{Pb}+\text{Pb}$ collisions at $\sqrt{s_{NN}} = 2.76 \text{ TeV}$ with
 1707 central $\text{Au}+\text{Au}$ data from PHENIX at $\sqrt{s_{NN}} = 0.2 \text{ GeV}$ and rapidity $1.2 < |y| < 2.2$ [201]. At low p_T
 1708 the ALICE R_{AA} is about four times larger than that seen at the lower energy, while at the same time the
 1709 initial energy density of the system at LHC is estimated to be larger than at RHIC by a similar factor.
 1710 While a quantitative interpretation of this result will require a detailed understanding of CNM effects
 1711 at the two energies, the results are qualitatively consistent with the collision energy trend expected in
 1712 recombination approaches such as [205, 211, 210]. First results of J/ψ production in p-Pb collisions at
 1713 the LHC have recently been presented [212, 213], allowing the calibration of CNM effects vs final state
 1714 suppression and recombination.

1715 9.2 Charmonium elliptic flow

1716 An important question for models implementing the competing contributions of J/ψ dissociation in
 1717 the medium and J/ψ regeneration via charm quark recombination is the degree of charm quark thermalization.
 1718 The question of thermalization in heavy-ion collisions is typically addressed via studies of hydrodynamic flow.
 1719 ALICE has recently presented the first data suggesting non-zero elliptic flow in
 1720 $\text{Pb}+\text{Pb}$ collisions, providing important information on this topic.

1721 In a dissociation/recombination type approach, elliptic flow of the observed J/ψ can arise from
 1722 multiple contributions. Those J/ψ produced in the initial hard scattering traverse a shorter path in
 1723 the medium when travelling in-plane vs out-of-plane, leading to a possible azimuthal modulation of
 1724 J/ψ yields with respect to the event plane. If charm quarks participate in the collective expansion
 1725 of the medium, as suggested by the observed elliptic flow of open charm mesons, J/ψ 's produced by
 1726 recombination will pick up the elliptic flow of the charm quarks. These contributions can possibly be
 1727 disentangled by studies of the p_T dependence of J/ψ suppression and J/ψ elliptic flow.

1728 Measurements of the J/ψ elliptic flow by STAR for $\text{Au}+\text{Au}$ collisions at $\sqrt{s_{NN}} = 200 \text{ GeV}$ are consistent
 1729 with zero [214], although the large uncertainties prevent strong conclusions. The ALICE measurement
 1730 of $J/\psi v_2$ as a function of transverse momentum is shown in Fig. 54 for $\text{Pb}+\text{Pb}$ collisions in the
 1731 20%–60% centrality range. The $J/\psi v_2$ data, which have a significance of about 2σ in this centrality

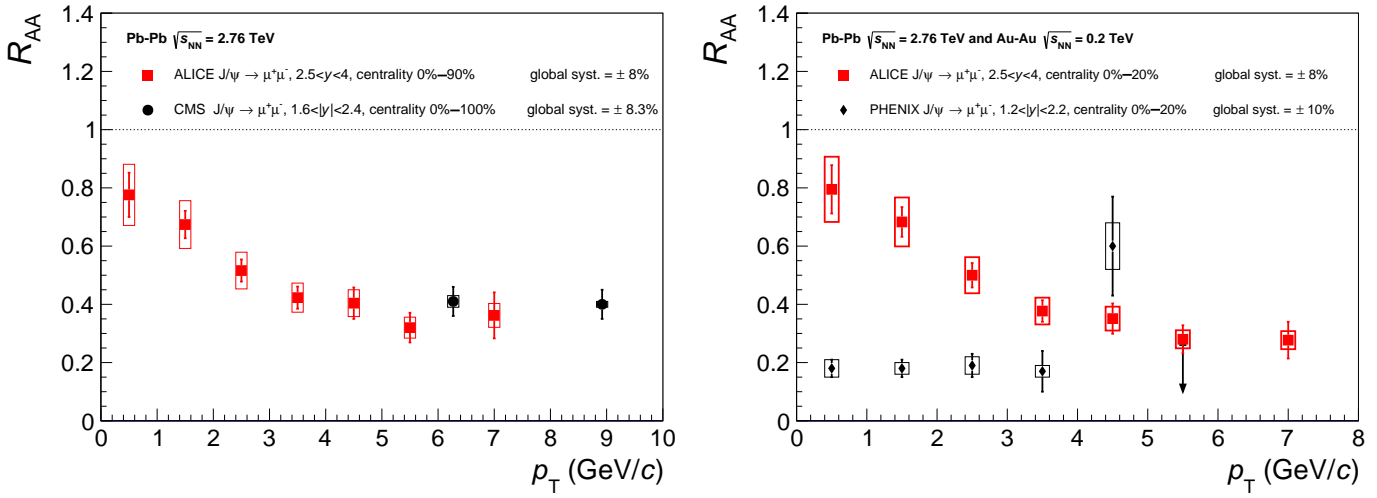


Figure 53: (Top): p_T dependence of $J/\psi R_{AA}$ measured by ALICE in Pb+Pb collisions (0–80% centrality) at $\sqrt{s_{NN}} = 2.76 \text{ TeV}$ compared to CMS [195] results (0–100% centrality) at the same energy. (Bottom): p_T dependence of the $J/\psi R_{AA}$ measured by ALICE in the 0%–20% most central Pb+Pb collisions at 2.76 TeV compared to PHENIX [201] results in the 0%–20% most central Au+Au collisions at 200 GeV. Reproduced from []

range, are compared to two transport model calculations [215, 216]. The models, which include charm quark recombination effects, are both compatible with the data within the current large experimental uncertainties. The comparison points to the importance of future high statistics measurements of J/ψ elliptic flow at high transverse momentum ($p_T > 5 \text{ GeV}/c$).

In combination, the p_T and collision energy dependence of $J/\psi R_{AA}$ and the indication of non-zero J/ψ elliptic flow suggest a possible contribution of charm quark recombination to J/ψ production in Pb+Pb collisions at LHC.

9.3 Upsilon suppression in PbPb

Measurements by CMS have provided the first high statistics look at Υ production in heavy-ion collisions [217]. The Υ family, with similar decay kinematics but a large variation of binding energies, provides an ideal laboratory to test dissociation effects in the hot medium produced in heavy-ion collisions. Compared to charmonium suppression studies, uncertainties due to CNM effects and feed-down from higher mass states are expected to be less important for the bottomonium family.

Dimuon invariant mass spectra in the Υ mass range obtained by CMS are shown in Fig. 55 for Pb+Pb (left) and p+p (right). The data correspond to integrated luminosities of $150 \mu\text{b}^{-1}$ and 230 nb^{-1} for Pb+Pb and p+p , respectively. For the p+p data, the excellent mass resolution of the CMS muon system allows a clear separation of the three $\Upsilon(nS)$ states. A similar mass resolution is achieved for Pb+Pb collisions. However, for Pb+Pb a strong suppression of the $\Upsilon(2S)$ state is evident from the distribution, and the $\Upsilon(3S)$ state is no longer visible above the continuum background. This is a striking visual confirmation of the expected Υ suppression pattern as a function of the $\Upsilon(nS)$ binding energy, and confirmed the first Υ measurements reported in [217].

The comparison of p+p and Pb+Pb data allows a characterization of the Υ suppression in terms of the nuclear modification factor R_{AA} . Integrating over centrality, the following R_{AA} values were measured for the $\Upsilon(nS)$ states:

$$R_{AA}(\Upsilon(1S)) = 0.56 \pm 0.08 \text{ (stat.)} \pm 0.07 \text{ (syst.)}, \quad (10)$$

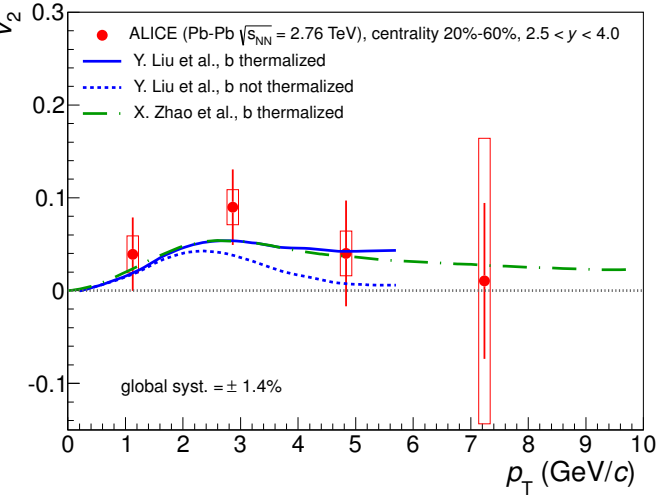


Figure 54: Inclusive J/ψ v_2 for $\text{Pb}+\text{Pb}$ collisions with 20–60% centrality at $\sqrt{s_{\text{NN}}} = 2.76 \text{ TeV}$ as a function of p_T . Also shown are calculations from two transport models [215, 216].

$$\begin{aligned} R_{\text{AA}}(\Upsilon(2\text{S})) &= 0.12 \pm 0.04 \text{ (stat.)} \pm 0.02 \text{ (syst.)}, \\ R_{\text{AA}}(\Upsilon(3\text{S})) &= 0.03 \pm 0.04 \text{ (stat.)} \pm 0.01 \text{ (syst.)}. \end{aligned}$$

The statistical significance of the $\Upsilon(3\text{S})$ peak above the continuum is less than one standard deviation. It should also be noted that there are significant feed-down contributions to the $\Upsilon(1\text{S})$ state that may reach $\approx 50\%$ [218, 219]. This could mean that directly produced $\Upsilon(1\text{S})$ state are largely unsuppressed, with the observed $\Upsilon(1\text{S})$ R_{AA} of 0.56 reflecting the dissociation of the higher mass excited states.

The $\Upsilon(1\text{S})$ and $\Upsilon(2\text{S})$ suppression was also studied as a function of centrality, as shown in Fig. 56. Here the relative suppression of $\Upsilon(1\text{S})$ and $\Upsilon(2\text{S})$ is characterized by the double ratio $(\Upsilon(2\text{S})/\Upsilon(1\text{S}))_{\text{PbPb}}/(\Upsilon(2\text{S})/\Upsilon(1\text{S}))_{\text{pp}}$ (Fig. 56 (left)) and the absolute suppression of the two states is shown as R_{AA} vs centrality (Fig. 56 (right)).

While R_{AA} shows a strongly falling trend with increasing collision centrality for both $\Upsilon(1\text{S})$ and $\Upsilon(2\text{S})$ (with a much stronger suppression for $\Upsilon(2\text{S})$), the double ratio does not exhibit a pronounced centrality dependence.

Overall, the data qualitatively exhibit the hierarchy in the $\Upsilon(n\text{S})$ suppression pattern expected based on the states' binding energies. Although the most peripheral bin is rather wide (50–100%), it is interesting to observe the strong suppression of the $\Upsilon(2\text{S})$ relative to the $\Upsilon(1\text{S})$ already for this bin. Future high statistics $\text{Pb}+\text{Pb}$ data should elucidate the onset of the Υ suppression in the most peripheral collisions, in combination with information on Υ suppression in small systems obtained from studies in p-Pb reference data.

10 Summary and outlook

This review has attempted to summarize the broad range of new data from the first two runs with lead ions in collision at the CERN Large Hadron Collider. To date, about $150 \mu\text{b}^{-1}$ of data have been collected by each of three major LHC experiments (ALICE, ATLAS and CMS), corresponding to about three billion minimum-bias events sampled between them. The three detectors are all large, multi-purpose spectrometers, with ALICE being optimized for particle identification at low p_T , photons, and muons at forward rapidity; ATLAS and CMS optimized for precision measurements of high p_T objects (tracks, jets, muons, electrons and photons). The centrality of the collision is estimated in all of

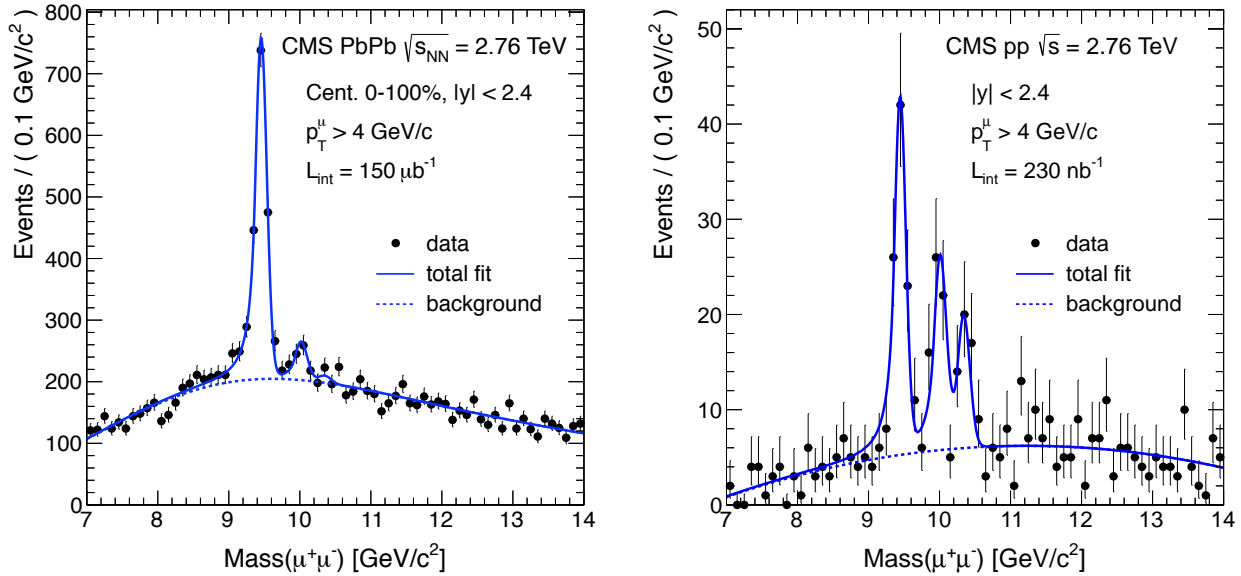


Figure 55: Dimuon invariant-mass distributions in Pb+Pb (left) and p+p (right) at $\sqrt{s_{\text{NN}}} = 2.76 \text{ TeV}$. Pb+Pb and p+p were reconstructed with identical reconstruction algorithms and analysis selections. The lines show simultaneous fits to both datasets for signal + background (solid) and background-only (dashed).

the experiments by partitioning the event distribution of the forward transverse energy or multiplicity into intervals corresponding to percentiles of the collected events, and related to the nuclear overlap geometry using Glauber models. Good agreement in the centrality estimation is found between the experiments, as illustrated by the charged particle multiplicity per participant pair, as a function of centrality. The centrality is also crucial for measuring the suppression of high p_T hadrons, relative to what is measured in proton-proton collisions, via the ratio $R_{\text{AA}}(p_T)$. The value of R_{AA} is found to be strongly suppressed at low p_T , but then to rise and plateau again at a level of about 0.5, similar to what is found for jet suppression. The detailed study of identified particle yields shows good consistency with thermal models, except for an anomalous suppression of protons. Just as it was at the CERN SPS and RHIC, the yield of strange hadrons, and especially multi-strange, is substantially enhanced in heavy-ion collisions. Two particle correlations provide a rich handle on soft physics in heavy ions, giving insight into the space-time structure (via HBT measurements), jets, and the so-called “ridge”. Despite not being a full jet measurement, correlations provide similar insight into the suppression of the away-side region and an enhancement on the near-side suggestive of modified jet fragmentation in medium. The geometric dependence of charge fluctuations and the charged balance function provide information on the fate of conserved quantities in the medium evolution. Finally, more sophisticated correlations meant to look for the Chiral Magnetic Effect (CME) find consistency with STAR data from RHIC, but no clear indication of the CME.

Collective flow has been extensively measured at the LHC by all the experiments. Both two-particle and multi-particle methods have been used, which have varying sensitivity to the presence of non-flow effects, such as correlations from jet production and fragmentation. Various scaling behaviors have been observed, both for the absolute value of v_2 (even at large p_T), as well as v_2 scaled by the overlap eccentricity. The LHC has also seen an explosion in the measurement of higher-order harmonics up to v_6 , and the rapidity-even and -odd contributions to v_1 , all of which should allow more stringent tests of hydrodynamic models. Event-by-event flow fluctuations have also been measured both by unfolding reconstructed distributions as well as by using combinations of cumulants. Good consistency has been

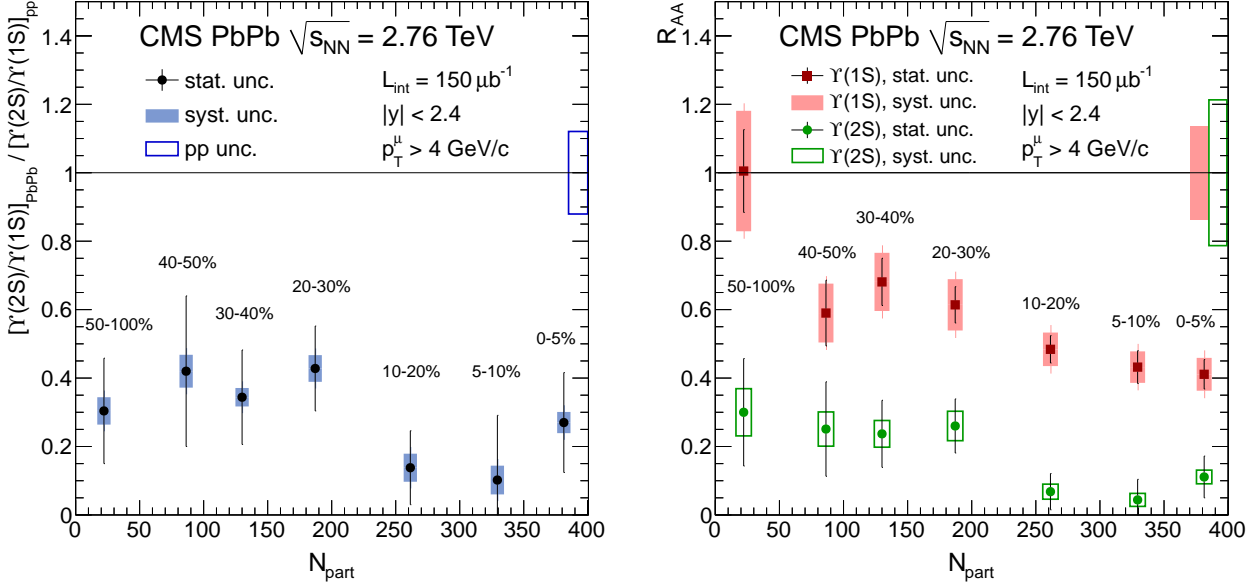


Figure 56: (Left): Centrality dependence of the $\Upsilon(1S)$ and $\Upsilon(2S)$ double ratios for 2.76 TeV Pb+Pb collisions. (Right): Centrality dependence of R_{AA} for $\Upsilon(1S)$ and $\Upsilon(2S)$ for 2.76 TeV Pb+Pb collisions. Error bars show statistical uncertainties, while the boxes around the points show systematic uncertainties. Common, N_{part} -independent uncertainties are represented by the boxes at unity. Reproduced from []

1807 found for v_2 fluctuations over a wide range of centrality, while differences in v_3 fluctuations may be
1808 attributable to the different methods used to extract it.

1809 Hard processes have been well calibrated using measurements of electro-weak bosons: both W
1810 and Z as well as photons. All of these particles are found to have cross sections (both total and
1811 differential) consistent with perturbative QCD calculations scaled by the number of binary collisions.
1812 No substantial modifications of the nuclear parton distributions functions appears to be needed, due
1813 to the good agreement of rapidity-dependent quantities. In this context, the modifications of jets in
1814 more central heavy ion collisions can more clearly be attributed to the energy loss of partons traversing
1815 the hot, dense medium. Energy loss has been addressed using several techniques, from dijet imbalance
1816 (despite measurements showing full energy containment) to single jet suppression, both inclusive and
1817 differentially in φ . Jet fragmentation in heavy-ion collisions has also been measured and found to be
1818 substantially modified, especially at large angles with respect to the jet axis. Correlations of jets with
1819 photons shows a similar energy loss effect, using a process that allows tagging of the initial hardness
1820 scale.

1821 Heavy flavor is produced copiously at the LHC and is expected to show different energy loss than
1822 light quarks. Early results show strong suppression of D mesons as well as J/Ψ from B-meson decays,
1823 as well as a significant signal that D mesons participate in the collective flow. Quarkonia (both J/ψ
1824 and Υ states) have also been studied over a wide range of p_{T} and rapidity. The J/ψ yield is found
1825 to be suppressed at a similar level over a wide rapidity range, although the suppression at low p_{T} is
1826 not as strong as it was at RHIC, suggesting the possibility of regeneration processes due to the large
1827 charm quark production rates. Similar to what was found for open charm, the forward J/ψ have a
1828 2σ significant v_2 signal, potentially larger than was found at RHIC. The Υ family show interesting
1829 behavior in heavy ion collisions, with all states being suppressed relative to proton-proton collisions,
1830 and the more weakly bound higher states showing stronger suppression than the more tightly bound

1831 1S state.

1832 The results shown here are mainly the ones submitted to journals for publication, and many more
1833 results are in preparation. Thus, this review should be seen mainly as a snapshot of the state of the field.
1834 The wealth of upcoming results from the first two lead–lead runs, and the upcoming runs with higher
1835 energy ($\sqrt{s_{\text{NN}}} = 5.5$ TeV) and luminosity exceeding the design instantaneous luminosity of $10^{27} \text{ cm}^{-2}\text{s}^{-1}$
1836 should provide even further insight into the nature and properties of the hot, dense matter formed in
1837 nuclear collisions at the LHC.

1838 The progress towards a detailed characterization of this strongly interacting state of matter will
1839 generally focus more on rarer probes, and the study of their coupling with the medium and hadronization.
1840 These will include heavy-flavour particles, quarkonia states, real and virtual photons, jets and
1841 their correlations with other probes (particularly photons and electroweak bosons). The cross sections
1842 of all these processes are significantly larger at LHC than at previous accelerators. In addition, the
1843 interaction with the medium of such hard probes is better controlled theoretically than the propagation
1844 of soft light partons.

1845 To achieve these goals high integrated luminosities and high precision measurements are required,
1846 which will give access to the rare physics channels needed to understand the dynamics of this condensed
1847 phase of QCD. Therefore, the LHC collaborations are upgrading the current detectors to enhance their
1848 vertexing capability, and allowing data taking at substantially higher rates. The upgrade strategy for
1849 heavy-ion running is formulated under the assumption that, after the second long shutdown in 2018, the
1850 LHC will progressively increase its luminosity with Pb beams eventually reaching an interaction rate
1851 of about 50 kHz, i.e. instantaneous luminosities $6 \times 10^{27} \text{ cm}^{-2}\text{s}^{-1}$. The proposed plan [220] envisage
1852 to accumulate 10 nb^{-1} of Pb–Pb collisions inspecting $\mathcal{O}(10^{10})$ interactions, which is needed to address
1853 the proposed physics programme, with focus on rare probes both at low- and high-transverse momenta
1854 as well as on the multi-dimensional analysis of such probes with respect to centrality, event plane, and
1855 multi-particle correlations.

1856 Acknowledgments

1857 We would like to thank to our collaborators with whom most of the LHC results presented here were
1858 obtained. In addition, we acknowledge helpful discussions with Federico Antinori, Michele Floris, Jan
1859 Fiete Grosse-Oetringhaus, and Alexander Kalweit during the preparation of this article.

1860 References

- 1861 [1] L. Evans, P. Bryant, LHC Machine, JINST 3 (2008) S08001. doi:10.1088/1748-0221/3/08/S08001.
- 1862 [2] G. Jarlskog, D. Rein, ECFA Large Hadron Collider Workshop, Aachen, Germany, 4–9 Oct 1990:
1863 Proceedings.
- 1864 [3] S. Borsanyi, et al., Is there still any T_c mystery in lattice QCD? Results with physical masses in
1865 the continuum limit III, JHEP 1009 (2010) 073. arXiv:1005.3508, doi:10.1007/JHEP09(2010)073.
- 1866 [4] R. Tribble, et al., The Frontiers of Nuclear Science, A Long Range PlanarXiv:0809.3137.
- 1867 [5] B. Muller, J. Schukraft, B. Wyslouch, First Results from Pb+Pb collisions at the LHC,
1868 Ann.Rev.Nucl.Part.Sci. 62 (2012) 361–386. arXiv:1202.3233, doi:10.1146/annurev-nucl-102711-
1869 094910.

- [6] N. Armesto, N. Borghini, S. Jeon, U. Wiedemann, S. Abreu, et al., Heavy Ion Collisions at the LHC - Last Call for Predictions, *J.Phys. G* 35 (2008) 054001. arXiv:0711.0974, doi:10.1088/0954-3899/35/5/054001.
- [7] K. Aamodt, et al., The ALICE experiment at the CERN LHC, *JINST* 3 (2008) S08002. doi:10.1088/1748-0221/3/08/S08002.
- [8] G. Aad, et al., The ATLAS Experiment at the CERN Large Hadron Collider, *JINST* 3 (2008) S08003. doi:10.1088/1748-0221/3/08/S08003.
- [9] S. Chatrchyan, et al., The CMS experiment at the CERN LHC, *JINST* 3 (2008) S08004. doi:10.1088/1748-0221/3/08/S08004.
- [10] M. L. Miller, K. Reygers, S. J. Sanders, P. Steinberg, Glauber modeling in high energy nuclear collisions, *Ann.Rev.Nucl.Part.Sci.* 57 (2007) 205–243. arXiv:nucl-ex/0701025, doi:10.1146/annurev.nucl.57.090506.123020.
- [11] R. Glauber, Cross-sections in deuterium at high-energies, *Phys.Rev.* 100 (1955) 242–248. doi:10.1103/PhysRev.100.242.
- [12] R. J. Glauber, Quantum Optics and Heavy Ion Physics, *Nucl.Phys.* A774 (2006) 3–13. arXiv:nucl-th/0604021, doi:10.1016/j.nuclphysa.2006.06.009.
- [13] A. Shor, R. S. Longacre, Effects of Secondary Interactions in Proton - Nucleus and Nucleus-nucleus Collisions Using the Hijing Event Generator, *Phys.Lett.* B218 (1989) 100. doi:10.1016/0370-2693(89)90483-8.
- [14] B. Alver, M. Baker, C. Loizides, P. Steinberg, The PHOBOS Glauber Monte Carlo arXiv:0805.4411.
- [15] H. De Vries, C. De Jager, C. De Vries, Nuclear charge and magnetization density distribution parameters from elastic electron scattering, *Atom.Data Nucl.Data Tabl.* 36 (1987) 495–536. doi:10.1016/0092-640X(87)90013-1.
- [16] B. Abelev, et al., Centrality determination of Pb-Pb collisions at $\sqrt{s_{NN}} = 2.76$ TeV with ALICE, *Phys.Rev.* C88 (2013) 044909. arXiv:1301.4361, doi:10.1103/PhysRevC.88.044909.
- [17] R. Bruce, S. Gilardoni, J. Jowett, D. Bocian, Beam losses from ultra-peripheral nuclear collisions between $(\text{Pb-208})^{**}82+$ ions in the Large Hadron Collider and their alleviation, *Phys.Rev.ST Accel.Beams* 12 (2009) 071002. arXiv:0908.2527, doi:10.1103/PhysRevSTAB.12.071002.
- [18] B. Abelev, et al., Measurement of the Cross Section for Electromagnetic Dissociation with Neutron Emission in Pb-Pb Collisions at $\sqrt{s_{NN}} = 2.76$ TeV, *Phys.Rev.Lett.* 109 (2012) 252302. arXiv:1203.2436, doi:10.1103/PhysRevLett.109.252302.
- [19] G. Aad, et al., Measurement of the centrality dependence of the charged particle pseudorapidity distribution in lead-lead collisions at $\sqrt{s_{NN}} = 2.76$ TeV with the ATLAS detector, *Phys.Lett.* B710 (2012) 363–382. arXiv:1108.6027, doi:10.1016/j.physletb.2012.02.045.
- [20] S. Chatrchyan, et al., Dependence on pseudorapidity and centrality of charged hadron production in PbPb collisions at a nucleon-nucleon centre-of-mass energy of 2.76 TeV, *JHEP* 1108 (2011) 141. arXiv:1107.4800, doi:10.1007/JHEP08(2011)141.

- [21] K. Aamodt, et al., Charged-particle multiplicity density at mid-rapidity in central Pb-Pb collisions at $\sqrt{s_{NN}} = 2.76$ TeV, Phys.Rev.Lett. 105 (2010) 252301. arXiv:1011.3916, doi:10.1103/PhysRevLett.105.252301.
- [22] K. Aamodt, et al., Centrality dependence of the charged-particle multiplicity density at mid-rapidity in Pb-Pb collisions at $\sqrt{s_{NN}} = 2.76$ TeV, Phys.Rev.Lett. 106 (2011) 032301. arXiv:1012.1657, doi:10.1103/PhysRevLett.106.032301.
- [23] S. Adler, et al., Systematic studies of the centrality and $s(\text{NN})^{**(1/2)}$ dependence of the $d E(T) / d \eta$ and $d N(\text{ch}) / d \eta$ in heavy ion collisions at mid-rapidity, Phys.Rev. C71 (2005) 034908. arXiv:nucl-ex/0409015, doi:10.1103/PhysRevC.71.049901, 10.1103/PhysRevC.71.034908.
- [24] N. Armesto, C. A. Salgado, U. A. Wiedemann, Relating high-energy lepton-hadron, proton-nucleus and nucleus-nucleus collisions through geometric scaling, Phys.Rev.Lett. 94 (2005) 022002. arXiv:hep-ph/0407018, doi:10.1103/PhysRevLett.94.022002.
- [25] D. Kharzeev, E. Levin, M. Nardi, Color glass condensate at the LHC: Hadron multiplicities in pp, pA and AA collisions, Nucl.Phys. A747 (2005) 609–629. arXiv:hep-ph/0408050, doi:10.1016/j.nuclphysa.2004.10.018.
- [26] J. L. Albacete, A. Dumitru, A model for gluon production in heavy-ion collisions at the LHC with rcBK unintegrated gluon densities arXiv:1011.5161.
- [27] E. Abbas, et al., Centrality dependence of the pseudorapidity density distribution for charged particles in Pb-Pb collisions at $\sqrt{s_{NN}} = 2.76$ TeV, Phys.Lett. B726 (2013) 610–622. arXiv:1304.0347, doi:10.1016/j.physletb.2013.09.022.
- [28] I. Bearden, et al., Pseudorapidity distributions of charged particles from Au+Au collisions at the maximum RHIC energy, Phys.Rev.Lett. 88 (2002) 202301. arXiv:nucl-ex/0112001, doi:10.1103/PhysRevLett.88.202301.
- [29] B. Alver, et al., Phobos results on charged particle multiplicity and pseudorapidity distributions in Au+Au, Cu+Cu, d+Au, and p+p collisions at ultra-relativistic energies, Phys.Rev. C83 (2011) 024913. arXiv:1011.1940, doi:10.1103/PhysRevC.83.024913.
- [30] S. Chatrchyan, et al., Measurement of the pseudorapidity and centrality dependence of the transverse energy density in PbPb collisions at $\sqrt{s_{NN}} = 2.76$ TeV, Phys.Rev.Lett. 109 (2012) 152303. arXiv:1205.2488, doi:10.1103/PhysRevLett.109.152303.
- [31] J. Bjorken, Highly Relativistic Nucleus-Nucleus Collisions: The Central Rapidity Region, Phys.Rev. D27 (1983) 140–151. doi:10.1103/PhysRevD.27.140.
- [32] K. Aamodt, et al., Suppression of Charged Particle Production at Large Transverse Momentum in Central Pb-Pb Collisions at $\sqrt{s_{NN}} = 2.76$ TeV, Phys.Lett. B696 (2011) 30–39. arXiv:1012.1004, doi:10.1016/j.physletb.2010.12.020.
- [33] S. Chatrchyan, et al., Study of high-pT charged particle suppression in PbPb compared to pp collisions at $\sqrt{s_{NN}} = 2.76$ TeV, Eur.Phys.J. C72 (2012) 1945. arXiv:1202.2554, doi:10.1140/epjc/s10052-012-1945-x.
- [34] A. Dainese, C. Loizides, G. Paic, Leading-particle suppression in high energy nucleus-nucleus collisions, Eur.Phys.J. C38 (2005) 461–474. arXiv:hep-ph/0406201, doi:10.1140/epjc/s2004-02077-x.

- [35] I. Vitev, M. Gyulassy, High p_T tomography of $d + \text{Au}$ and $\text{Au}+\text{Au}$ at SPS, RHIC, and LHC, Phys.Rev.Lett. 89 (2002) 252301. arXiv:hep-ph/0209161, doi:10.1103/PhysRevLett.89.252301.
- [36] I. Vitev, Jet tomography, J.Phys. G30 (2004) S791–S800. arXiv:hep-ph/0403089, doi:10.1088/0954-3899/30/8/019.
- [37] C. A. Salgado, U. A. Wiedemann, Calculating quenching weights, Phys.Rev. D68 (2003) 014008. arXiv:hep-ph/0302184, doi:10.1103/PhysRevD.68.014008.
- [38] N. Armesto, A. Dainese, C. A. Salgado, U. A. Wiedemann, Testing the color charge and mass dependence of parton energy loss with heavy-to-light ratios at RHIC and CERN LHC, Phys.Rev. D71 (2005) 054027. arXiv:hep-ph/0501225, doi:10.1103/PhysRevD.71.054027.
- [39] T. Renk, H. Holopainen, R. Paatelainen, K. J. Eskola, Systematics of the charged-hadron p_T spectrum and the nuclear suppression factor in heavy-ion collisions from $\sqrt{s} = 200$ GeV to $\sqrt{s} = 2.76$ TeV, Phys.Rev. C84 (2011) 014906. arXiv:1103.5308, doi:10.1103/PhysRevC.84.014906.
- [40] B. Abelev, et al., Centrality Dependence of Charged Particle Production at Large Transverse Momentum in Pb–Pb Collisions at $\sqrt{s_{NN}} = 2.76$ TeV, Phys.Lett. B720 (2013) 52–62. arXiv:1208.2711, doi:10.1016/j.physletb.2013.01.051.
- [41] B. Abelev, et al., Pion, Kaon, and Proton Production in Central Pb–Pb Collisions at $\sqrt{s_{NN}} = 2.76$ TeV, Phys.Rev.Lett. 109 (2012) 252301. arXiv:1208.1974, doi:10.1103/PhysRevLett.109.252301.
- [42] B. Abelev, et al., Centrality dependence of π , K, p production in Pb–Pb collisions at $\sqrt{s_{NN}} = 2.76$ TeV, Phys.Rev. C88 (2013) 044910. arXiv:1303.0737, doi:10.1103/PhysRevC.88.044910.
- [43] E. Schnedermann, J. Sollfrank, U. W. Heinz, Thermal phenomenology of hadrons from 200-A/GeV S+S collisions, Phys.Rev. C48 (1993) 2462–2475. arXiv:nucl-th/9307020, doi:10.1103/PhysRevC.48.2462.
- [44] C. Shen, U. Heinz, P. Huovinen, H. Song, Radial and elliptic flow in Pb+Pb collisions at the Large Hadron Collider from viscous hydrodynamic, Phys.Rev. C84 (2011) 044903. arXiv:1105.3226, doi:10.1103/PhysRevC.84.044903.
- [45] P. Bozek, I. Wyskiel-Piekarska, Particle spectra in Pb-Pb collisions at $\sqrt{s_{NN}} = 2.76$ TeV, Phys.Rev. C85 (2012) 064915. arXiv:1203.6513, doi:10.1103/PhysRevC.85.064915.
- [46] K. Werner, I. Karpenko, M. Bleicher, T. Pierog, S. Porteboeuf-Houssais, Jets, Bulk Matter, and their Interaction in Heavy Ion Collisions at Several TeV, Phys.Rev. C85 (2012) 064907. arXiv:1203.5704, doi:10.1103/PhysRevC.85.064907.
- [47] I. Karpenko, Y. Sinyukov, K. Werner, Uniform description of bulk observables in hydrokinetic model of $A + A$ collisions at RHIC and LHC, Phys.Rev. C87 (2013) 024914. arXiv:1204.5351, doi:10.1103/PhysRevC.87.024914.
- [48] Y. Karpenko, Y. Sinyukov, Femtoscopic scales in central A+A collisions at RHIC and LHC energies in hydrokinetic model, J.Phys. G38 (2011) 124059. arXiv:1107.3745, doi:10.1088/0954-3899/38/12/124059.
- [49] S. Bass, M. Belkacem, M. Bleicher, M. Brandstetter, L. Bravina, et al., Microscopic models for ultrarelativistic heavy ion collisions, Prog.Part.Nucl.Phys. 41 (1998) 255–369. arXiv:nucl-th/9803035, doi:10.1016/S0146-6410(98)00058-1.

- [50] P. Bozek, Flow and interferometry in 3+1 dimensional viscous hydrodynamics, Phys.Rev. C85 (2012) 034901. arXiv:1110.6742, doi:10.1103/PhysRevC.85.034901.
- [51] P. Bozek, Hydrodynamic flow from RHIC to LHC, Acta Phys.Polon. B43 (2012) 689. arXiv:1111.4398, doi:10.5506/APhysPolB.43.689.
- [52] B. Abelev, et al., Production of charged pions, kaons and (anti) protons at large transverse momentum in pp and in Pb–Pb collisions at $\sqrt{s_{NN}} = 2.76$ TeV arXiv:XXXX.XXXX.
- [53] R. C. Hwa, C. Yang, Proton enhancement at large $p(T)$ at LHC without structure in associated-particle distribution, Phys.Rev.Lett. 97 (2006) 042301. arXiv:nucl-th/0603053, doi:10.1103/PhysRevLett.97.042301.
- [54] B. Abelev, et al., Identified baryon and meson distributions at large transverse momenta from Au+Au collisions at $s(NN)^{**}(1/2) = 200$ -GeV, Phys.Rev.Lett. 97 (2006) 152301. arXiv:nucl-ex/0606003, doi:10.1103/PhysRevLett.97.152301.
- [55] A. Adare, et al., Spectra and ratios of identified particles in Au+Au and d+Au collisions at $\sqrt{s_{NN}}=200$ GeV, Phys.Rev. C88 (2013) 024906. arXiv:1304.3410, doi:10.1103/PhysRevC.88.024906.
- [56] R. Fries, B. Muller, C. Nonaka, S. Bass, Hadron production in heavy ion collisions: Fragmentation and recombination from a dense parton phase, Phys.Rev. C68 (2003) 044902. arXiv:nucl-th/0306027, doi:10.1103/PhysRevC.68.044902.
- [57] P. Aurenche, B. Zakharov, Jet color chemistry and anomalous baryon production in AA-collisions, Eur.Phys.J. C71 (2011) 1829. arXiv:1109.6819, doi:10.1140/epjc/s10052-011-1829-5.
- [58] J. Rafelski, B. Muller, Strangeness Production in the Quark - Gluon Plasma, Phys.Rev.Lett. 48 (1982) 1066. doi:10.1103/PhysRevLett.48.1066.
- [59] P. Koch, B. Muller, J. Rafelski, Strangeness in Relativistic Heavy Ion Collisions, Phys.Rept. 142 (1986) 167–262. doi:10.1016/0370-1573(86)90096-7.
- [60] S. Margetis, K. Safarik, O. Villalobos Baillie, Strangeness production in heavy-ion collisions, Ann.Rev.Nucl.Part.Sci. 50 (2000) 299–342. doi:10.1146/annurev.nucl.50.1.299.
- [61] E. Andersen, et al., Strangeness enhancement at mid-rapidity in Pb Pb collisions at 158-A-GeV/c, Phys.Lett. B449 (1999) 401–406. doi:10.1016/S0370-2693(99)00140-9.
- [62] F. Antinori, et al., Strangeness enhancements at central rapidity in 40 A GeV/c Pb-Pb collisions, J.Phys. G37 (2010) 045105. arXiv:1001.1884, doi:10.1088/0954-3899/37/4/045105.
- [63] C. Alt, et al., Energy dependence of Lambda and Xi production in central Pb+Pb collisions at A-20, A-30, A-40, A-80, and A-158 GeV measured at the CERN Super Proton Synchrotron, Phys.Rev. C78 (2008) 034918. arXiv:0804.3770, doi:10.1103/PhysRevC.78.034918.
- [64] B. Abelev, et al., Enhanced strange baryon production in Au + Au collisions compared to p + p at $s(NN)^{**}(1/2) = 200$ -GeV, Phys.Rev. C77 (2008) 044908. arXiv:0705.2511, doi:10.1103/PhysRevC.77.044908.
- [65] B. B. Abelev, et al., Multi-strange baryon production at mid-rapidity in Pb-Pb collisions at $\sqrt{s_{NN}} = 2.76$ TeV arXiv:1307.5543.

- [66] B. B. Abelev, et al., K_s^0 and Λ production in Pb-Pb collisions at $\text{sqrt}(s_{\text{NN}}) = 2.76 \text{ TeV}$, Phys.Rev.Lett. 111 (2013) 222301. arXiv:1307.5530, doi:10.1103/PhysRevLett.111.222301.
- [67] H. Song, U. W. Heinz, Causal viscous hydrodynamics in 2+1 dimensions for relativistic heavy-ion collisions, Phys.Rev. C77 (2008) 064901. arXiv:0712.3715, doi:10.1103/PhysRevC.77.064901.
- [68] H. Song, U. W. Heinz, Multiplicity scaling in ideal and viscous hydrodynamics, Phys.Rev. C78 (2008) 024902. arXiv:0805.1756, doi:10.1103/PhysRevC.78.024902.
- [69] H. Song, S. A. Bass, U. Heinz, Elliptic flow in 200 A GeV Au+Au collisions and 2.76 A TeV Pb+Pb collisions: insights from viscous hydrodynamics + hadron cascade hybrid model, Phys.Rev. C83 (2011) 054912. arXiv:1103.2380, doi:10.1103/PhysRevC.83.054912, 10.1103/PhysRevC.87.019902.
- [70] K. Werner, Lambda-to-Kaon Ratio Enhancement in Heavy Ion Collisions at Several TeV, Phys.Rev.Lett. 109 (2012) 102301. arXiv:1204.1394, doi:10.1103/PhysRevLett.109.129903, 10.1103/PhysRevLett.109.102301.
- [71] M. Aggarwal, et al., K^{*0} production in Cu+Cu and Au+Au collisions at $\sqrt{s_N N} = 62.4 \text{ GeV}$ and 200 GeV, Phys.Rev. C84 (2011) 034909. arXiv:1006.1961, doi:10.1103/PhysRevC.84.034909.
- [72] B. Abelev, Observation of an Antimatter Hypernucleus, Science 328 (2010) 58–62. arXiv:1003.2030, doi:10.1126/science.1183980.
- [73] A. Andronic, P. Braun-Munzinger, J. Stachel, Thermal hadron production in relativistic nuclear collisions: The Hadron mass spectrum, the horn, and the QCD phase transition, Phys.Lett. B673 (2009) 142–145. arXiv:0812.1186, doi:10.1016/j.physletb.2009.02.014, 10.1016/j.physletb.2009.06.021.
- [74] A. Andronic, P. Braun-Munzinger, K. Redlich, J. Stachel, The thermal model on the verge of the ultimate test: particle production in Pb-Pb collisions at the LHC, J.Phys. G38 (2011) 124081. arXiv:1106.6321, doi:10.1088/0954-3899/38/12/124081.
- [75] J. Cleymans, K. Redlich, Unified description of freezeout parameters in relativistic heavy ion collisions, Phys.Rev.Lett. 81 (1998) 5284–5286. arXiv:nucl-th/9808030, doi:10.1103/PhysRevLett.81.5284.
- [76] F. Becattini, R. Fries, The QCD confinement transition: Hadron formationarXiv:0907.1031.
- [77] B. Abelev, et al., Systematic Measurements of Identified Particle Spectra in pp, d^+ Au and Au+Au Collisions from STAR, Phys.Rev. C79 (2009) 034909. arXiv:0808.2041, doi:10.1103/PhysRevC.79.034909.
- [78] S. Adler, et al., Identified charged particle spectra and yields in Au+Au collisions at $S(\text{NN})^{**1/2} = 200\text{-GeV}$, Phys.Rev. C69 (2004) 034909. arXiv:nucl-ex/0307022, doi:10.1103/PhysRevC.69.034909.
- [79] J. Steinheimer, J. Aichelin, M. Bleicher, Non-thermal p/π ratio at LHC as a consequence of hadronic final state interactions, Phys.Rev.Lett. 110 (2013) 042501. arXiv:1203.5302, doi:10.1103/PhysRevLett.110.042501.
- [80] F. Becattini, M. Bleicher, T. Kollegger, T. Schuster, J. Steinheimer, et al., Hadron Formation in Relativistic Nuclear Collisions and the QCD Phase Diagram, Phys.Rev.Lett. 111 (2013) 082302. arXiv:1212.2431, doi:10.1103/PhysRevLett.111.082302.

- [81] Y. Pan, S. Pratt, Baryon Annihilation in Heavy Ion CollisionsarXiv:1210.1577.
- [82] C. Ratti, R. Bellwied, M. Cristoforetti, M. Barbaro, Are there hadronic bound states above the QCD transition temperature?, Phys.Rev. D85 (2012) 014004. arXiv:1109.6243, doi:10.1103/PhysRevD.85.014004.
- [83] R. Hagedorn, Statistical thermodynamics of strong interactions at high-energies, Nuovo Cim.Suppl. 3 (1965) 147–186.
- [84] R. Hagedorn, Hadronic matter near the boiling point, Nuovo Cim. A56 (1968) 1027–1057. doi:10.1007/BF02751614.
- [85] J. Rafelski, J. Letessier, Particle Production in $s_{NN} = 2.76$ TeV Heavy Ion Collisions, Phys.Rev. C83 (2011) 054909. arXiv:1012.1649, doi:10.1103/PhysRevC.83.054909.
- [86] M. Petran, J. Letessier, V. Petracek, J. Rafelski, Hadron production and QGP Hadronization in Pb–Pb collisions at $\sqrt{s_{NN}} = 2.76$ TeV, Phys.Rev. C88 (2013) 034907. arXiv:1303.2098, doi:10.1103/PhysRevC.88.034907.
- [87] R. Hanbury Brown, R. Twiss, A New type of interferometer for use in radio astronomy, Phil.Mag. 45 (1954) 663–682.
- [88] K. Aamodt, et al., Two-pion Bose-Einstein correlations in central Pb-Pb collisions at $\text{sqrt}(s_{NN}) = 2.76$ TeV, Phys.Lett. B696 (2011) 328–337. arXiv:1012.4035, doi:10.1016/j.physletb.2010.12.053.
- [89] J. Adams, et al., Pion interferometry in Au+Au collisions at $S(\text{NN})^{**}(1/2) = 200\text{-GeV}$, Phys.Rev. C71 (2005) 044906. arXiv:nucl-ex/0411036, doi:10.1103/PhysRevC.71.044906.
- [90] M. A. Lisa, S. Pratt, R. Soltz, U. Wiedemann, Femtoscopy in relativistic heavy ion collisions, Ann.Rev.Nucl.Part.Sci. 55 (2005) 357–402. arXiv:nucl-ex/0505014, doi:10.1146/annurev.nucl.55.090704.151533.
- [91] M. Chojnacki, W. Florkowski, W. Broniowski, A. Kisiel, Soft heavy-ion physics from hydrodynamics with statistical hadronization: Predictions for collisions at $S^{**}(1/2)(\text{NN}) = 5.5\text{-TeV}$, Phys.Rev. C78 (2008) 014905. arXiv:0712.0947, doi:10.1103/PhysRevC.78.014905.
- [92] I. Karpenko, Y. Sinyukov, Energy dependence of pion interferometry scales in ultra-relativistic heavy ion collisions, Phys.Lett. B688 (2010) 50–54. arXiv:0912.3457, doi:10.1016/j.physletb.2010.03.068.
- [93] M. Herrmann, G. Bertsch, Source dimensions in ultrarelativistic heavy ion collisions, Phys.Rev. C51 (1995) 328–338. arXiv:hep-ph/9405373, doi:10.1103/PhysRevC.51.328.
- [94] B. B. Abelev, et al., Two and Three-Pion Quantum Statistics Correlations in Pb-Pb Collisions at $\sqrt{s_{NN}}=2.76$ TeV at the LHC arXiv:1310.7808.
- [95] B. Abelev, et al., Net-Charge Fluctuations in Pb-Pb collisions at $\sqrt{s_N}N = 2.76$ TeV, Phys.Rev.Lett. 110 (2013) 152301. arXiv:1207.6068, doi:10.1103/PhysRevLett.110.152301.
- [96] S. Jeon, V. Koch, Charged particle ratio fluctuation as a signal for QGP, Phys.Rev.Lett. 85 (2000) 2076–2079. arXiv:hep-ph/0003168, doi:10.1103/PhysRevLett.85.2076.
- [97] S. Jeon, V. Koch, Event by event fluctuations arXiv:hep-ph/0304012.

- [98] B. Abelev, et al., Beam-Energy and System-Size Dependence of Dynamical Net Charge Fluctuations, Phys.Rev. C79 (2009) 024906. arXiv:0807.3269, doi:10.1103/PhysRevC.79.024906.
- [99] B. B. Abelev, et al., Multiplicity dependence of the average transverse momentum in pp, p-Pb, and Pb-Pb collisions at the LHC arXiv:1307.1094.
- [100] J. Adams, et al., Incident energy dependence of pt correlations at RHIC, Phys.Rev. C72 (2005) 044902. arXiv:nucl-ex/0504031, doi:10.1103/PhysRevC.72.044902.
- [101] X.-N. Wang, M. Gyulassy, HIJING: A Monte Carlo model for multiple jet production in p p, p A and A A collisions, Phys.Rev. D44 (1991) 3501–3516. doi:10.1103/PhysRevD.44.3501.
- [102] W.-T. Deng, X.-N. Wang, R. Xu, Gluon shadowing and hadron production in heavy-ion collisions at LHC, Phys.Lett. B701 (2011) 133–136. arXiv:1011.5907, doi:10.1016/j.physletb.2011.05.040.
- [103] Z.-W. Lin, C. M. Ko, B.-A. Li, B. Zhang, S. Pal, A Multi-phase transport model for relativistic heavy ion collisions, Phys.Rev. C72 (2005) 064901. arXiv:nucl-th/0411110, doi:10.1103/PhysRevC.72.064901.
- [104] K. Aamodt, et al., Harmonic decomposition of two-particle angular correlations in Pb-Pb collisions at $\sqrt{s_{NN}} = 2.76$ TeV, Phys.Lett. B708 (2012) 249–264. arXiv:1109.2501, doi:10.1016/j.physletb.2012.01.060.
- [105] K. Aamodt, et al., Particle-yield modification in jet-like azimuthal di-hadron correlations in Pb-Pb collisions at $\sqrt{s_{NN}} = 2.76$ TeV, Phys.Rev.Lett. 108 (2012) 092301. arXiv:1110.0121, doi:10.1103/PhysRevLett.108.092301.
- [106] B. Abelev, et al., Measurement of Event Background Fluctuations for Charged Particle Jet Reconstruction in Pb-Pb collisions at $\sqrt{s_{NN}} = 2.76$ TeV, JHEP 1203 (2012) 053. arXiv:1201.2423, doi:10.1007/JHEP03(2012)053.
- [107] T. Renk, K. J. Eskola, Hard dihadron correlations in heavy-ion collisions at RHIC and LHC, Phys.Rev. C84 (2011) 054913. arXiv:1106.1740, doi:10.1103/PhysRevC.84.054913.
- [108] B. Abelev, et al., Charge correlations using the balance function in Pb-Pb collisions at $\sqrt{s_{NN}} = 2.76$ TeV, Phys.Lett. B723 (2013) 267–279. arXiv:1301.3756, doi:10.1016/j.physletb.2013.05.039.
- [109] M. Aggarwal, et al., Balance Functions from Au+Au, d+Au, and p+p Collisions at $\sqrt{s_{NN}} = 200$ GeV, Phys.Rev. C82 (2010) 024905. arXiv:1005.2307, doi:10.1103/PhysRevC.82.024905.
- [110] D. Kharzeev, Parity violation in hot QCD: Why it can happen, and how to look for it, Phys.Lett. B633 (2006) 260–264. arXiv:hep-ph/0406125, doi:10.1016/j.physletb.2005.11.075.
- [111] K. Fukushima, D. E. Kharzeev, H. J. Warringa, The Chiral Magnetic Effect, Phys.Rev. D78 (2008) 074033. arXiv:0808.3382, doi:10.1103/PhysRevD.78.074033.
- [112] D. E. Kharzeev, L. D. McLerran, H. J. Warringa, The Effects of topological charge change in heavy ion collisions: 'Event by event P and CP violation', Nucl.Phys. A803 (2008) 227–253. arXiv:0711.0950, doi:10.1016/j.nuclphysa.2008.02.298.
- [113] B. Abelev, et al., Charge separation relative to the reaction plane in Pb-Pb collisions at $\sqrt{s_{NN}} = 2.76$ TeV, Phys.Rev.Lett. 110 (2013) 012301. arXiv:1207.0900, doi:10.1103/PhysRevLett.110.012301.

- [114] S. A. Voloshin, Parity violation in hot QCD: How to detect it, Phys.Rev. C70 (2004) 057901. arXiv:hep-ph/0406311, doi:10.1103/PhysRevC.70.057901.
- [115] V. Toneev, V. Voronyuk, The Chiral Magnetic Effect: Beam-energy and system-size dependence, Phys.Atom.Nucl. 75 (2012) 607–612. arXiv:1012.1508, doi:10.1134/S1063778812050274.
- [116] B. Abelev, et al., Azimuthal Charged-Particle Correlations and Possible Local Strong Parity Violation, Phys.Rev.Lett. 103 (2009) 251601. arXiv:0909.1739, doi:10.1103/PhysRevLett.103.251601.
- [117] K. Ackermann, et al., Elliptic flow in Au + Au collisions at $(S(NN))^{**}(1/2) = 130$ GeV, Phys.Rev.Lett. 86 (2001) 402–407. arXiv:nucl-ex/0009011, doi:10.1103/PhysRevLett.86.402.
- [118] B. Back, M. Baker, M. Ballintijn, D. Barton, B. Becker, et al., The PHOBOS perspective on discoveries at RHIC, Nucl.Phys. A757 (2005) 28–101. arXiv:nucl-ex/0410022, doi:10.1016/j.nuclphysa.2005.03.084.
- [119] K. Adcox, et al., Formation of dense partonic matter in relativistic nucleus-nucleus collisions at RHIC: Experimental evaluation by the PHENIX collaboration, Nucl.Phys. A757 (2005) 184–283. arXiv:nucl-ex/0410003, doi:10.1016/j.nuclphysa.2005.03.086.
- [120] J. Adams, et al., Experimental and theoretical challenges in the search for the quark gluon plasma: The STAR Collaboration’s critical assessment of the evidence from RHIC collisions, Nucl.Phys. A757 (2005) 102–183. arXiv:nucl-ex/0501009, doi:10.1016/j.nuclphysa.2005.03.085.
- [121] I. Arsene, et al., Quark gluon plasma and color glass condensate at RHIC? The Perspective from the BRAHMS experiment, Nucl.Phys. A757 (2005) 1–27. arXiv:nucl-ex/0410020, doi:10.1016/j.nuclphysa.2005.02.130.
- [122] A. Adare, et al., Scaling properties of azimuthal anisotropy in Au+Au and Cu+Cu collisions at $s(NN) = 200$ -GeV, Phys.Rev.Lett. 98 (2007) 162301. arXiv:nucl-ex/0608033, doi:10.1103/PhysRevLett.98.162301.
- [123] R. Fries, B. Muller, C. Nonaka, S. Bass, Hadronization in heavy ion collisions: Recombination and fragmentation of partons, Phys.Rev.Lett. 90 (2003) 202303. arXiv:nucl-th/0301087, doi:10.1103/PhysRevLett.90.202303.
- [124] M. Luzum, P. Romatschke, Conformal Relativistic Viscous Hydrodynamics: Applications to RHIC results at $s(NN)^{**}(1/2) = 200$ -GeV, Phys.Rev. C78 (2008) 034915. arXiv:0804.4015, doi:10.1103/PhysRevC.78.034915, 10.1103/PhysRevC.79.039903.
- [125] P. Kovtun, D. Son, A. Starinets, Viscosity in strongly interacting quantum field theories from black hole physics, Phys.Rev.Lett. 94 (2005) 111601. arXiv:hep-th/0405231, doi:10.1103/PhysRevLett.94.111601.
- [126] B. Alver, B. Back, M. Baker, M. Ballintijn, D. Barton, et al., Importance of correlations and fluctuations on the initial source eccentricity in high-energy nucleus-nucleus collisions, Phys.Rev. C77 (2008) 014906. arXiv:0711.3724, doi:10.1103/PhysRevC.77.014906.
- [127] A. M. Poskanzer, S. Voloshin, Methods for analyzing anisotropic flow in relativistic nuclear collisions, Phys.Rev. C58 (1998) 1671–1678. arXiv:nucl-ex/9805001, doi:10.1103/PhysRevC.58.1671.
- [128] N. Borghini, P. M. Dinh, J.-Y. Ollitrault, A New method for measuring azimuthal distributions in nucleus-nucleus collisions, Phys.Rev. C63 (2001) 054906. arXiv:nucl-th/0007063, doi:10.1103/PhysRevC.63.054906.

- 2180 [129] N. Borghini, P. M. Dinh, J.-Y. Ollitrault, Flow analysis from multiparticle azimuthal correlations,
 2181 Phys.Rev. C64 (2001) 054901. arXiv:nucl-th/0105040, doi:10.1103/PhysRevC.64.054901.
- 2182 [130] N. Borghini, P. M. Dinh, J.-Y. Ollitrault, Flow analysis from cumulants: A Practical
 2183 guidearXiv:nucl-ex/0110016.
- 2184 [131] A. Bilandzic, R. Snellings, S. Voloshin, Flow analysis with cumulants: Direct calculations,
 2185 Phys.Rev. C83 (2011) 044913. arXiv:1010.0233, doi:10.1103/PhysRevC.83.044913.
- 2186 [132] R. Bhalerao, N. Borghini, J. Ollitrault, Genuine collective flow from Lee-Yang zeroes, Phys.Lett.
 2187 B580 (2004) 157–162. arXiv:nucl-th/0307018, doi:10.1016/j.physletb.2003.11.056.
- 2188 [133] N. Borghini, R. Bhalerao, J. Ollitrault, Anisotropic flow from Lee-Yang zeroes: A Practical guide,
 2189 J.Phys. G30 (2004) S1213–S1216. arXiv:nucl-th/0402053, doi:10.1088/0954-3899/30/8/092.
- 2190 [134] G. Aad, et al., Measurement of the azimuthal anisotropy for charged particle production in
 2191 $\sqrt{s_{NN}} = 2.76$ TeV lead-lead collisions with the ATLAS detector, Phys.Rev. C86 (2012) 014907.
 2192 arXiv:1203.3087, doi:10.1103/PhysRevC.86.014907.
- 2193 [135] K. Aamodt, et al., Higher harmonic anisotropic flow measurements of charged particles in
 2194 Pb-Pb collisions at $\sqrt{s_{NN}} = 2.76$ TeV, Phys.Rev.Lett. 107 (2011) 032301. arXiv:1105.3865,
 2195 doi:10.1103/PhysRevLett.107.032301.
- 2196 [136] G. Aad, et al., Measurement of the pseudorapidity and transverse momentum dependence of the
 2197 elliptic flow of charged particles in lead-lead collisions at $\sqrt{s_{NN}} = 2.76$ TeV with the ATLAS
 2198 detector, Phys.Lett. B707 (2012) 330–348. arXiv:1108.6018, doi:10.1016/j.physletb.2011.12.056.
- 2199 [137] K. Aamodt, et al., Elliptic flow of charged particles in Pb-Pb collisions at 2.76 TeV, Phys.Rev.Lett.
 2200 105 (2010) 252302. arXiv:1011.3914, doi:10.1103/PhysRevLett.105.252302.
- 2201 [138] M. Luzum, Elliptic flow at energies available at the CERN Large Hadron Collider: Comparing
 2202 heavy-ion data to viscous hydrodynamic predictions, Phys.Rev. C83 (2011) 044911.
 2203 arXiv:1011.5173, doi:10.1103/PhysRevC.83.044911.
- 2204 [139] S. Chatrchyan, et al., Measurement of the elliptic anisotropy of charged particles produced in
 2205 PbPb collisions at nucleon-nucleon center-of-mass energy of 2.76 TeV, Phys.Rev. C87 (2013)
 2206 014902. arXiv:1204.1409, doi:10.1103/PhysRevC.87.014902.
- 2207 [140] B. Abelev, et al., Anisotropic flow of charged hadrons, pions and (anti-)protons measured at high
 2208 transverse momentum in Pb-Pb collisions at $\sqrt{s_{NN}}=2.76$ TeV, Phys.Lett. B719 (2013) 18–28.
 2209 arXiv:1205.5761, doi:10.1016/j.physletb.2012.12.066.
- 2210 [141] S. Chatrchyan, et al., Azimuthal anisotropy of charged particles at high transverse momenta
 2211 in PbPb collisions at $\sqrt{s_{NN}} = 2.76$ TeV, Phys.Rev.Lett. 109 (2012) 022301. arXiv:1204.1850,
 2212 doi:10.1103/PhysRevLett.109.022301.
- 2213 [142] B. Alver, G. Roland, Collision geometry fluctuations and triangular flow in heavy-ion collisions,
 2214 Phys.Rev. C81 (2010) 054905. arXiv:1003.0194, doi:10.1103/PhysRevC.82.039903, 10.1103/Phys-
 2215 RevC.81.054905.
- 2216 [143] Z. Qiu, U. W. Heinz, Event-by-event shape and flow fluctuations of relativistic heavy-ion collision
 2217 fireballs, Phys.Rev. C84 (2011) 024911. arXiv:1104.0650, doi:10.1103/PhysRevC.84.024911.

- 2218 [144] B. Abelev, et al., Directed flow of charged particles at mid-rapidity relative to the spectator plane
 2219 in Pb-Pb collisions at $\sqrt{s_{NN}} = 2.76$ TeV, Phys.Rev.Lett. 111 (2013) 232302. arXiv:1306.4145,
 2220 doi:10.1103/PhysRevLett.111.232302.
- 2221 [145] G. Aad, et al., Measurement of the distributions of event-by-event flow harmonics in lead-lead
 2222 collisions at $\sqrt{s_{NN}} = 2.76$ TeV with the ATLAS detector at the LHC arXiv:1305.2942.
- 2223 [146] S. Chatrchyan, et al., Measurement of higher-order harmonic azimuthal anisotropy in PbPb col-
 2224 lisions at a nucleon-nucleon center-of-mass energy of 2.76 TeV arXiv:1310.8651.
- 2225 [147] C. Salgado, J. Alvarez-Muniz, F. Arleo, N. Armesto, M. Botje, et al., Proton-Nucleus Collisions at
 2226 the LHC: Scientific Opportunities and Requirements, J.Phys. G39 (2012) 015010. arXiv:1105.3919,
 2227 doi:10.1088/0954-3899/39/1/015010.
- 2228 [148] S. Chatrchyan, et al., Study of W boson production in PbPb and pp collisions at $\sqrt{s_{NN}} = 2.76$
 2229 TeV, Phys.Lett. B715 (2012) 66–87. arXiv:1205.6334, doi:10.1016/j.physletb.2012.07.025.
- 2230 [149] G. Aad, et al., Measurement of Z boson Production in Pb+Pb Collisions at $\sqrt{s_{NN}} =$
 2231 2.76 TeV with the ATLAS Detector, Phys.Rev.Lett. 110 (2013) 022301. arXiv:1210.6486,
 2232 doi:10.1103/PhysRevLett.110.022301.
- 2233 [150] H. Paukkunen, C. A. Salgado, Constraints for the nuclear parton distributions from Z and W
 2234 production at the LHC, JHEP 1103 (2011) 071. arXiv:1010.5392, doi:10.1007/JHEP03(2011)071.
- 2235 [151] S. Chatrchyan, et al., Measurement of isolated photon production in pp and PbPb
 2236 collisions at $\sqrt{s_{NN}} = 2.76$ TeV, Phys.Lett. B710 (2012) 256–277. arXiv:1201.3093,
 2237 doi:10.1016/j.physletb.2012.02.077.
- 2238 [152] Measurement of high-pT isolated prompt photons in lead-lead collisions at $\sqrt{s_{NN}} = 2.76$ TeV with
 2239 the ATLAS detector at the LHC.
- 2240 [153] M. Wilde, Measurement of Direct Photons in pp and Pb-Pb Collisions with ALICE, Nucl.Phys.
 2241 A904-905 (2013) 573c–576c. arXiv:1210.5958, doi:10.1016/j.nuclphysa.2013.02.079.
- 2242 [154] A. Adare, et al., Enhanced production of direct photons in Au+Au collisions at $\sqrt{s_{NN}} = 200$ GeV
 2243 and implications for the initial temperature, Phys.Rev.Lett. 104 (2010) 132301. arXiv:0804.4168,
 2244 doi:10.1103/PhysRevLett.104.132301.
- 2245 [155] M. Cacciari, G. P. Salam, G. Soyez, The Anti-k(t) jet clustering algorithm, JHEP 0804 (2008)
 2246 063. arXiv:0802.1189, doi:10.1088/1126-6708/2008/04/063.
- 2247 [156] K. Adcox, et al., Suppression of hadrons with large transverse momentum in central Au+Au
 2248 collisions at $\sqrt{s_{NN}} = 130$ -GeV, Phys.Rev.Lett. 88 (2002) 022301. arXiv:nucl-ex/0109003,
 2249 doi:10.1103/PhysRevLett.88.022301.
- 2250 [157] C. Adler, et al., Centrality dependence of high p_T hadron suppression in Au+Au col-
 2251 lisions at $\sqrt{s_{NN}} = 130$ -GeV, Phys.Rev.Lett. 89 (2002) 202301. arXiv:nucl-ex/0206011,
 2252 doi:10.1103/PhysRevLett.89.202301.
- 2253 [158] U. A. Wiedemann, Jet Quenching in Heavy Ion Collisions (2010) 521–562 arXiv:0908.2306.
- 2254 [159] G. Aad, et al., Observation of a Centrality-Dependent Dijet Asymmetry in Lead-Lead Collisions
 2255 at $\sqrt{s_{NN}} = 2.77$ TeV with the ATLAS Detector at the LHC, Phys.Rev.Lett. 105 (2010) 252303.
 2256 arXiv:1011.6182, doi:10.1103/PhysRevLett.105.252303.

- 2257 [160] S. Chatrchyan, et al., Observation and studies of jet quenching in PbPb collisions at nucleon-
 2258 nucleon center-of-mass energy = 2.76 TeV, Phys. Rev. C 84 (2011) 024906. arXiv:1102.1957,
 2259 doi:10.1103/PhysRevC.84.024906.
- 2260 [161] S. Chatrchyan, et al., Jet momentum dependence of jet quenching in PbPb colli-
 2261 sions at $\sqrt{s_{NN}} = 2.76$ TeV, Phys. Lett. B 712 (2012) 176. arXiv:1202.5022,
 2262 doi:10.1016/j.physletb.2012.04.058.
- 2263 [162] CMS Collaboration, Commissioning of the particle-flow reconstruction in minimum-bias and jet
 2264 events from p+pp+p collisions at 7 TeV, CMS Physics Analysis Summary CMS-PAS-PFT-10-002.
 2265 URL <http://cdsweb.cern.ch/record/1279341>
- 2266 [163] M. Nguyen, et al., Jet reconstruction with particle flow in heavy-ion collisions with CMS, J. Phys.
 2267 G 38 (2011) 124151. arXiv:1107.0179, doi:10.1088/0954-3899/38/12/124151.
- 2268 [164] G. Aad, et al., Measurement of the jet radius and transverse momentum dependence of inclusive
 2269 jet suppression in lead-lead collisions at $\sqrt{s_{NN}} = 2.76$ TeV with the ATLAS detector, Phys. Lett.
 2270 B 719 (2013) 220. arXiv:1208.1967, doi:10.1016/j.physletb.2013.01.024.
- 2271 [165] J. Adams, et al., Azimuthal anisotropy and correlations at large transverse momenta in p+p and
 2272 Au+Au collisions at $s(\text{NN})^{**}(1/2) = 200\text{-GeV}$, Phys.Rev.Lett. 93 (2004) 252301. arXiv:nucl-
 2273 ex/0407007, doi:10.1103/PhysRevLett.93.252301.
- 2274 [166] S. Adler, et al., A Detailed Study of High-p(T) Neutral Pion Suppression and Azimuthal
 2275 Anisotropy in Au+Au Collisions at $s(\text{NN})^{**}(1/2) = 200\text{-GeV}$, Phys.Rev. C76 (2007) 034904.
 2276 arXiv:nucl-ex/0611007, doi:10.1103/PhysRevC.76.034904.
- 2277 [167] A. Adare, et al., Azimuthal anisotropy of neutral pion production in Au+Au collisions at
 2278 $\sqrt{(s_N N)} = 200$ GeV: Path-length dependence of jet quenching and the role of initial geometry,
 2279 Phys.Rev.Lett. 105 (2010) 142301. arXiv:1006.3740, doi:10.1103/PhysRevLett.105.142301.
- 2280 [168] G. Aad, et al., Measurement of the Azimuthal Angle Dependence of Inclusive Jet Yields in
 2281 Pb+Pb Collisions at $\sqrt{s_{NN}} = 2.76$ TeV with the ATLAS detector, Phys.Rev.Lett. 111 (2013)
 2282 152301. arXiv:1306.6469, doi:10.1103/PhysRevLett.111.152301.
- 2283 [169] I. Vitev, S. Wicks, B.-W. Zhang, A Theory of jet shapes and cross sections: From hadrons to
 2284 nuclei, JHEP 0811 (2008) 093. arXiv:0810.2807, doi:10.1088/1126-6708/2008/11/093.
- 2285 [170] I. Vitev, B.-W. Zhang, Jet tomography of high-energy nucleus-nucleus collisions at next-to-leading
 2286 order, Phys.Rev.Lett. 104 (2010) 132001. arXiv:0910.1090, doi:10.1103/PhysRevLett.104.132001.
- 2287 [171] Y. He, I. Vitev, B.-W. Zhang, $\mathcal{O}(\alpha_s^3)$ Analysis of Inclusive Jet and di-Jet Production in Heavy
 2288 Ion Reactions at the Large Hadron Collider, Phys.Lett. B713 (2012) 224–232. arXiv:1105.2566,
 2289 doi:10.1016/j.physletb.2012.05.054.
- 2290 [172] Y. L. Dokshitzer, V. A. Khoze, Basics of perturbative QCD, Editions Frontières, 1991.
- 2291 [173] S. Chatrchyan, et al., Measurement of jet fragmentation into charged particles in pp
 2292 and PbPb collisions at $\sqrt{s_{NN}} = 2.76$ TeV, JHEP 1210 (2012) 087. arXiv:1205.5872,
 2293 doi:10.1007/JHEP10(2012)087.
- 2294 [174] Y. Mehtar-Tani, C. A. Salgado, K. Tywoniuk, Anti-angular ordering of gluon ra-
 2295 diation in QCD media, Phys. Rev. Lett. 106 (2011) 122002. arXiv:1009.2965,
 2296 doi:10.1103/PhysRevLett.106.122002.

- [175] A. Idilbi, A. Majumder, Extending soft-collinear-effective-theory to describe hard jets in dense QCD media, Phys. Rev. D 80 (2009) 054022. arXiv:0808.1087, doi:10.1103/PhysRevD.80.054022.
- [176] J. Casalderrey-Solana, E. Iancu, Interference effects in medium-induced gluon radiation, JHEP 08 (2011) 015. arXiv:1105.1760, doi:10.1007/JHEP08(2011)015.
- [177] J. Casalderrey-Solana, J. G. Milhano, U. Wiedemann, Jet quenching via jet collimation, J. Phys. G 38 (2011) 124086. arXiv:1107.1964, doi:10.1088/0954-3899/38/12/124086.
- [178] R. B. Neufeld, I. Vitev, Parton showers as sources of energy-momentum deposition in the QGP and their implication for shockwave formation at RHIC and at the LHC, Phys. Rev. C 86 (2012) 024905. arXiv:1105.2067, doi:10.1103/PhysRevC.86.024905.
- [179] J.-P. Blaizot, F. Dominguez, E. Iancu, Y. Mehtar-Tani, Medium-induced gluon branching, JHEP 01 (2013) 143. arXiv:1209.4585, doi:10.1007/JHEP01(2013)143.
- [180] M. Fickinger, G. Ovanesyan, I. Vitev, Angular distributions of higher order splitting functions in the vacuum and in dense QCD matter, JHEP 07 (2013) 059. arXiv:1304.3497, doi:10.1007/JHEP07(2013)059.
- [181] S. Chatrchyan, et al., Modification of jet shapes in PbPb collisions at $\sqrt{s_{NN}} = 2.76$ TeV arXiv:1310.0878.
- [182] T. Renk, Medium-modified jet shapes and other jet observables from in-medium parton shower evolution, Phys. Rev. C 80 (2009) 044904. arXiv:0906.3397, doi:10.1103/PhysRevC.80.044904.
- [183] S. Chatrchyan, et al., Studies of jet quenching using isolated-photon+jet correlations in PbPb and pp collisions at $\sqrt{s_{NN}} = 2.76$ TeV, Phys. Lett. B 18 (2013) 773. arXiv:1205.0206, doi:10.1016/j.physletb.2012.11.003.
- [184] S. Chatrchyan, et al., Measurement of isolated photon production in pp and PbPb collisions at $\sqrt{s_{NN}} = 2.76$ TeV, Phys. Lett. B 710 (2012) 256. doi:10.1016/j.physletb.2012.02.077.
- [185] R. Sharma, I. Vitev, B.-W. Zhang, Light-cone wave function approach to open heavy flavor dynamics in QCD matter, Phys. Rev. C 80 (2009) 054902. arXiv:0904.0032, doi:10.1103/PhysRevC.80.054902.
- [186] W. Horowitz, M. Gyulassy, Quenching and Tomography from RHIC to LHC, J. Phys. G 38 (2011) 124114. arXiv:1107.2136, doi:10.1088/0954-3899/38/12/124114.
- [187] W. Horowitz, Testing pQCD and AdS/CFT Energy Loss at RHIC and LHC, AIP Conf. Proc. 1441 (2012) 889–891. arXiv:1108.5876, doi:10.1063/1.3700710.
- [188] W. Alberico, A. Beraudo, A. De Pace, A. Molinari, M. Monteno, et al., Heavy-flavour spectra in high energy nucleus-nucleus collisions, Eur. Phys. J. C 71 (2011) 1666. arXiv:1101.6008, doi:10.1140/epjc/s10052-011-1666-6.
- [189] M. Monteno, W. Alberico, A. Beraudo, A. De Pace, A. Molinari, et al., Heavy-flavor dynamics in nucleus-nucleus collisions: from RHIC to LHC, J. Phys. G 38 (2011) 124144. arXiv:1107.0256, doi:10.1088/0954-3899/38/12/124144.
- [190] P. Gossiaux, R. Bierkandt, J. Aichelin, Tomography of a quark gluon plasma at RHIC and LHC energies, Phys. Rev. C 79 (2009) 044906. arXiv:0901.0946, doi:10.1103/PhysRevC.79.044906.

- 2335 [191] P. Gossiaux, J. Aichelin, T. Gousset, V. Guiho, Competition of Heavy Quark Radiative and
 2336 Collisional Energy Loss in Deconfined Matter, *J.Phys. G*37 (2010) 094019. arXiv:1001.4166,
 2337 doi:10.1088/0954-3899/37/9/094019.
- 2338 [192] O. Fochler, J. Uphoff, Z. Xu, C. Greiner, Jet quenching and elliptic flow at RHIC and LHC
 2339 within a pQCD-based partonic transport model, *J.Phys. G*38 (2011) 124152. arXiv:1107.0130,
 2340 doi:10.1088/0954-3899/38/12/124152.
- 2341 [193] A. Buzzatti, M. Gyulassy, Jet Flavor Tomography of Quark Gluon Plasmas at RHIC and LHC,
 2342 *Phys.Rev.Lett.* 108 (2012) 022301. arXiv:1106.3061, doi:10.1103/PhysRevLett.108.022301.
- 2343 [194] B. Abelev, et al., Measurement of electrons from semileptonic heavy-flavour hadron de-
 2344 cays in pp collisions at $\sqrt{s} = 7\text{TeV}$, *Phys.Rev. D*86 (2012) 112007. arXiv:1205.5423,
 2345 doi:10.1103/PhysRevD.86.112007.
- 2346 [195] S. Chatrchyan, et al., Suppression of non-prompt J/ψ , prompt J/ψ , and Y(1S) in PbPb collisions
 2347 at $\sqrt{s_{NN}} = 2.76$ TeV, *JHEP* 1205 (2012) 063. arXiv:1201.5069, doi:10.1007/JHEP05(2012)063.
- 2348 [196] C. Collaboration, J/ψ results from CMS in PbPb collisions, with 150mub-1 data.
- 2349 [197] T. Matsui, H. Satz, J/ψ Suppression by Quark-Gluon Plasma Formation, *Phys. Lett. B*178 (1986)
 2350 416. doi:10.1016/0370-2693(86)91404-8.
- 2351 [198] S. Digal, P. Petreczky, H. Satz, Quarkonium feed-down and sequential suppression, *Phys. Rev. D*
 2352 64 (2001) 094015. arXiv:hep-ph/0106017, doi:10.1103/PhysRevD.64.094015.
- 2353 [199] B. Alessandro, et al., A New measurement of J/ψ suppression in Pb-Pb collisions at 158-GeV per
 2354 nucleon, *Eur.Phys.J. C*39 (2005) 335–345. arXiv:hep-ex/0412036, doi:10.1140/epjc/s2004-02107-
 2355 9.
- 2356 [200] A. Adare, et al., j/ψ production vs centrality, transverse momentum, and rapidity in au +
 2357 au collisions at $\sqrt{s_{NN}} = 200$ gev, *Phys. Rev. Lett.* 98 (2007) 232201. arXiv:nucl-ex/0611020,
 2358 doi:10.1103/PhysRevLett.98.232201.
- 2359 [201] A. Adare, et al., J/ψ suppression at forward rapidity in Au+Au collisions at $\sqrt{s_{NN}} = 200$ GeV,
 2360 *Phys.Rev. C*84 (2011) 054912. arXiv:1103.6269, doi:10.1103/PhysRevC.84.054912.
- 2361 [202] P. Braun-Munzinger, J. Stachel, (Non)thermal aspects of charmonium production and a
 2362 new look at J/ψ suppression, *Phys.Lett. B*490 (2000) 196–202. arXiv:nucl-th/0007059,
 2363 doi:10.1016/S0370-2693(00)00991-6.
- 2364 [203] R. L. Thews, M. Schroedter, J. Rafelski, Enhanced J/ψ production in deconfined quark matter,
 2365 *Phys.Rev. C*63 (2001) 054905. arXiv:hep-ph/0007323, doi:10.1103/PhysRevC.63.054905.
- 2366 [204] A. Andronic, P. Braun-Munzinger, K. Redlich, J. Stachel, Evidence for charmonium generation
 2367 at the phase boundary in ultra-relativistic nuclear collisions, *Phys.Lett. B*652 (2007) 259–261.
 2368 arXiv:nucl-th/0701079, doi:10.1016/j.physletb.2007.07.036.
- 2369 [205] X. Zhao, R. Rapp, Transverse Momentum Spectra of J/ψ in Heavy-Ion Collisions, *Phys.Lett.*
 2370 *B*664 (2008) 253–257. arXiv:0712.2407, doi:10.1016/j.physletb.2008.03.068.
- 2371 [206] G. Aad, et al., Measurement of the centrality dependence of J/ψ yields and observation of Z
 2372 production in lead-lead collisions with the ATLAS detector at the LHC, *Phys.Lett. B*697 (2011)
 2373 294–312. arXiv:1012.5419, doi:10.1016/j.physletb.2011.02.006.

- 2374 [207] A. Rakotozafindrabe, E. Ferreiro, F. Fleuret, J. Lansberg, N. Matagne, Cold Nuclear Matter
 2375 Effects on extrinsic J/ψ production at $\sqrt{s_{NN}} = 2.76$ TeV at the LHC, Nucl.Phys. A855 (2011)
 2376 327–330. arXiv:1101.0488, doi:10.1016/j.nuclphysa.2011.02.071.
- 2377 [208] R. Vogt, Cold nuclear matter effects on J/ψ and Υ production at energies available at the
 2378 CERN Large Hadron Collider (LHC), Phys. Rev. C 81 (2010) 044903. arXiv:1003.3497,
 2379 doi:10.1103/PhysRevC.81.044903.
- 2380 [209] F. Dominguez, D. Kharzeev, E. Levin, A. Mueller, K. Tuchin, Gluon saturation effects on the color
 2381 singlet J/Ψ production in high energy dA and AA collisions, Phys.Lett. B710 (2012) 182–187.
 2382 arXiv:1109.1250, doi:10.1016/j.physletb.2012.02.068.
- 2383 [210] Y.-p. Liu, Z. Qu, N. Xu, P.-f. Zhuang, J/ψ Transverse Momentum Distribution in
 2384 High Energy Nuclear Collisions at RHIC, Phys.Lett. B678 (2009) 72–76. arXiv:0901.2757,
 2385 doi:10.1016/j.physletb.2009.06.006.
- 2386 [211] K. Zhou, N. Xu, P. Zhuang, Quarkonium Production and Medium Effects in High Energy Nuclear
 2387 Collisions arXiv:1309.7520.
- 2388 [212] B. B. Abelev, et al., J/ψ production and nuclear effects in p-Pb collisions at $\sqrt{s_{NN}}=5.02$
 2389 TeV arXiv:1308.6726.
- 2390 [213] R. Aaij, et al., Study of J/ψ production and cold nuclear matter effects in $p\text{Pb}$ collision-
 2391 sarXiv:1308.6729.
- 2392 [214] L. Adamczyk, et al., Measurement of J/ψ Azimuthal Anisotropy in Au+Au Collisions at $\sqrt{s_{NN}}$
 2393 = 200 GeV arXiv:1212.3304.
- 2394 [215] Y. Liu, N. Xu, P. Zhuang, J/ψ elliptic flow in relativistic heavy ion collisions, Nucl.Phys. A834
 2395 (2010) 317C–319C. arXiv:0910.0959, doi:10.1016/j.nuclphysa.2010.01.008.
- 2396 [216] X. Zhao, A. Emerick, R. Rapp, In-Medium Quarkonia at SPS, RHIC and LHC, Nucl.Phys.A904-
 2397 905 2013 (2013) 611c–614c. arXiv:1210.6583, doi:10.1016/j.nuclphysa.2013.02.088.
- 2398 [217] S. Chatrchyan, et al., Indications of suppression of excited upsilon states in pbpb col-
 2399 lisions at $\sqrt{s_{NN}}= 2.76$ TeV, Phys. Rev. Lett. 107 (2011) 052302. arXiv:1105.4894,
 2400 doi:10.1103/PhysRevLett.107.052302.
- 2401 [218] A. Affolder, et al., Production of $\Upsilon(1S)$ mesons from χ_b decays in $p\bar{p}$ collisions at $\sqrt{s} = 1.8$ TeV,
 2402 Phys. Rev. Lett. 84 (2000) 2094. arXiv:hep-ex/9910025, doi:10.1103/PhysRevLett.84.2094.
- 2403 [219] R. Aaij, et al., Measurement of the fraction of $\Upsilon(1S)$ originating from $\chi_b(1P)$ decays in pp collisions
 2404 at $\sqrt{s} = 7$ TeV, JHEP 1211 (2012) 031. arXiv:1209.0282, doi:10.1007/JHEP11(2012)031.
- 2405 [220] B. Abelev, et al., Letter of Intent for the Upgrade of the ALICE Experiment arXiv:CERN-LHCC-
 2406 2012-012 ; LHCC-I-022.